Meron Yemane

Modelling and Control of Wave-to-Wire Model of Point Absorber Wave Energy Converters (WECs)

Master's thesis in Electric Power Engineering
Supervisor: Elisabetta Tedeschi
June 2019

NTNU

Norwegian University of
Science and Technology

NTNU
Norwegian University of
Science and Technology

Modelling and Control of Wave-to-Wire Model of Point Absorber Wave Energy Converters (WECs)

Meron Yemane

Master of Science in Electric Power Engineering
Supervisor: Elisabetta Tedeschi
Co-Supervisor: Dan El Andres Montoya Andrade
June 2019

Norwegian University of Science and Technology
Faculty of Engineering
Department of Electric Power Engineering

This page intentionally left blank

Abstract

Waves have a huge potential where around 10% of the world's electricity demand can be supplied from wave energy. This provides a unique opportunity to bring more renewable energy into the world by deploying wave energy converters (WECs). The ability of WECs to stand alone in places where there is no grid also offers WECs special importance.

This master thesis presents the modelling and control of wave-to-wire model of point absorber wave energy converters (WECs). The point absorber (PA3) used is adopted from the Cruz-Atcheson Consulting Engineers model developed within the EU project IMAGINE and inspired by the CETO3 WEC. The WEC is connected to a rotating permanent magnet synchronous generator (PMSG) directly through a recirculating ball screw. The PMSG is connected to a dc-link through a converter. Two types of control strategies are applied to maximize the power extracted from the incoming irregular wave. These are passive loading and optimum control. The study is limited to an incoming irregular wave of Bretschneider spectrum with a significant height of $3.25\,m$ and a peak period of 12 seconds. The constraints on power, end limits and the maximum power that the PMSG can generate, $296.20\,kW$, are taken into account.

Passive loading and optimum control are applied with and without of capping of mechanical input power to the PMSG at $250\,kW$. The highest maximum average power of $35.82\,kW$ is generated by uncapped optimum control with a ratio of peak to average electrical power, 8.64. The maximum average value is 3.5%, 4% and 1.5% higher than the maximum average power obtained in uncapped passive loading, capped passive loading and capped optimum control respectively. The difference is lowered due to the limit of maximum power generated by PMSG. The PA3 has two degrees of freedom and therefore a power higher than the capping value is generated. The delay of the actuator also influences the power generated by the WEC.

Keywords: wave energy, WEC, point absorber, control strategies, PMSG, passive loading, optimum control

Sammendrag

Bølger har et stort potensial, da rundt 10% av verdens strømforbruk kan leveres fra bølgeenergi. Dette gir en unik mulighet til å bringe mer fornybar energi inn i verden ved bruken av bølgeenergiomformere (WEC). WEC-er sin evne til å stå alene på steder der det ikke er noe nett, gir også WEC-er en spesiell betydning.

Denne masteroppgaven presenterer modellering og kontroll av en bølge-til-kabel (wave-to-wire-modell) av punktabsorbator WEC-er. Punktabsorbatoren (PA3) som brukes er fra Cruz-Atcheson Consulting Engineers-modell, utviklet i EU-prosjektet IMAGINE og inspirert av CETO3 WEC. WEC-en er koblet til en roterende permanentmagnet synkron-generator (PMSG) direkte gjennom en resirkulerende kuleskrue. PMSG-en er koblet til en DC-kobling gjennom en omformer. To typer kontrollstrategier, henholdsvis passiv lasting og optimal kontroll (passive loading og optimum control), blir brukt for å maksimere effekten utvunnet fra innkommende uregelmessig bølge. Masteroppgaven er begrenset til en innkommende uregelmessig bølge av Bretschneider-spektrum med en betydelig høyde på $3,25\,m$ og en topperiode på 12 sekunder. Begrensningene på effekt, sluttgrenser og maksimal effekt som PMSG-en kan generere, $296.20\,kW$, er tatt hensyn til.

Passive loading og optimum control påføres med og uten begrensning av mekanisk in-ngangseffekt til PMSG-en ved $250\,kW$. Den høyeste maksimale gjennomsnittlige effek-ten på $35,82\,kW$ genereres ved ubegrenset optimal kontroll med et forhold mellom topp og gjennomsnittlig på $8,64$. Den maksimale gjennomsnittsverdien er $3,5\%$, 4% og $1,5\%$ høyere enn den maksimale gjennomsnittlige effekten som er oppnådd ved henholdsvis ubegrenset passive loading, begrenset passive loading og begrenset optimum control. Forskjellen er senket på grunn av grensen for maksimal effekt generert av PMSG-en. Da PA3 har to frihetsgrader, er den maksimale genererte kraften høyere enn PMSG-en sin begrensende effektverdi.

Preface

This thesis is a completion of the master of science in Electric Power Engineering at Norwegian University of Science and Technology (NTNU). It presents the modelling and control of wave-to-wire model of point absorber wave energy converters (WECs).

Wave energy is renewable energy and it has a huge potential which is starting to be utilized. It has been a very interesting experience to work in this nascent technology and follow the current researches and developments in point absorber wave energy converters.

I would like to thank my supervisor professor Elisabetta Tedeschi and co-supervisor Dr Dan El Andres Montoya Andrade for the guidance, assistance and for being easily accessible whenever I needed help. I would also like to thank Mr Erick Fernando Alves for his valuable input and support to my master thesis.

Trondheim, 17th Juni 2019

Table of Contents

List of Figures

Abbreviations

1DoF	One degree of Freedom
AVT	Approximate optimal velocity tracking
AWS	Archimedes Wave Swing
c	Causal
d-axis	Direct Axis
EMF	Electromotive Force
EMG	Electro-Mechanical Generator
FOC	Field-Oriented Control
JONSWAP	Joint North Sea Water Project
OPEC	Organization of Petroleum Exporting Countries
LPMG	Linear Permanent Magnet Generator
LTI	Linear Time Invariant
MIMO	Multiple Input Multiple Output
OPT	Open Power Technologies
OTS	Overtopping System
OWC	Oscillating Water Column
PI	Proportional-Integral
PMSG	Permanent Magnet Synchronous Generator
PTO	Power Take Off
q-axis	Quadrature Axis
RIRF	Radiation Impulse Response Function
RPMG	Rotating Permanent Magnet Generator
PWM	Pulse Width Modulation
RMS	Root Mean Square
RPM	Revolutions Per Minute
SISO	Single Input Single Output
TWh	Tera Watt Hour
VdqFF	Feed Forward Voltages v_d and v_q
Vphmax	Maximum phase voltage input of current controller
WAB	Wave Activated Body
W2W	Wave-to-Wire
WEC	Wave Energy Converter
Wec-Sim	Wave Energy Converter Simulator

Nomenclature

Symbol	SI Unit	Description
A	$[kg]$	Frequency independent added water
m_r	$[kg]$	Frequency dependent added mass
$m_r(\infty)$	$[kg]$	Added mass when frequency approaches infinity
A_w	$[m^2]$	Water surface area of the point absorber
m	$[kg]$	Mass of the device including generator inertia
E		State-space system matrix
F		State-space system matrix
G		State-space system matrix
L		State-space system matrix
u		Input of state-space system matrix
B	$[N/(m/s)]$	Radiation damping
F_R	$[N]$	Wave Radiation Force
H_{rad}	$[N/m]$	Radiation Impulse Response Function (RIRF)
R_r	$[N/(m/s)]$	Radiation resistance
B_{PTO}	$[N/(m/s)]$	Damping coefficient of the PTO
$B(w)$	$[N/(m/s)]$	Frequency dependent mechanical damping
S	$[N/m]$	Spring in mass-spring-damper system or geometry of the float
R	$[N/(m/s)]$	Mechanical damping in mass-spring-damper system or Radiation coefficient matrix
K	$[N/m]$	Hydrodynamic stiffness
k	$[N/m]$	Hydrostatic stiffness
M_{PTO}	$[kg]$	Spring coefficient of the PTO
S_{PTO}	$[kg]$	Stiffness coefficient of the PTO
w	$[Hz]$	Frequency
T	$[s]$	Period
τ_c	$[s]$	Time shift
ρ	$[kg/m^3]$	Ocean water density
h	$[m]$	Vertical distance between the mean water level and the sea bed
H	$[m]$	Maximum water surface elevation of a wave from a trough to a crest
η	$[m]$	Amplitude of a wave with respect to mean water level
z	$[m]$	Float vertical (heave) position
v	$[m/s]$	Speed of the heave
v_a	$[V]$	Voltage of phase a across the stator windings
v_b	$[V]$	Voltage of phase b across the stator windings
v_c	$[V]$	Voltage of phase c across the stator windings
R_s	$[\Omega]$	Equivalent resistance of each stator windings
L_d	$[H]$	d axis inductance
L_q	$[H]$	q axis inductance
w_m	$[rad/s]$	Rotor mechanical rotational speed
i_a	$[A]$	Current of phase a flowing in the stator windings
i_b	$[A]$	Current of phase b flowing in the stator windings
i_c	$[A]$	Current of phase c flowing in the stator windings
I	$[A]$	Amplitude of current

v_d	$[V]$	d axis PMSG voltage
v_q	$[V]$	q axis PMSG voltage
v_d'	$[V]$	d axis PMSG voltage after feed forward
v_q'	$[V]$	q axis PMSG voltage after feed forward
$v_{dc-link}$	$[V]$	DC link voltage
i_d	$[A]$	d axis PMSG current
i_q	$[A]$	q axis PMSG current
i_{dref}	$[A]$	d axis reference current
i_{qref}	$[A]$	q axis reference current
V	$[V]$	Amplitude of voltage
Ψ_a	$[Wb]$	Rate of change of magnitude flux in phase a stator windings
Ψ_b	$[Wb]$	Rate of change of magnitude flux in phase b stator windings
Ψ_c	$[Wb]$	Rate of change of magnitude flux in phase c stator windings
Ψ_m	$[Wb]$	Rotor flux linkage
Ψ_d	$[Wb]$	Direct axis flux linkage
Ψ_q	$[Wb]$	Quadrature axis flux linkage
T_e	$[Nm/rad]$	Rotor torque
$T_{\alpha\beta\gamma}$		Clarke transformation matrix
T_{dq0}		Park transformation matrix
a	$[m/s^2]$	Acceleration of the heave
ϕ	$[deg]$	Initial angle of the current
t	$[s]$	Time
w	$[rad/s]$	Frequency for three-phase current
θ	$[deg]$	Angle of the signal
F_{pe}	$[N]$	Force caused by external pressure
F_{re}	$[N]$	Reaction forces
F_r	$[N]$	Convolution term
F_e	$[N]$	Wave Excitation Force
h_η	$[N/m]$	Excitation force coefficient
F_l	$[N]$	Mooring Force
F_o	$[N]$	Environmental Force
F_B	$[N]$	Float Buoyancy Force
F_{PTO}	$[N]$	Power Take Off
F_v	$[N]$	Viscous Force
F_D	$[N]$	Damper force in a mass-spring-damper system
F_S	$[N]$	Spring force in a mass-spring-damper system
F	$[N]$	External force in a mass-spring-damper system
g	$[m/s^2]$	Gravitation force of attraction
R_{wec}	$[\Omega]$	Resistance part of electrical equivalent of WEC
X_{wec}	$[\Omega]$	Reactance part of electrical equivalent of WEC
C_{wec}	$[F]$	Reactance part of electrical equivalent of WEC
L_{wec}	$[H]$	Reactance part of electrical equivalent of WEC
R_{PTO}	$[\Omega]$	Resistance part of the PTO
X_{PTO}	$[\Omega]$	Reactance part of the PTO
B_{opt}	$[N/(m/s)]$	Optimal value of damping coefficient
M_{opt}	$[N/(m/s^2)]$	Optimal value of spring coefficient
S_{opt}	$[N/m]$	Optimal value of stiffness coefficient
Z_{PTO}	$[\Omega]$	Impedance part of the PTO

H_s	$[m]$	Significant height
T_p	$[s]$	Peak period
P_{mean}	$[W]$	Mean output power
P_{peak}	$[W]$	Peak output power
F_{peak}	$[N]$	Peak force
v_{peak}	$[m/s]$	Peak velocity
z_{peak}	$[m]$	Peak position
W_p	$[J]$	Potential energy
W_k	$[J]$	Kinetic energy
sig		Signal
$S(w)$	$[m^2/(rad/sec)]$	Wave spectral density
p_{sc}	$[m]$	Screw pitch
v_{in}	$[m/s]$	Linear input speed of ball screw
η_{bs}		Ball screw efficiency
T_{ref}	$[Nm]$	Reference rotational torque
P_{cu}	$[W]$	The copper resistance stator winding power loss
e	$[A]$	Error signal of PI controller
du	$[V]$	Control signal saturation of the PI controller
$Reset$		Integrator gain reset

This page intentionally left blank

Chapter 1

Introduction

Chapter 1 introduces wave energy converters (WECs) in general and point absorbers in particular. It also provides a basic description of a corresponding modelling approach.

Wind blowing over a surface of sea or ocean creates wave energy. The heat energy from the sun affects the earth unequally due to the presence of cloud covers, valleys, mountains, vegetation, desert lands, seas, and other scenarios. Warm air expands and rises up creating a low pressure. The surrounding air with lower temperature has a higher pressure and this results in the flow of air from the higher pressure to the lower pressure area and forms wind as shown in Figure 1.1. The strong wind blowing over the surface of the sea or ocean creates waves. Different kinds of waves are created depending on what initiates the wave. Storms and extreme weather conditions far away can produce long and steady waves that flow endlessly. A nearby weather system that rise and fall quickly creates the often seen high and choppy waves [1]. They are normally newly formed occurrences. Though wind blowing over the surface of the sea or ocean produces the majority of ocean waves, there are other ways ocean waves could be generated [2]. These include earthquakes and planetary forces.

The amount of energy in ocean waves is huge. It is estimated to have an annual potential of $8000 - 80000\,TWh$ [3]. Other advantages of ocean waves are:

- They have more predictability and a higher concentration of energy compared to other renewable energy sources [4].

- The natural seasonal variability of ocean waves corresponds to the electricity demand of temperate climates [5]. Temperate climates are regions without extremes of temperature and precipitation. They have fluctuation between summer and winter without being extreme.

- Waves can travel long distances with little loss of energy [6].

- Waves can produce power up to 90% of the time which is high compared to wind and solar that generate 20-30 percent of the time [6].

Wave energy converter (WEC) converts wave energy into electricity. The wind gliding over the ocean surface creates waves as it loses a fraction of its kinetic energy to the water beneath it. Thus, a WEC is a device that converts the kinetic and potential energy in the waves into electrical or mechanical energy. Wave energy industry is a pre-commercial
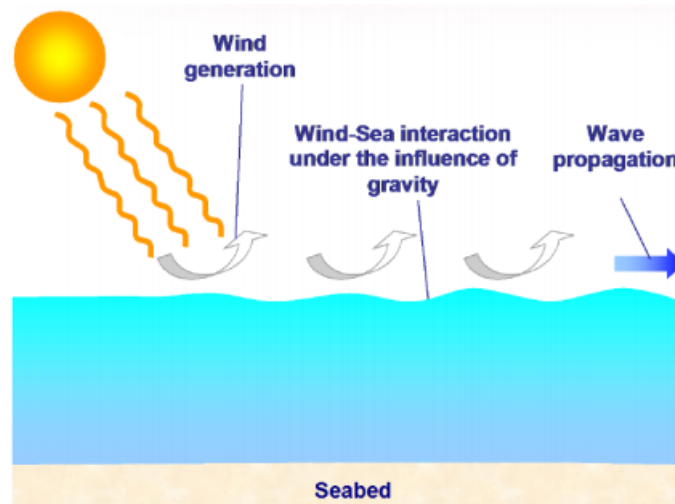
Figure 1.1: Creation of waves from Solar Energy [7]

industry that has technological and non-technological barriers. Technological challenges are those that require technological solutions that may be device-related as well as cabling, data collection, and vessels for deployment. Non-technological barriers among others include financial support, regulatory issues, and environmental impact. The future of wave energy depends for the most part on the technology convergence and efficient performance. However, the economic, environmental and social aspects of its advancement will be very influential [8].

1.1 Classification of Wave Energy Converters (WECs)

There are different ways of classifying WECs. This is due to the completely different principles of operation implemented by WECs. WECs could be divided depending on[9]:

- The distance of the WEC from the bottom of the water and the coast,
  - Onshore, Shallow water (depth $< 50\,m$), Offshore (depth $> 50\,m$)
- The position of the WEC with respect to the sea level,
  - Emerged, Semi-emerged, Submerged
- The size and the orientation of the WEC,
  - Attenuator, Terminator, Point absorber
- The energy capture principle implemented.
  - Oscillating water column (OWS), Overtopping Sys (OTS), Oscillating body

Attenuators are long structures in contrast to the wavelength and they have their axis parallel to the direction of the incident wave. Pelamis 750 kW prototype converter is a typical example of attenuator [11]. Terminators are also long structures but they are positioned perpendicular to the incident wave direction. An example of terminators is a WavePlane

Figure 1.2: A schematic of three WEC types: a point absorber (bottom left), an attenuator (top left) and a terminator (right) [10]

converter [11]. Point absorbers are axis-symmetric. They often have a significantly small diameter compared to the wavelength of the wave. Point absorbers extract energy from all directions by bobbing or pitching action of the device. A schematic of a point absorber, an attenuator, and a terminator are shown at the bottom left, top left and right of Figure 1.2 respectively.

Energy absorption of different kinds of wave energy concepts is discussed by Aurélien Babarit in [12]. Figure 1.3 (a) and (b) shows OWC and OTS with a turbine. Figure 1.3 (c) shows three different kinds of oscillating bodies [13].

Oscillating water column (OWC) is a structure that has an open inlet for water under the sea surface, and thus it keeps an air pocket trapped above a water column, as shown in Figure 1.3 (a). As the water column moves up and down, the trapped air is pressurized and it is forced to flow through a turbine. The kind of turbine used is mostly a Wells turbine but sometimes it could be an Impulse Turbine [14]. Simplicity, robustness and the positioning of moving parts outside of water for a longer part of the material lifetime are advantages of OWCs. Examples of OWC wave energy converters are Pico [15] and LIMPET [16].

Overtopping systems (OTS) collect sea water with incident waves above sea level as shown in Figure 1.3 (b). As more incoming wave crests pass over the slope of the OTS, the reservoir holds more water. The water in the reservoir flows out back to the sea through a low head turbine. As sea waves propagate in all directions and high waves damage coastal areas, the primary target of most researches on OTS is to preserve coastal areas from damage [17] [18]. Examples of OTS wave energy converters are Power Pyramida, Sucking Sea Shaft, Wave Dragon [19] and Tapchan [20].

Oscillating bodies are floating structures while they are rarely fully submerged. They have a buoy or a flap-type device that is moving directly with the sea waves. Thus, the oscillating body could be made of two parts moving relative to each other or only one part moving relative to a fixed reference. Three different types of oscillating bodies are shown in Figure 1.3 (c). Oscillating bodies generally exploit more powerful waves in deep water. Offshore wave energy converters are generally more complex than onshore and shallow water WECs. This complexity added with the challenges associated with mooring and maintenance, hinders their development [22]. However, they are often considered the most promising and hence are most often investigated due to modularity, cost, and
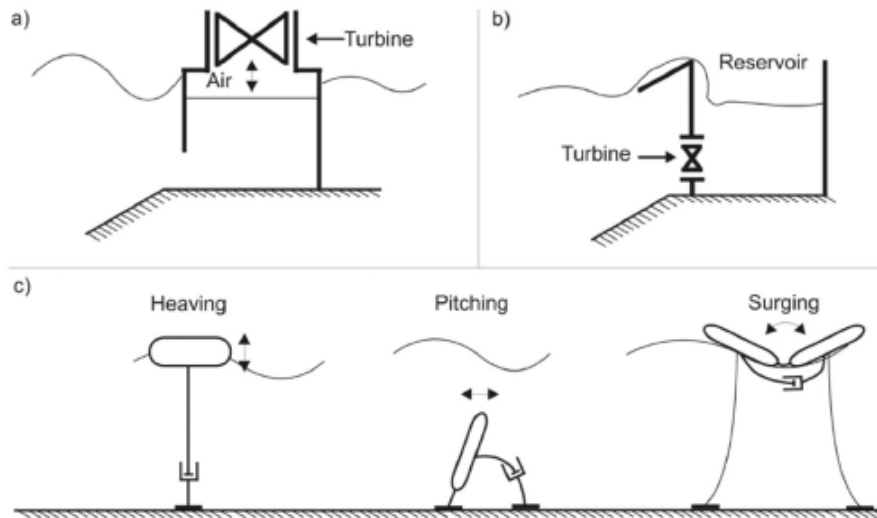
Figure 1.3: WEC's classification according to the energy capture principle [21]

presence of more powerful waves in deep water. Examples of oscillating bodies are Oyster [21], DEXA wave energy converter and WEC developed at Uppsala University [23]. The point absorber is a type of float oscillating body and it is described in detail in the next section.

1.2 The Point Absorber WEC

Point absorbers are WECs which are either floating or submerged to collect the oscillating force of the wave. They are normally found at or near the surface of water. Point absorbers are located in shallow or deep water and usually away from the coastal lines. The distance from the shore is crucial as point absorbers can gather energy from all directions and deeper waters help them to exploit more powerful waves [24]. Examples of point absorber are AquaBuoy [25], WaveBob [26], PowerBuoy [27], SEAREV [28] and Archimedes Wave Swing [29].

Figure 1.4 shows a point absorber wave energy converter made by Open Power Technologies (OPT). It consists of a float, spar and heave plate. The float moves up and down the spar with the incoming waves. The heave plate and the spar are firmly connected to each other. A point absorber could have a single-body or two-body heaving buoys. Single-body heaving buoys are the simplest and the heaving buoy moves against a fixed frame of reference. Two-body heaving bodies solve the difficulties that are created because of the distance between the water surface and the bottom of the sea. The heave plate could be connected to the bottom by mooring and this gives rise to a multi-body system. In this system, the energy is produced from the relative motion of the two bodies oscillating against each other.
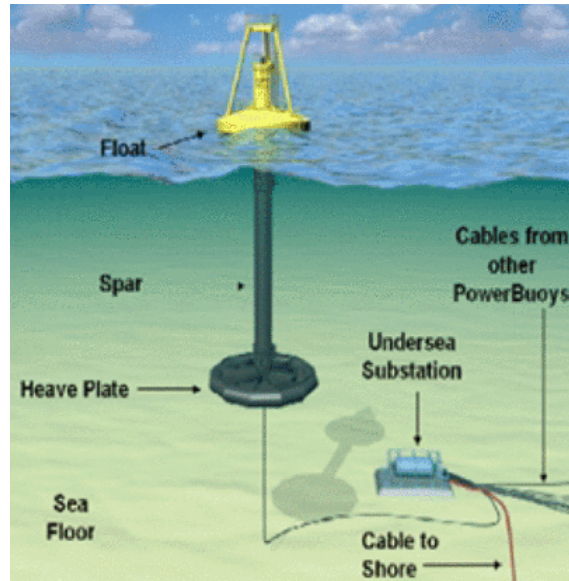
Figure 1.4: A point absorber wave energy converter by OPT [30]

1.3 Wave-to-Wire Model

A Model is a process of building a representation of a real-world object or phenomenon as a set of mathematical equations and allowing respective ideas to be investigated. A model is an abstraction that permits users to concentrate on specified properties of a complex system leaving the non-essential properties out of the system to be analyzed [31].

A Wave-to-Wire (W2W) concept covers the conversion of ocean waves into electricity by a WEC. A Wave-to-Wire model is a useful representation of real-world WECs that have input incoming ocean waves and produce electric power as an output. The electrical power output is mostly injected into the grid. Thus, the word "wave" describes the ocean waves that are the origin of energy while the word "wire" describes the ultimate output of the WEC that is electricity. Taking all the parts of the system into account helps to investigate, optimize and also improve the system as a whole [2]. As the model simplifies the system by eliminating non-essential properties, it does not have the same degree of freedom as the real world point absorber.

The W2W model has four stages: absorption, transmission, generation and conditioning. The model considers the interaction of the hydrodynamic part, the mechanical part and the electrical part with each other, and includes all the characteristic dynamics, energy losses and constraints of different components of the system. This is advantageous in investigating the coupling issues of the system, internal operating requirements of sub-systems as well as advanced control strategies that can be embedded into the model [2]. All these four stages are discussed with reference to a point absorber WEC.

The first stage of W2W is the absorption stage by point absorber. The point absorber WEC is the primary capture system and it is introduced in section 1.2. As the incident waves are irregular, the ability to capture incident waves of the point absorber WEC is

very crucial.

The second stage is the transmission stage. The hydraulic PTO can produce large force at low speed and it is robust. It is the most commonly applied PTO. The hydraulic ram driven by ocean waves pressures the working medium (fluid) to drive the generator. An all-electric PTO can also be applied. Direct-driven permanent magnet synchronous generators connected directly to the point absorber improve the efficiency of the transmission stage by avoiding the complexities.

The third stage of W2W is the generation stage. The generators convert mechanical energy to electrical energy. The generators are divided into linear and rotating type. The Uppsala University WEC and the AWS WEC employ linear permanent magnet generator (LPMG) [13] while the Lifesaver WEC [32] employ rotating permanent magnet generator (RPMG) [2]. Linear generators are on the testing stage but not employed in most advanced WECs [33]–[39]. Some investigations have led to conclude permanent magnet generators have higher power density and higher efficiency [40], [41]. Induction generators employed in generation stage implies a specific mechanical PTO which generate additional power losses reducing the overall efficiency [42]–[45]. A brief description of different types of generators used in the generation stage and the type of generator chosen for simulation are described in chapter 5.

The fourth stage is the conditioning stage. Generally, the output of generators is three-phase electric voltages with variable frequencies. The power conversion is required to inject these currents into electric grids. If the WEC is supplying a DC motor, an AC/DC converter is needed. When the WEC is to be connected to a grid an AC/AC conversion is necessary. One way of achieving this is to use AC/DC and DC/AC converters in series with a DC capacitor in between. DC/DC converters could also be needed to step-up or step-down the electric voltage based on the output voltage of the rectifier and input voltage of the inverter [2]. The main functions of converters in a WEC are [2]:

- To convert from AC to DC or from DC to AC.

- To increase the amount of power captured from WEC.

- To define the quality of the output waveform of electric power to be suited to the grid connection.

Electric power converters are categorized into the following types:

- DC to DC converter - Chopper converts variable DC to constant DC or constant DC to variable DC.

- DC to AC converter - Inverter converts DC to an AC of defined frequency and voltage.

- AC to DC converter - Rectifier converts AC to DC.

- AC to AC converter - Cycloconverter, Matrix converter. They provide AC of a desired frequency and voltage from AC.

Figure 1.5 shows a point absorber WEC, direct drive linear generator and a back-to-back converter system connected to the grid. The rectifier controls the reaction force generated to achieve maximum power capture from sea waves. The inverter keeps the voltage of the DC link constant.
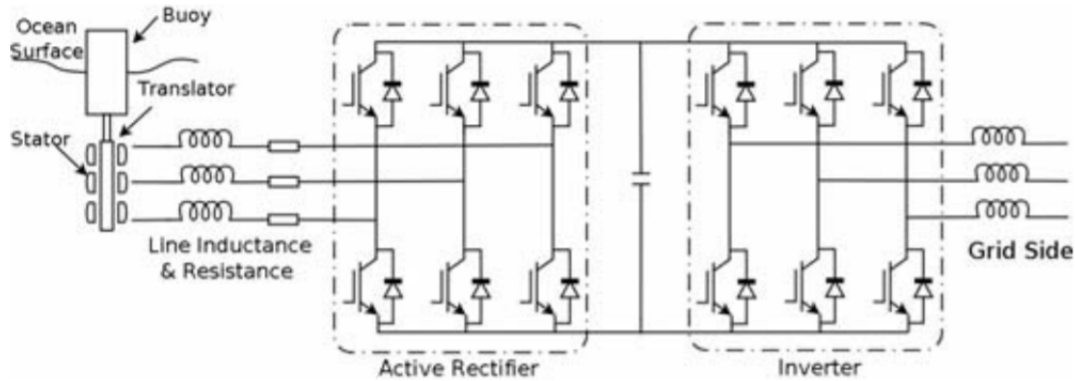
Figure 1.5: The direct drive linear generator and back-to-back power converter system [46]

1.4 Outline of the Thesis

This master thesis is composed of seven chapters. Chapter 1 outlines the basic introduction for wave energy converters and point absorbers in particular including the basics of a suitable modelling approach.

Chapter 2 describes the basic theoretical knowledge of WECs. The wave equation and the forces affecting the wave equation in defining the movement of the point absorbers are discussed. Relevant references are given for further reading.

chapter 3 the modelling of WECs are addressed. The mass-spring-damper system and which wave equation force it represents is discussed. The Space-State analysis of WECs is presented. The electric analogue of WECs is explained. At last, the hydrodynamic model and control of WECs to maximize absorbed energy from incoming waves are briefly discussed.

Chapter 4 explains the control strategies and practical limitations of a point absorber WEC. Two different control strategies for maximizing the power capture are explained. The Wec-Sim model employed and the wave spectrum of the irregular incoming wave are presented. The physical constraints of the point absorber and its effect on the rating of the PTO and effect of efficiency of power conversion are addressed. At last a mathematical analysis for maximizing the power capture without exceeding the peak power limit is presented.

Chapter 5 looks at the details of the modelling and control of permanent magnet synchronous generators (PMSGs). It looks into the Clarke and Park transformation and how PMSGs are modelled in dq frame of reference. The electro-mechanical design of the PMSG is addressed. Afterwards, the decoupling of dq voltages in PMSGs, the voltage

source converter (VSC) and the current controller to be connected to the PMSG are discussed. Field weakening application is explained at the end of chapter 5.

Chapter 6 covers a detailed description of simulations conducted with capping and uncapping of input mechanical power to PMSG in two different control strategies i.e. passive loading and optimum control. The optimal values of damping coefficient and spring coefficient in each type of simulation and their corresponding maximum average electric output power, peak electrical power, peak mechanical power, peak mechanical force, peak velocity, peak stroke distance, rms current, maximum current and rms voltage are presented.

Chapter 7 contains discussion, conclusion and future works. The results of the simulation are interpreted and compared to each other. The maximum possible power capture with limited oversizing of the Power Take-Off is determined. At last, future works are suggested.

1.5 Scope and Limitation of the Thesis

The focus of this thesis is to model a wave-to-wire point absorber wave energy converter (PA3). Two different control strategies are implemented on the WEC. The control strategies are operated on the model to harvest the maximum possible energy from the ocean in irregular sea conditions. At last, the optimal trade-off between high power capture and limited oversizing of the Power Take-Off system is determined. The work of this thesis is a continuation of a semester project I worked last autumn semester, Modelling and Control of Wave Energy Converters [47]. The semester project covers the maximization of the mechanical power output of the point absorber WEC (PA3). Most part of chapter 1 and chapter 2 is taken from the specialization project and small part of chapter 3.

The point absorber 3 (PA3) model used is adapted from the Cruz-Atcheson Consulting Engineers model developed within the EU project IMAGINE and inspired by the CETO3 WEC. Figure 1.6 shows the wave-to-wire Simulink model of PA3. The model is provided by NTNU university. The work of this thesis is building the system from the WEC up to the DC-link. The WEC is connected to a rotating permanent magnet synchronous generator (PMSG) through a recirculating ball screw that converts linear motion to rotational motion. The PMSG is connected to a converter and a dc-link. The two types of control strategies applied are passive loading and optimum control. The two control strategies are analyzed by capping and uncapping the mechanical input power of the generators. The simulation is limited to one sea state and it is an incident irregular wave of Bretschneider spectrum with a significant height of $3.25\,m$ and a peak period of 12 seconds. The constraints on power, end limits and the maximum power that the PMSG can generate, $296.20\,kW$, are taken into account.
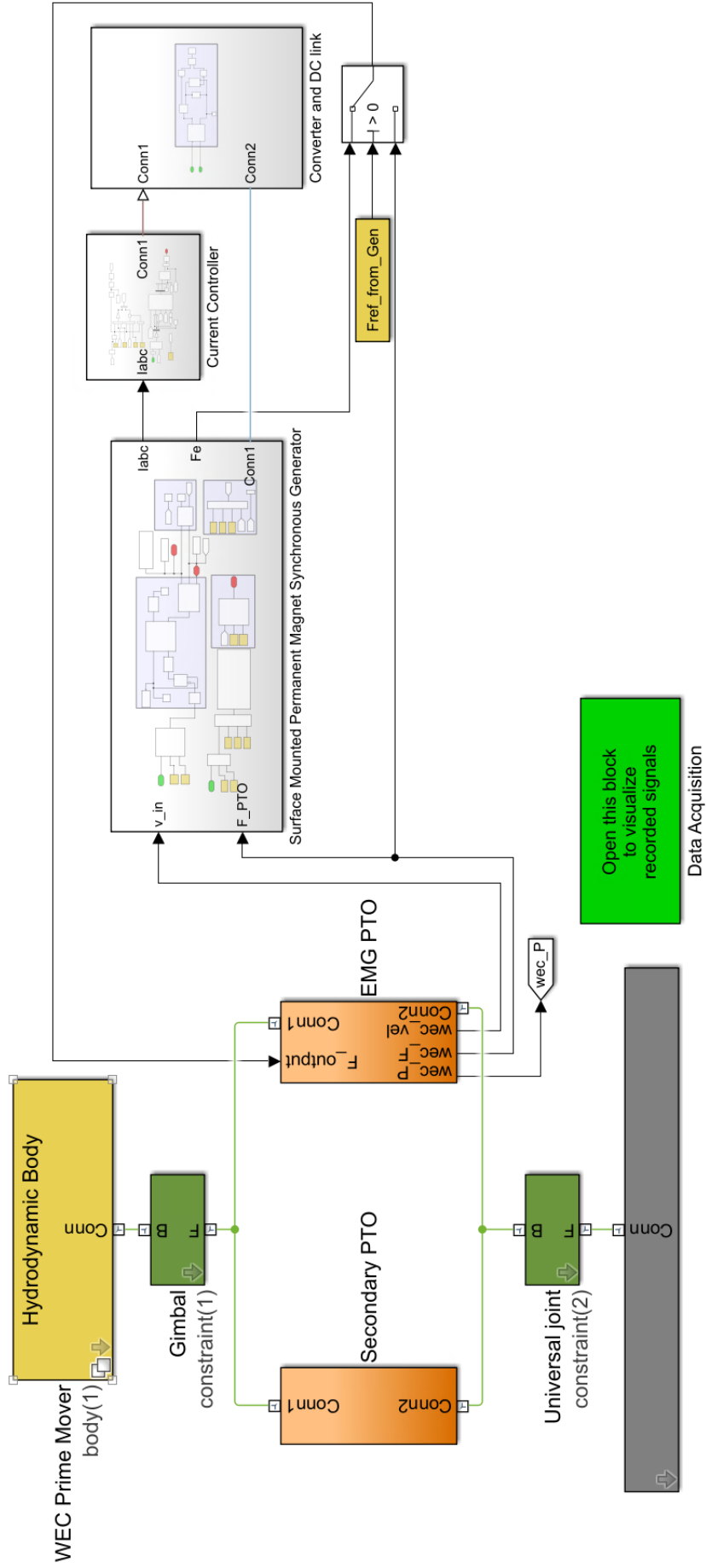
Figure 1.6: Simulink wave-to-wire model

This page intentionally left blank

Chapter 2

Theory

Chapter 2 describes the basic theoretical knowledge of WECs. The wave equation and the forces affecting the wave equation in defining the movement of the point absorbers are discussed. Relevant references are given for further reading.

2.1 Waves and Wave Energy

Waves are described by their length, λ and their height, H as shown in Figure 2.1. h in Figure 2.1 represents the distance between the mean water level and the sea bed while H represents the maximum vertical distance between a trough and a crest of the wave. η represents the instantaneous surface elevation of the wave above or below the mean water level. To describe wave's behaviour precisely, different wave theories depending on the water depth and the steepness of the wave are applied.
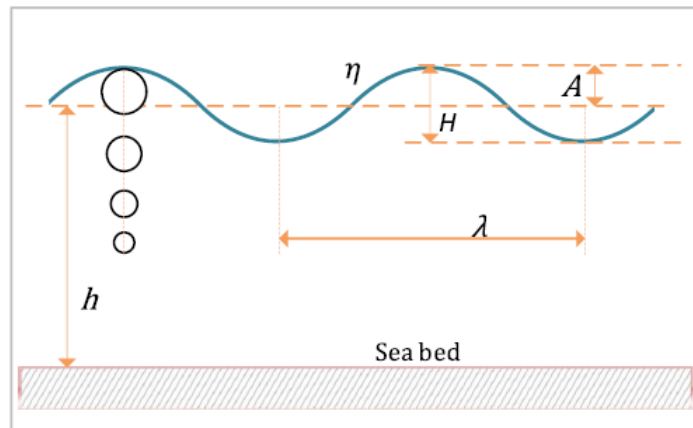
Figure 2.1: Basic characteristics of a wave [21]

For deep waters where the wavelength of the wave is less than half of the depth of the sea bed, $\lambda < 0.5 * h$, 95% of wave energy is trapped between the surface and a depth of $\lambda/4$. As shown in the side of Figure 2.1, the water particles moving in an oscillating pattern underwater have an exponentially decreasing diameters of the circles with an increase of water depth. For deep water, a linear wave theory[1] could be applied. For shallow water

---

[1]Linear wave theory is strictly applicable to waves where the wave height is small compared to the wavelength, λ and the water depth, h. It assumes the fluid flow as inviscid, incompressible and irrotational.

where the ratio of the wavelength to wave height is small, the linear wave theory is not valid. A second-order Stokes theory could be applied [48], [49].

The energy in waves can be divided into kinetic and gravitational potential energy. The amount of energy in a wave depends on the amplitude, $\frac{H}{2}$ and the period, T, of the wave. The power in a wave is directly proportional to the period, T and the square of the amplitude of the wave, $\frac{H^2}{4}$.
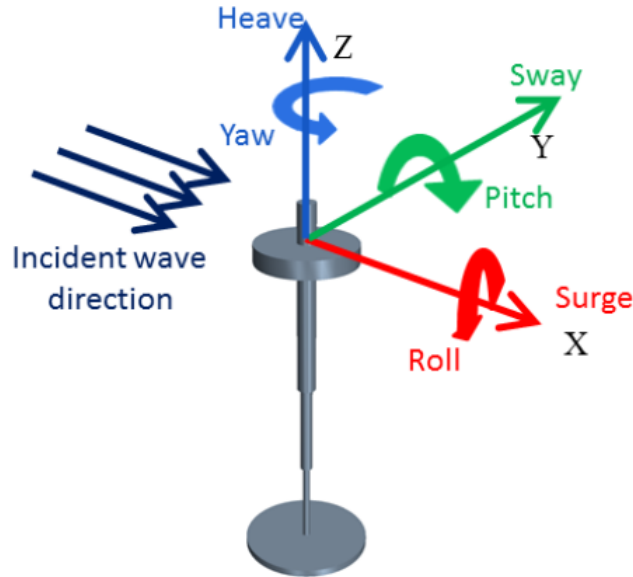
Figure 2.2: Three-dimensional body with six degrees of freedom [50]

A rigid body in three-dimensional space has six independent degrees of freedom. Figure 2.2 shows all six degrees of freedom. When a floating point absorber is subjected to incoming waves, the forces act on all six degrees of freedom. Thus, the point absorber can move in three linear motions which relate to three perpendicular axes i.e. forward and backward (surge), up and down (heave) as well as left and right (sway) with respect to the dominant incident wave direction. The point absorber has also three rotational motions i.e. yaw, pitch (transverse axis) as well as a roll (longitudinal axis).

2.2   Wave Equations

In this thesis, the incoming waves are assumed to be mono-directional and they propagate in the positive x-direction. The system is assumed to be axis-symmetric and all motions are positioned to be in the $(x0z)$ plane. Hence the point absorber interacts with the ocean in Surge, Heave and Pitch direction. Heave has the strongest interaction and it is the principal mode for the extraction of wave energy. There is also a quite strong response in surge while the interaction in pitch is weak [51]. In this section, the point absorber is assumed to have only one degree of freedom, heave, as shown in Figure 2.3.

From Newton's second law:

$$m\ddot{z}\left(t\right) = F_{pe}\left(t\right) + F_{re}\left(t\right) \tag{2.1}$$
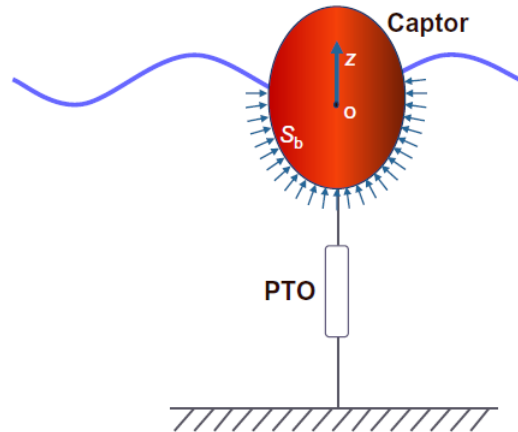
Figure 2.3: Schematic representation of one single degree of freedom (heaving) WEC [52]

where m denotes the total inertia of the system, z its displacement in heave (vertical) direction, F_{pe} the force caused by external pressure i.e. hydrodynamic or hydrostatic and F_{re} reaction force which includes loads connected by the PTO and mooring foundation. In conventional modelling of point absorber, the main forces taken into account are:

- Inertia force: the force resulting from the product of mass and acceleration, $m\ddot{z}$.

- Radiation force: the force acting on the point absorber due to the pressure differences resulted from the fluid displacement of the point absorber in the absence of an incident wave field [52].

- Buoyancy force: the upward force exerted by any fluid on a partly or wholly submerged object in a fluid. The buoyant force is equal to the weight of the fluid displaced by the object.

- Mooring force: Mooring lines can be any type of cable, chain or rope and they connect the point absorber to an anchoring system that is fixed on the seafloor [53]. The power absorption and the dynamics of the system are influenced by the mooring system.

- Viscous damping force: vortex shedding results from the interaction of waves and the point absorber's oscillations. As a result, the viscous damping force represents the power loss due to viscous drag (form drag and skin friction drag).

- Excitation force: this is the force that is applied by the incident waves on a motionless point absorber [52].

- Power Take Off (PTO) force: the PTO force converts the mechanical power to electrical power. To accomplish the work it must work against a fixed reference i.e. a rigid connection to the bottom of the sea and internal inertia. Friction force and other losses in the conversion of power are included in PTO force. The PTO consists of electrical machines as well as uni- or bidirectional converters.

- Other environmental forces: environmental forces are loads like winds, currents and tides. Environmental forces influence the dynamics of conversion systems [54].

According to Newton's second law [55]:

$$m\ddot{z}\left(t\right) + F_R\left(t\right) + F_B\left(t\right) + F_v\left(t\right) + F_l\left(t\right) + F_o\left(t\right) = F_E\left(t\right) + F_{PTO}\left(t\right) \quad (2.2)$$

where m is the mass, F_R is the radiation force, F_B is the buoyancy force, F_v is the viscous force, F_l is the mooring force, F_o is the environmental force, F_E is the wave excitation force and F_{PTO} is the Power Take Off.

In this thesis, only linear terms will be considered as commonly done for this application and as a result viscous, mooring and environmental forces will be neglected. The resulting equation will be:

$$m\ddot{z}\left(t\right) + F_R\left(t\right) + F_B\left(t\right) = F_E\left(t\right) + F_{PTO}\left(t\right) \quad (2.3)$$

Assuming linear hydrodynamics[2][56], equation (2.3) written in frequency domain is [37]:

$$-w^2 z\left(w\right) m + F_R\left(w\right) + F_B\left(w\right) = F_E\left(w\right) + F_{PTO}\left(w\right) \quad (2.4)$$

2.2.1 The Radiation Force

The radiation force is expressed as [54]:

$$F_R\left(w\right) = m_r\left(w\right) a\left(w\right) + R_r\left(w\right) v\left(w\right) \quad (2.5)$$

where $m_r(w)$ is the frequency dependent added mass due to the near-field standing wave, $R_r(w)$ is the radiation resistance related to far-field outgoing waves. $u(w)$ and $a(w)$ are the speed and the acceleration in frequency domain respectively where $a(w) = -w^2 z(w)$ and $v(w) = jwz(w)$.

The radiation force could be linearized [57] and expressed in the time domain:

$$F_R\left(t\right) = m_r\left(\infty\right)\ddot{z} + \int_o^t H_{rad}\left(t - \tau\right)\dot{z}\left(\tau\right) d\tau \quad (2.6)$$

The added mass at infinite frequency is the mass of the fluid accelerated by the point absorber due to the generation of surface waves. Separating the added mass at an infinite frequency from equation (2.6), the remaining part is a convolution integral. This part includes the frequency dependent added mass and the radiation resistance.

A simplified equation can be used to calculate the radiation force if the radiation force has little importance. This is the case if the effects of the losses of the motion of the body are significant compared to the radiation power. Thus, the radiation parameters of equation (2.6) are approximated by constant coefficients [37].

$$F_R\left(t\right) = -A\ddot{z}\left(t\right) - B\dot{z}\left(t\right) \quad (2.7)$$

This expressed in frequency domain is:

$$F_R\left(w\right) = \left(w^2 A - jwB\right) z\left(w\right) \quad (2.8)$$

---

[2]Linear hydrodynamics assumes the amplitude of body oscillations to be small compared with the body size

where A and B are constants representing the added mass due to near-field standing wave and the radiation resistance related to far-field outgoing waves.

2.2.2 The Excitation Force

Excitation force is the product of elevation, η and excitation force coefficient, h_η [54]. The value of the excitation force coefficient depends on body geometry [58]. The excitation force in the time domain can be expressed as:

$$F_E\left(t\right) = \; h_\eta\left(t\right) \; \circledast^3 \; \eta_{ref}\left(t\right) \tag{2.9}$$

expressed in frequency domain:

$$F_E\left(w\right) = \; H_\eta\left(w\right) \; \eta_{ref}\left(w\right) \tag{2.10}$$

When equation (2.10) is used to calculate the excitation force, the elevation of the incident wave is taken as an input. The excitation force could also be calculated by assuming the excitation force to be an input. One way is based on a linearized Morison approach [37].

$$F_E\left(t\right) = A\,\ddot{\eta}\left(t\right) + B\,\dot{\eta}\left(t\right) + k\,\eta\left(t\right) \tag{2.11}$$

where A is the added mass, B is the radiation damping and k is the hydrostatic stiffness.
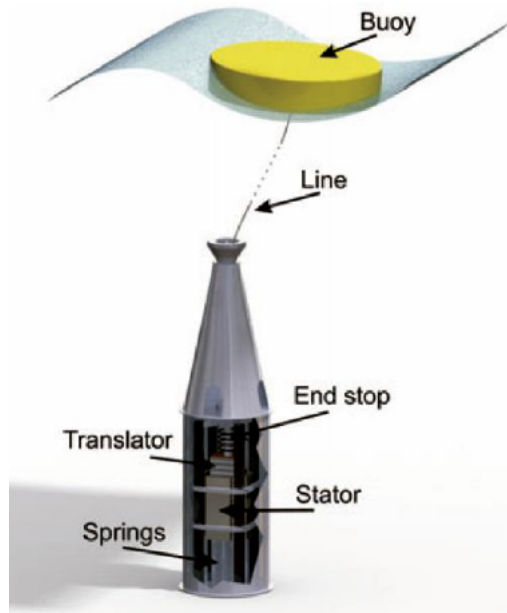
Figure 2.4: A cylindrical direct drive one-body point absorber WEC [59]

---

[3]The sign, $\circledast$, indicates convolution

2.2.3 The Float Buoyancy Force

The buoyancy force is expressed as:

$$F_B\left(t\right) = \ g\rho A_w z\left(t\right) = \ g\rho\pi \ r^2_{float} z\left(t\right) \tag{2.12}$$

where A_w is the water surface area of the point absorber. It is assumed to be circular as shown in Figure 2.4, g is the gravity and ρ is the density of water.

2.2.4 Power Take Off (PTO)

The PTO converts the energy absorbed in the point absorber buoy into electricity. The PTO affects the amount of wave energy absorbed, the size, the mass and the structural dynamics of the wave energy converter [60], [61]. Point absorbers can utilize different kinds of PTO. They could even use cascaded conversion mechanisms.

A linear model of PTO is expressed as:

$$F_{PTO}\left(t\right) = - \ B_{PTO}\dot{z}\left(t\right) - M_{PTO}\ddot{z}\left(t\right) - S_{PTO}z\left(t\right) \tag{2.13}$$

where B_{PTO} is the damping coefficient, M_{PTO} is the spring coefficient and S_{PTO} is the stiffness coefficient.

The different expressions of PTO's forces are presented in chapter 6.

Chapter 3

Modelling of Point Absorber WEC

Chapter 3 address the modelling of WECs. The discussion of the mass-spring-damper system and the wave equation forces it represents are discussed. The Space-State analysis of WECs is presented. The electric analogue of WECs is explained. At last, the hydrodynamic model and control of WECs to maximize absorbed energy from incoming waves are briefly discussed.

In modelling part to ease the application, the considered WEC is a spherical semi-submerged point absorber WEC as shown in Figure 3.1. It is assumed to have a single degree of freedom as discussed in section 2.2 and it is directly connected to an electric PTO.
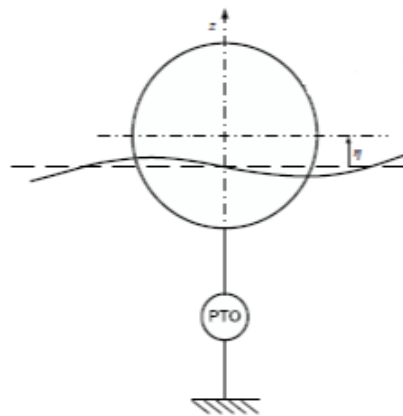
Figure 3.1: A Simplified model for a directly coupled point absorber in heave [4]

3.1   Mass-Spring-Damper system

A point absorber can be represented by a mass-spring-damper system. This is helpful in understanding the control and transfer of power [62]. This analysis is strictly solid for monochromatic[1] waves. Figure 3.2 shows the mass-spring-damper system where a mass m is suspended and an external force is acting on the mass upwards.

---

[1]A monochromatic wave is a wave with a single wavelength and frequency.

Newton's second law reads:

$$m\ddot{z} = F + F_D + F_S \tag{3.1}$$

where m is the mass, F the external force, F_D the damper force and F_S the spring force where $F_D = -R\dot{z}$ and $F_S = -Sz$.

If the damper and spring are assumed to have linear characteristics, then the stiffness S and the mechanical resistance R are constants. Then, equation (3.1) can be rewritten as:

$$m\ddot{z} + R\dot{z} + Sz = F \tag{3.2}$$

where an overdot is applied to denote the differentiation of variables with respect to time t.

When representing a point absorber by a mass-spring-damper system, equation (3.2) can be compared to equation (2.3). The oscillation of WEC has more complicated dynamics than the mass-spring-damper system. However, equation (3.2) can be compared to equation (2.3) by linearization of radiation and buoyancy forces. The radiation and buoyancy forces are similar to damping and stiffness forces respectively [63]. The radiation force is not explicitly related to the incoming waves. However, it is linearly related to the motion of the point absorber. Assuming the incoming wave to be a monochromatic and regular wave, the radiation force can be expressed as $F_R = -R\dot{z}$ where R is the radiation coefficient matrix [64], [65]. The buoyancy force can be expressed as $F_B = -Sz$ where S is $g\rho A_w$, depending on the geometry of the float. At last, the external force F in equation (3.2) represents the excitation and PTO force, $F_E + F_{PTO}$, in equation (2.3).

3.1.1 Free Oscillation

If the external force F applied on mass m in Figure 3.2 is zero and the mass m is released at a certain distance from $z = 0$, the system is in free oscillation.
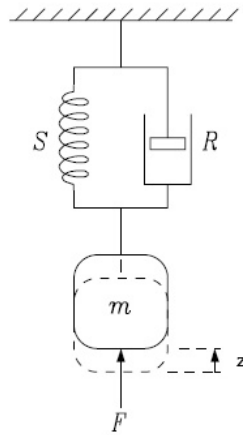
Figure 3.2: Mechanical oscillator composed of a mass-spring-damper system [62]

The system's initial energy is [62]:

$$W_C = W_{po} + W_{ko} = S\frac{z_o{}^2}{2} + m\frac{v_o{}^2}{2} \tag{3.3}$$

where the subscript o indicates the initial value of the corresponding variable. The energy is the sum of potential and kinetic energy. By solving equation (3.3), the general solution is:

$$z = (C_1 \cos w_d t + C_2 \sin w_d t) e^{-\delta t} \tag{3.4}$$

where the damping coefficient, the undamped natural angular frequency and the damped angular frequency are $\delta = R/2m$, $w_o = \sqrt{(S/m)}$ and $w_d = \sqrt{w_o^2 - \delta^2}$ respectively.

Constants C_1 and C_2 are determined from the initial conditions in equation (3.4). Assuming damping force to be zero, the oscillations are purely sinusoidal with a natural period of the oscillation $2\pi/w_o$. The free oscillation described in equation (3.4) is an exponentially damped sinusoidal oscillation with a period of $2\pi/w_o$. The power loss in the system is due to damping resistance R and it is a ratio of $1 - exp(-4\pi\delta/w_d)$ of the energy [62].

A quality factor Q can be defined as a ratio between the stored energy and the average energy loss. The quality factor in a time interval of $1/w_d$ is:

$$Q = (1 - e^{-2\delta/w_d})^{-1} \tag{3.5}$$

If the damping coefficient δ is small, the resulting quality factor is large.

The case of forced oscillation is not discussed in this master thesis. But, it is thoroughly discussed in the book "Ocean Waves and Oscillation Systems" by Johannes Falnes chapter 2 [62].

3.2 Space-State Analysis

The standard form of expressing state equations is as a set of n coupled first-order ordinary differential equations. The time derivative of each state variable is defined by the state variables $z_1(t),...,z_n(t)$ and the system inputs $u_1(t),...,u_r(t)$ [66].

$$\begin{aligned}
\dot{z}_1 &= f_1(z, u, t) \\
\dot{z}_2 &= f_2(z, u, t) \\
\vdots &= \vdots \\
\dot{z}_n &= f_n(z, u, t)
\end{aligned} \tag{3.6}$$

where $z_i = dx_i/dt$ and $f_i(z, u, t)$ for $i = 1, ..n$ could be a generally non-linear time varying function of the system input, output and state variables. In vector notation equation (3.6) can be expressed:

$$\dot{\mathbf{z}} = \mathbf{f}(\mathbf{z}, \mathbf{u}, t) \tag{3.7}$$

where $\mathbf{f}(\mathbf{z}, \mathbf{u}, t)$ is a vector function with n components $f_i(\mathbf{z}, \mathbf{u}, t)$.

To perform state space analysis, the second order differential equation of equation (3.2) can be written as the following two first order differential equations:

$$\dot{z}_1 = z_2 \qquad \dot{z}_2 = -\frac{R}{m}z_2 - \frac{S}{m}z_1 + \frac{1}{m}u_1 \tag{3.8}$$

where the state variables are $z_1(t) = z(t)$ and $z_2(t) = u(t) = \dot{z}(t)$ and the input is $u_1(t) = F(t)$. Written in matrix form this would be:

$$\begin{bmatrix} \dot{z}_1 \\ \dot{z}_2 \end{bmatrix} = \begin{bmatrix} 0 & 1 \\ -S/m & -R/m \end{bmatrix} \begin{bmatrix} z_1 \\ z_2 \end{bmatrix} + \begin{bmatrix} 0 \\ 1/m \end{bmatrix} u_1 \tag{3.9}$$

Representing equation (3.9) in state-variable form:

$$\dot{z} = Ez + Fu \tag{3.10a}$$
$$y = Gz + Lu \tag{3.10b}$$

Applying Laplace transform on equations (3.10a) and (3.10b):

$$sZ(s) = EZ(s) + FU(s) \tag{3.11a}$$
$$Y(s) = GZ(s) + LU(s) \tag{3.11b}$$

Substituting $Z(s)$ from equation (3.11a) into equation (3.11b):

$$Y(s) = \left[G(sI - E)^{-1}F + L \right] U(s) \tag{3.12a}$$
$$Y(s) = H(s) * U(s) \tag{3.12b}$$

Assuming the variables E, F, G and L in the block diagram, Figure 3.3, to be time variant, the solution for state-variable $z(t)$ and the corresponding solution for $y(t)$ are [62]:

$$z(t) = e^{E(t-t_o)} z(t_o) + \int_{t_0}^{t} e^{E(t-\tau)} Fu(\tau) \, d\tau \tag{3.13}$$

$$y(t) = Ge^{E(t-t_o)} z(t_o) + \int_{t_0}^{t} Ge^{E(t-\tau)} Fu(\tau) \, d\tau + Lu(t) \tag{3.14}$$

The block diagram of equation (3.12a) is shown in Figure 3.3. The detailed step to reach equation (3.13) and (3.14) are shown in appendix A.1.
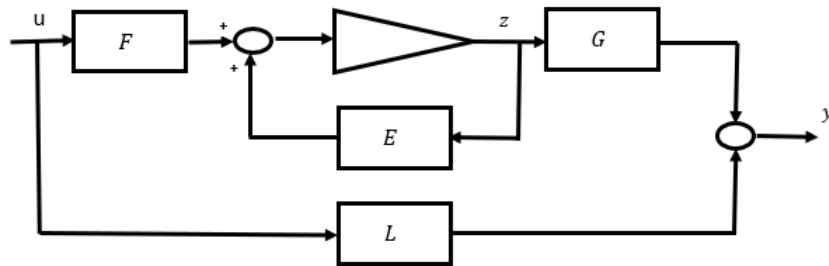
Figure 3.3: Linear time-invariant state-space model

3.3 Electric Analogue of WEC

The mechanical system of Figure 3.1 is analogue to an electric circuit shown in Figure 3.4. The inductance, resistance and capacitance of WEC correspond to m, R and $1/S$ of Figure 3.1 respectively. Thus, the voltage source, the electric charge on the capacitor

and the electric current are analogous to the force F, position z and velocity v respectively.

Comparing the electric analogue to the forces mentioned in section 2.2. The supply voltage corresponds to the excitation force F_E while the current corresponds to the buoy velocity. The resistance R_{wec}, the inductance L_{wec} and the inverse of capacitance $1/C_{wec}$ correspond to the total buoy damping, the mass of the point absorber and the hydrostatic stiffness respectively. The representation of electric analogue is restricted to sinusoidal incoming wave as the total buoy mass which includes the added mass and the total damping which includes damping from the radiation force, is frequency dependent [67].
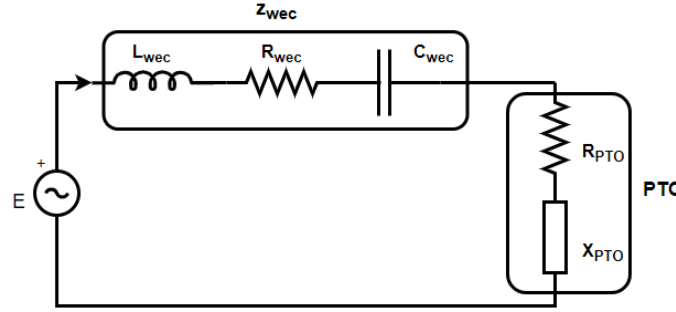
Figure 3.4: Electric analogue of a point-absorber WEC [68]

The PTO is represented by a series connection of equivalent resistance, R_{PTO} and equivalent reactance, X_{PTO}. The sign of the value of reactance depends if the point absorber is inductive or capacitive. If the value of reactance is negative, the device is inductive and the value is equivalent to an added mass. If the value of reactance is positive, the device is capacitive and the value is equivalent to a spring constant [68].

3.4 Hydrodynamic Model

The hydrodynamic model is employed to describe the interaction between WEC and the incoming waves [62]. Linear waves are described using linear wave theory while irregular waves are constructed by superimposing randomly phase-shifted sinusoidal waves of different heights and periods. The modelling of the hydrodynamic system is created to describe the motion of the heave of the point absorber WEC. Figure 3.5 shows the forces described in chapter 2.

From equation (2.3) we have:

$$F_i\left(t\right) + F_R\left(t\right) + F_B\left(t\right) = \ F_E\left(t\right) + F_{PTO}\left(t\right) \tag{3.15}$$

Thus, the hydrodynamic model could be written as[69]:

$$(M + m_r\left(\infty\right))\ddot{z}\left(t\right) + \int\limits_{-\infty}^{t} H_{rad}(t-\tau)\dot{z}\left(\tau\right)d\tau + Kz\left(t\right) = F_E\left(t\right) + F_{PTO}\left(t\right) \tag{3.16}$$

where M is the mass of the device including the generator's inertia, $m_r\left(\infty\right)$ is the added mass when frequency approaches infinity, H_{rad} is the radiation impulse response function
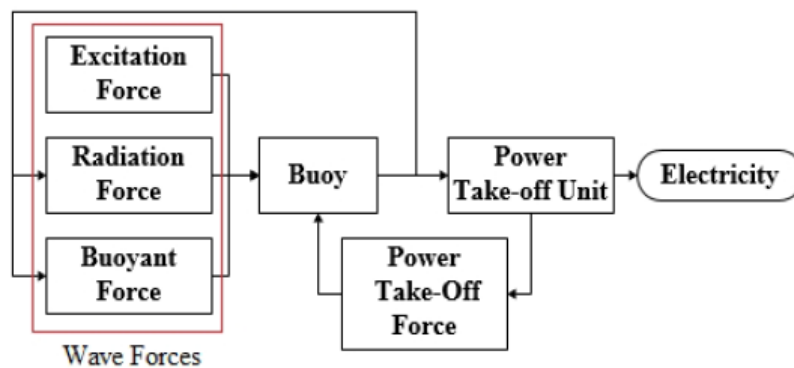
Figure 3.5: Forces acting on the heave axis of a point absorber [30]

(RIRF) and K is the hydrodynamic stiffness.

The hydrodynamic model written in frequency domain is [69]:

$$-w^2 \left(M + m_r \left(w \right) \right) z \left(w \right) + jwB \left(w \right) z \left(w \right) + Kz \left(w \right) = F_E \left(w \right) + F_{PTO} \left(w \right) \quad (3.17)$$

where $m_r(w)$ is the frequency dependent added mass, $B(w)$ is the mechanical damping and w is the angular frequency of the incident wave.

Chapter 4

Control Strategies and Practical Limitations

Chapter 4 explains the control strategies and practical limitations of a point absorber WEC. Moreover, two different control strategies for maximizing the power capture are explained. The Wec-Sim model employed and the wave spectrum of the irregular incoming wave are presented. The physical constraints of the point absorber and its effect on the rating of the PTO and effect of power capping are addressed. At last a mathematical analysis for maximizing the power capture without exceeding the peak power limit is presented.

4.1 Control Strategies

Objects oscillating in water generate waves and generally, good wave makers are good wave absorbers [62]. Therefore to absorb wave energy, water has to be displaced in an oscillatory manner with the correct timing. Absorbing the wave's energy means removing energy from waves. As energy is removed from the passing wave, the resulting wave after the encounter with the oscillating device is a wave of reduced or zero amplitude. In order to cancel or reduce waves by the oscillating body, the oscillating body must oscillate in opposition to the passing wave. Therefore it is necessary to generate waves that interfere destructively to passing waves in order to absorb energy. The destruction of a wave requires the creation of another wave.

The motion of the point absorber determines the amount of energy absorbed. The force exerted by the PTO can control the motion of the point absorber. The point absorber moves to absorb energy from the incident waves by destructive interference. The point absorber must radiate waves with appropriate amplitude as well as phase to absorb maximum energy [70]. It is theoretically possible to absorb 100% of the wave energy as shown in Figure 4.1 d. For a symmetrical body oscillating in only one direction, for instance, the vertical oscillation, it is theoretically possible to absorb a maximum 50% of wave energy as shown in 4.1 b. The 50% limit is described in detail in the book, "Ocean Waves and Oscillating Systems" written by Johannes Falnes chapter 6. However, a non-symmetrical body oscillating in only one mode of direction may absorb almost all of the energy of the incident wave [62].
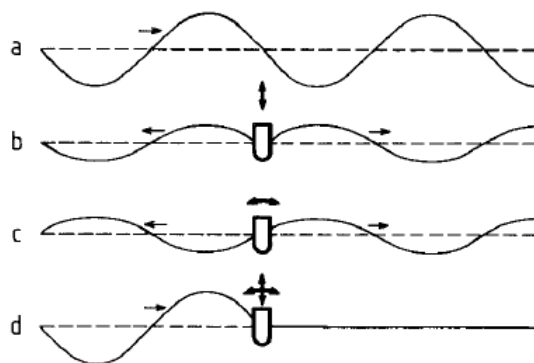
Figure 4.1: Curve 'a' illustrates an undisturbed incident wave. Curve 'b' illustrates symmetric wave generation by means of a straight array of evenly spaced small floating bodies oscillating up and down. Curve 'c' illustrates the anti-symmetric wave generation. Curve 'd' represents the superposition of curve 'a', 'b' and 'c', illustrating the complete absorption of wave energy [62]

A heaving point absorber radiating circular waves against a plane incident wave is shown in Figure 4.2. Point absorbers are very small compared to the wavelength of the waves. The circular waves interact destructively with the plane incident waves. Optimum oscillation of the point absorber is necessary for maximum energy absorption. The optimum oscillation has an optimum amplitude and an optimum phase of the oscillation. This could be described by referring to Figure 4.1. Figure 4.1 d illustrates the total absorption of energy of the incoming wave by an oscillating object. This is the superposition of the curves 'a', 'b' and 'c'. Curve 'a' illustrates an undisturbed incident wave. Curve 'b' and curve 'c' illustrates a wave generation by small floating bodies oscillating vertically and horizontally respectively.

The amplitude of the radiated waves of curve 'b' and 'c' to the left and right of the floating body are equal to each other but exactly half of the amplitude of the incident wave curve 'a'. The waves of curve 'b' and 'c' to the right of the floating body are in phase with each other but they have a $180°$ phase shift from curve 'a'. Thus, the sum of the curve 'a', 'b' and 'c' results into a destructive interference of the incident wave as seen to the right of the floating body in Figure 4.1 d, total absorption of energy. The waves of Curve 'b' and 'c' to the left of the floating body are equal but they have $180°$ phase shift from each other. Thus, the sum of curve 'b' and 'c' becomes zero resulting in the sum of the curve 'a', 'b' and 'c' to be equal to curve 'a' as shown in Figure 4.1 d.

For point absorber WEC with only one mode of oscillation, the final wave results from the superposition of curve 'a' and 'b'. The resulting radiating waves to the left and right of the point absorber propagate with half of the amplitude of the incident wave. Wave energy is proportional to the square of wave amplitude [71]. Hence, 25% of the incident wave energy is sent to the right and another 25% is sent to the left of the point absorber. The theoretically maximum energy of 50% is absorbed by the point absorber WEC.

The optimum phase conditions of a one-mode oscillating system occur when the oscillating body is at resonance with the incoming incident wave. This happens when the natural frequency of the oscillating body is equal to the wave frequency of the wave. This in turn means, the velocity of the oscillating body is in phase with the excitation force of the
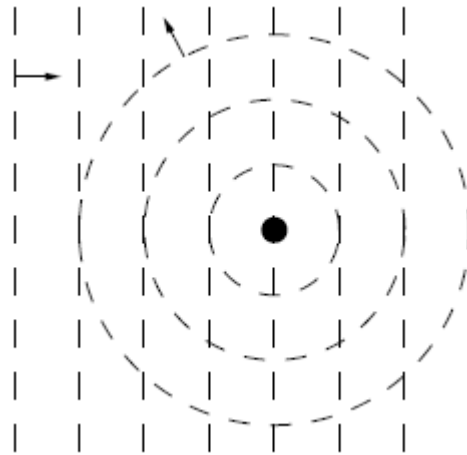
Figure 4.2: Wave pattern interference of two waves seen from above. As a point absorber absorbs energy, it creates a circular wave radiating away from the point absorber [62].

wave [62].

The main goal of controllers in wave energy conversion is to produce the maximum power output possible while constraints are taken into account. The constraint could result from a Power Take-Off system or other physical constraints. The physical constraints could limit the force, displacement, speed and power of the WEC. The physical size of a point absorber is very small compared to the wavelength of the incident waves. The high power to volume ratio results in cost reduction. However, point absorbers have narrow frequency response and ocean waves have a wide range of frequency band that varies with time and season. This could result in poor performance if the device is not actively controlled [72]. Thus, there is an optimum trajectory movement the WEC should follow that is determined by the incident wave to maximize the energy absorbed.

The optimum trajectory movement of the WEC is defined by the combination of physical inertia, stiffness, damping and PTO forces. The values of physical inertia, stiffness and damping are defined in the design of the WEC. Therefore, the main principle of WEC control is to employ the PTO forces to obtain the optimum power extraction condition. The optimum power extraction is reached by changing the amplitude and/or phase of the motion of the WEC point absorber. This results in increased complexity of the system and lowers the reliability and increases the maintenance [60].

The energy absorbed by point absorber is maximized if the resonant frequency coincides with the dominant frequencies of the incident waves. The wave frequencies which the point absorber encounters are generally lower than the resonant frequency of the WEC. In order to increase the energy absorption by employing resonance techniques, the system must be provided with a supplementary mass or it must be provided with a negative spring constant by the flow of reactive power [73].

When considering an unconstrained point absorber to achieve the optimum power extraction, two conditions are important [60]:

  • The velocity of heave and the dynamic pressure of the incoming incident wave must

be in phase.

- At resonance condition, the amplitude of the incoming incident wave must be twice the amplitude of the radiated wave of the point absorber WEC.

There are different control algorithms for a heaving semi-submerged sphere. These include passive loading, optimum control, approximate optimum velocity tracking, phase control by latching and clutching, and model-predictive control. Most of the control strategies could be seen as velocity tracking as they can be expressed with a formula for optimum velocity [2].

Two types of control strategies are examined. They are passive loading and optimum control.

4.1.1 Passive Loading

Passive loading is the simplest and most common strategy. In passive loading, the PTO force is proportional to the buoy velocity and the damping coefficient, B_{PTO}, is the coefficient of proportionality. The amplitude of the WEC trajectory motion is changed to maximize the power extracted. Representing the WEC with its equivalent impedance as in Figure 3.4, the optimum value of B_{PTO} is the absolute value of the point absorber's electrical equivalent impedance, $B_{PTO}(w) = \sqrt{R_{wec}^2(w) + X_{wec}^2(w)}$. The damping coefficient also known as mechanical damping is frequency dependent.

As the PTO force and the speed are proportional and the damping factor is always greater than zero, the power is always positive and flows only one way. The PMSG works only as a generator.

$$F_{PTO}\left(t\right) = -B_{PTO}\,\dot{z}\left(t\right) \tag{4.1}$$

The minus sign is due to the way F_{PTO} is defined in equation (2.2).

4.1.2 Optimum Control

Optimum Control also known as complex-conjugate or reactive control is a way of adjusting the point absorber to react as in resonance over a broad frequency band. The PTO force has one component proportional to the buoy acceleration and another component proportional to the buoy velocity. The part of PTO force proportional to the buoy acceleration is the reactive part, inertia. The part PTO force proportional to the buoy velocity is the real part, damping. Both components result in control of amplitude and phase of the motion required to extract the absolute maximum power available. As the force and speed are not proportional, the resulting flow of power is bidirectional and the PTO mechanism becomes more complex [69].

Representing the WEC with its electrical equivalent impedance as in Figure 3.4, the optimum value of X_{wec} for sinusoidal incoming waves is the conjugate of X_{PTO} i.e. $R_{PTO} = R_{wec}$ and $X_{PTO} = -X_{wec}$. This is in order to cancel out the reactive part

and the resonance achieved results in absorption of maximum power available. The value of $F_{PTO}(t)$ is given by:

$$F_{PTO}(t) = -B_{PTO}\,\dot{z}(t) - M_{PTO}\,\ddot{z}(t) \tag{4.2}$$

where B_{PTO} is the damping coefficient and M_{PTO} is the spring coefficient. The minus sign is due to the way F_{PTO} is defined in equation (2.2). $B_{PTO} = R_{wec}(w)$ and $M_{PTO} = -X_{wec}(w)/w$. The detailed steps to obtain the expression for B_{PTO} and M_{PTO} are shown in Appendix A.5.

4.2 Wec-Sim Model

Wec-Sim (Wave Energy Converter SIMulator) is an open source wave energy converter (WEC) Simulation tool. The code of Wec-Sim is developed in MATLAB/Simulink by using a multi-body dynamics solver Simscape Multibody [74]. Wec-Sim model devices are comprised of rigid bodies, Power Take-Offs and mooring systems. Simulations are performed in the time domain and they are solved by the governing equations of motion presented in chapter 2 in six degrees-of-freedom.
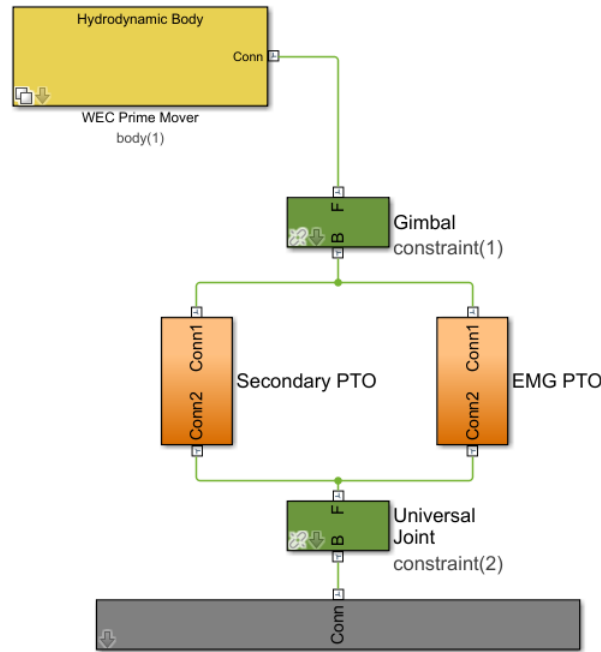
Figure 4.3: PA3 Wec-Sim model schematic [75]

The point absorber WEC model used in the simulation is a point absorber 3 (PA3). Point absorber 3 (PA3) is adapted from Cruz-Atcheson Consulting Engineers. It is developed within the IMAGINE project and inspired by the CETO3 WEC [76], [77]. The point absorber is a single-body WEC and bottom referenced. The linear motion in heave is changed to rotational motion by a roller ball screw directly connected to PMSG and placed in the bottom of a spar [78]. The rated power of the PMSG is $250\,kW$ and its parameters are shown in table 5.2 section 5.3. The buoy has physical dimensions of height, diameter, displacement and mass of $6.5\,m$, $9.1\,m$, $329\,m^3$ and $76.9\,t$ respectively. The PA3 Wec-

Sim model schematic is shown in Figure 4.3.

As shown in Figure 4.3, the EMG PTO and auxiliary subsystems are placed between the prime mover and the seabed. The PA3 model has one universal joint, seabed and one gimbal joint, prime mover. The PA3 subsystem consists of one degree of freedom (1DoF) translational PTO block which is capable of accepting an external actuation force. The actuation force blocks are modified to take into account the losses in the EMG PTO block, the maximum power constraint and the stroke range in the auxiliary block. The main PTO variables are the damping coefficient, spring term and the friction losses. The controller and the EMG take inputs of PTO position, velocity and acceleration. The EMG PTO model is shown in Figure 4.4. The auxiliary subsystem handles the tension force and employs end-stops. The maximum distance of stroke length is limited because of the finite length of hydraulic rams. Therefore it is important to have a deceleration cushion at both ends of the stroke. The auxiliary subsystem produces forces that emulate the physical system. These consists of the constant force produced to oppose the buoyancy of prime mover and a force profile that simulates the end-stops. A quadratic formulation is applied to employ a resistive force near the minimum and the maximum stroke of the WEC. It dissipates kinetic energy gently while reducing the mechanical damage that could occur.
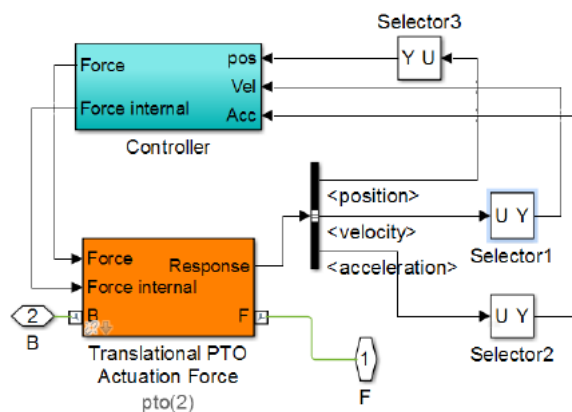
Figure 4.4: PA3 Wec-Sim EMG PTO model [75]

4.2.1 Wave spectrum of the incoming wave

It is easy to notice that waves on sea surfaces are not simple sinusoidal curves. The surface appears to be a superposition of random waves of various lengths and periods. By making simplifications, the distribution of wave energy in different wave frequencies and wavelengths are given by a wave spectrum. Specific parameters such as significant wave height, peak period, wind speed, fetch lengths characterise a wave spectrum [50]. The general form of the wave spectrum available in the Wec-Sim is given:

$$S(f, \theta) = S(f) D(\theta) \tag{4.3}$$

where $S(f)$ is the wave power spectrum, f the wave frequency in Hertz, $D(\theta)$ the directional distribution and θ the wave direction in degrees.

There are many different kinds of wave spectrums that are employed in the offshore industry. The wave spectrum chosen in the simulation of Wec-Sim is the Bretschneider spectrum [50], [79]. Bretschneider spectrum is based on two-parameters: significant height and peak wave frequency. The parameters strongly depend on the wind speed but they also depend on wind direction, fetch as well as the location of storm fronts [50]. The wave spectrum is given by [79]:

$$S\left(f\right) = \frac{5}{16}\frac{w_p^4}{w^5} * H_s^2 * exp(-\frac{5}{4}w)S\left(f\right)D\left(\theta\right) \tag{4.4}$$

where H_s is the significant height and w_p is the $2\pi/T_p$ where T_p is the peak period. The Bretschneider spectrum parameters are a peak period of 12 seconds and a significant wave height of $3.25\,m$. Figure 4.5 shows the Bretschneider spectrum for the incoming wave. The MATLAB script for constructing the Bretschneider spectrum of waves is found in Appendix B.1.
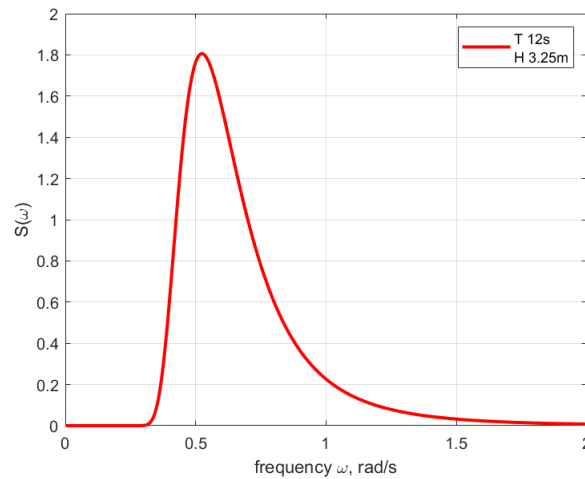
Figure 4.5: Breitschneider spectrum of a wave with a significant height of 3.25m and a peak period of 12 seconds

4.3   Physical Constraints

The electrical system of the point absorber WEC, in general, is composed of an electric machine controlled by a power electronics and a grid interface power electronics. This master thesis examines the system up to a DC-link and as such, the effect of grid interface power electronics are not addressed. The description and parameters of the electrical generator and the converter employed in this thesis are expressed in chapter 5. The control strategy plays a crucial role in deciding the selection as well as the topology and rating of the electrical system [80]. Maximizing the average power produced by the WEC requires a variable speed electrical machine. Control strategies that implement bidirectional power flow require a bidirectional power electronics converter and also the operation of an electric machine as a motor and a generator.

4.3.1 Effect of control strategies on PTO rating

The average and peak power are the main parameters that are considered in the design of the PTO and the performance evaluation of the WEC [80]. The peak and average extracted power are dependent on the control strategy applied and as such, the rating of the PTO system components depend on the control strategy employed. Different control strategies result in different distinct peak to average power ratio. The rating of electric machines and converters limit the maximum power the system can handle. Electrical machines can operate transiently at high peak power since their time constants are generally in the range of minutes. On the contrary, power electronics converters have a short thermal time constant in the order of hundreds of milliseconds. This means the rating of power converters of wave energy devices must be higher than the peak power output [81]. Thus, the performance of WEC is often evaluated from the ratio of peak to average power [82], [83]. This is very applicable as it is relevant to deal from the design of the PTO up to the WEC-grid connection [80].

4.3.2 Effect of efficiency of power conversion

The efficiency of electrical machines and power converters are affected by several factors including rotational speed and loading factors [69]. It is difficult to have a specific evaluation of the effect of efficiency but a simplified efficiency curve as a function of load factor can be used, shown in Figure 4.6. A load factor is the ratio of extracted power to the rated power. As shown in Figure 4.6 the efficiency decreases quickly when the extracted power decreases. This creates a different influence on the rating of the electric machines and power converters.

There are two contradicting aspects that affect the value of the maximum average extracted power. The higher rating of electric machines and power converters ensures extraction of power from peak power values. On the contrary, higher rating significantly increases the losses due to nonlinear efficiency. Optimum control generates much higher peak power and thus, the low load operating conditions results in higher losses due to nonlinear efficiency as well as due to the bidirectional flow of power.

4.3.3 Mathematical Analysis

A mathematical approach can show how the WEC control strategy could be tuned to respect the maximum power constraint. In cases where the incident waves are low amplitude and low period, it is possible that application of optimum control does not reach peak power. In this case, the maximum extracted average power is reached in resonance.

When a constraint of peak power is imposed on the system, it is theoretically viable to calculate the optimal values of R_{wec} and X_{wec}. Referring to an electric analogue of a point absorber in Figure 3.4, the average power produced is [84]:

$$P_{mean} = \frac{E^2 R_{PTO}}{(R_{wec} + R_{PTO})^2 + (X_{wec} \pm \frac{R_{PTO}\sqrt{1-cos\varphi_{PTO}^2}}{cos\varphi_{PTO}})^2} \tag{4.5}$$
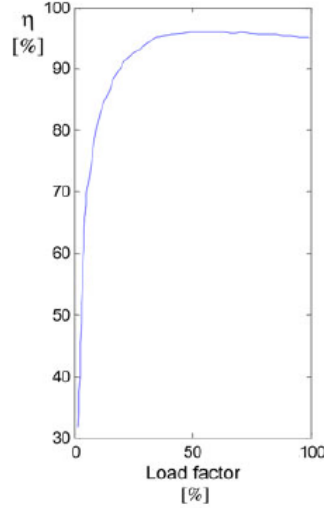
Figure 4.6: The efficiency of electrical and electronic devices as a function of loading factor [69]

where the generator voltage E corresponds to wave excitation force, F_e and the load power factor $cos\varphi_{PTO}$ is:

$$cos\varphi_{PTO} = cos\left(tan^{-1}(\frac{X_{PTO}}{R_{PTO}})\right) \tag{4.6}$$

The detailed calculation to obtain equation (4.5) is shown in appendix A.2.

Expressing the peak power the system can be handled as a function of average power:

$$P_{peak} = P_{mean}(1 + \frac{1}{cos\varphi_{PTO}}) \tag{4.7}$$

Once the peak power is known, by inserting equation (4.5) into equation (4.7) a second order polynomial with a variable of R_{PTO} having a parameter of $cos\varphi_{PTO}$ is obtained [84].

$$R_{PTO}^2(\frac{P_{peak}}{cos\varphi_{PTO}}) = R_{PTO}\left[2P_{peak}R_{wec} + 2P_{peak}X_{wec}\sqrt{\frac{1}{cos\varphi_{PTO}} - 1}\right.$$
$$\left. - E^2(\frac{1}{cos\varphi_{PTO}} + 1)\right] + P_{peak}(R_{wec}^2 + X_{wec}^2) = 0 \tag{4.8}$$

For the second order equation to have at least one positive solution, there should be at least one variation in the signs of the coefficients. Under reasonable working conditions, the quadratic coefficient and the constant term are always positive. Thus, it is essential for the linear coefficient to be negative.

$$2P_{peak}R_{wec} + 2P_{peak}X_{wec}\sqrt{\frac{1}{cos\varphi_{PTO}} - 1} - E^2(\frac{1}{cos\varphi_{PTO}} + 1) +$$
$$P_{peak}(R_{wec}^2 + X_{wec}^2) < 0 \tag{4.9}$$

By analytical analysis of equation (4.9), different values of $cos\varphi_{PTO}$ are obtained depending on the buoy parameters and the incoming incident wave [84]. As the peak power is

already known, a higher value of $cos\varphi_{PTO}$ produces a higher average power from equation (4.7). Thus to maximize the average extracted power, the highest value of power factor, $cos\varphi_{PTO}$ must be chosen. The determinant of the second order equation (4.9) at the optimum value of $cos\varphi_{PTO}$ must be non-zero [84].

After determining the value of $cos\varphi_{PTO}$, the value of R_{PTO} is calculated from equation (4.8). The value of X_{PTO} is calculated from equation (4.6). Interestingly there were instances where the proposed method mathematically did not provide the optimal control parameters. In contrast, the simulations in [84] show that the proposed method did not fail for reasonable ranges of the incoming wave amplitudes and frequencies.

In cases where the incoming waves have small amplitude and high frequency, optimum control is chosen to fully exploit the lower energy content of the waves. In the case of high waves, pure damping is chosen so as not to exceed the power limit. When the peak power limit is in between the peak power produced by passive loading and optimum control, the intermediate reactive control can be used. Thus the intermediate reactive control maximizes the power output without exceeding the power limit of the electric machines and the power electronics. In this master thesis, the application of intermediate reactive control is not investigated.

Although the mathematical formulation was derived for sinusoidal conditions, the trends highlighted can be extended to irregular waves. However, the identification of proper control parameters should then be derived by time domain simulations.

Modelling and Control of Permanent Magnet Synchronous Generator

Chapter 5 looks at the details of the modelling and control of permanent magnet synchronous generators (PMSGs). It looks into the Clarke and Park transformation and how PMSGs are modelled in dq frame of reference. The electro-mechanical design of the PMSG is addressed. Afterwards, the decoupling of dq voltages in PMSGs, the voltage source converter (VSC) and the current controller to be connected to the PMSG are discussed. Field weakening application is explained at the end of chapter 5.

5.1 Permanent Magnet Synchronous Generator (PMSG)

Three different generators that can be used in WEC are compared. These are a linear permanent magnet (PM), induction generator and rotating PM.

Linear generators are connected directly to the buoy which means they do not need a mechanical transducer and a gear step-up. Linear PM generators are one example of linear generators in use. A tubular axial flux generator is often preferred within Linear PM generators because of its relative maturity. The disadvantage of linear PM generators is the magnetic discontinuity in stator and rotor which requires higher back iron cross-sections. Furthermore, due to the linear movement of the permanent magnets, some magnetic materials are inactive when they are outside stator [85]. The elimination of mechanical conversion to rotating movement is the main advantage of directly connected linear generators. The absence of gears eliminates the associated gear efficiencies. However, the requirement of precise bearings and high mechanical stability is a disadvantage. They have a limited bending moment so as to maintain the thin air gap of the generator. Linear generators experience high forces and low speeds due to the size of the buoy and the nature of the system in parts of wave operating cycle [85]. Gears change the linear motion of the buoy to rotational motion. While gears introduce an extra component, cost and power loss, they handle "end-stop" and other survivability related overload issues. The gears also open the possibility of utilizing well established electric generators, for example, robust induction generator [85].

Induction generators are simple and rugged in construction. They are robust and they can run in any environmental condition. Induction generators are cheaper and they are

maintenance free due to a lack of commutators, slip rings and brushes [86]. They can also operate in polluted and explosive environments as the lack of brushes avoid sparks. The disadvantage of induction generators is that they have poor starting torque and the speed control of induction generators is difficult [86].

In low speed, high pole PM rotating generators have constant speed irrespective of the load. They are directly connected to a step-up gear. Nonetheless, the weight is very high due to high torque at the low speed [85]. Table 5.1 compares the three types of generators briefly described above.

Table 5.1: Summary of three different kinds of generators. The +, 0 and - in the table represents favourable, neutral and less advantageous [85]

Type of generators	Weight	Efficiency	Robustness	Converter size	Cost
Induction	+	0.90	+	0	+
Linear PM	-	0.93	-	0	-
Rotating PM	-	0.95	0	+	0

In this master thesis, a rotating PMSG is preferred to be utilized. PMSGs have magnets mounted attached to the surface of the rotor or within the rotor itself. The magnets of the generator produce constant motor flux. PMSG is a cross between a brushless DC motor and an induction motor. It has a permanent magnet rotor like a brushless DC and a stator winding that produces a sinusoidal flux density in the air gap that resembles an induction generator. When PMSGs have digitally controlled converters, they can produce torque at zero speed. PMSG is well suited for high efficiency and high-performance motor drives. High-performance control is characterized by fast acceleration and deceleration, full torque control at zero speed and smooth rotation over the entire speed range of the motor [87]. High-performance motor control is performed by vector control technique also known as field-oriented control (FOC). The algorithm of vector control is to decompose the stator current in-terms of a torque generating part and a magnetic field generating part. Both components can be controlled separately.
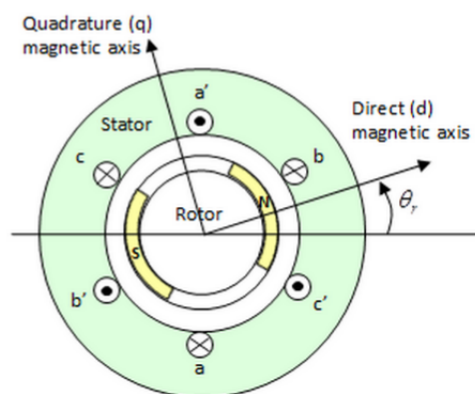

Figure 5.1: Motor construction of a permanent magnet synchronous generator (PMSG) with a single pole-pair on the rotor [88]

PMSGs offer many advantages over other types of generators. PMSGs are the most efficient electric machine. This is due to the presence of movable magnetic sources within
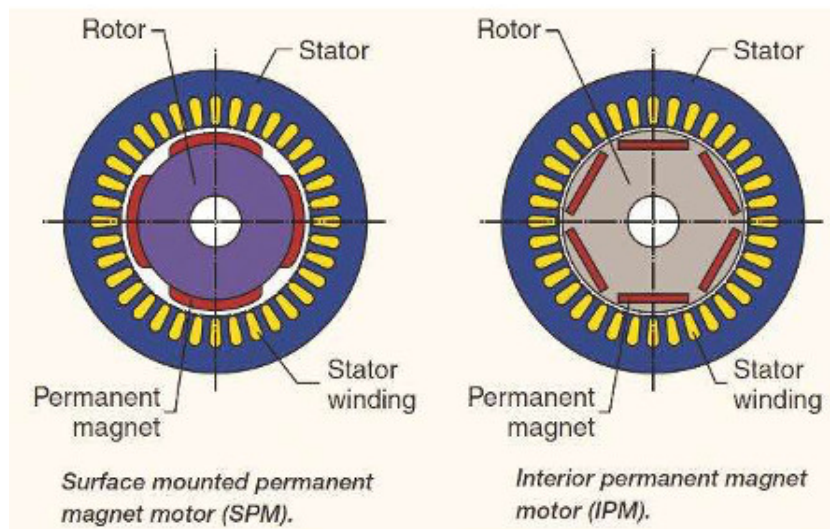
Figure 5.2: Diagram of a surface mounted and interior PM synchronous motor [89]

PMSGs. This eliminates copper loss of the exciter and makes the rotor easy to cool. It also minimizes the mechanical friction losses as PMSGs do not have slip rings or commutators and brushes [90]. These advantages help PMSGs to be built small, light and rugged structure. PMSGs need less maintenance and have higher reliability compared to most generators. However, they have more maintenance and less reliability compared to Induction generators due to the lack of commutators, slip rings and brushes. The winding insulation, bearing and magnetic life length of PMSG are also very long lasting [90]. The disadvantages of PMSGs are the high cost of permanent magnets and their commercial availability.

PMSGs can be divided into surface mounted permanent magnet synchronous generatorsss (SPMSG) and interior permanent synchronous generator (IPMSG), shown in Figure 5.2. Surface mounted PMSGs are not suited for high-speed application. Surface mounted PMSGs provide a uniform air gap as the permeability of the magnet and the air gap is almost the same. As a result, there is no reluctance torque. The dynamic performance of these generators is superior and it is suited for high-performance machine drives. IPMSGs have robustness and are applicable for high-speed applications. Reluctance torque is present due to the presence of saliency [89]. A round rotor surface mounted permanent magnet synchronous generator is used in this master thesis. The construction of a single pole-pair PMSG is shown in Figure 5.1.

The round rotor surface mounted permanent magnet synchronous generator (PMSG) is directly connected to the buoy without an intermediate hydraulic system as shown in Figure 1.5. This is referred to as a direct generation. This offers a high flexibility of speed and force control of the buoy movement and avoids comparatively low efficiencies. This results in almost total control of the force, speed and position of the buoy by the relevant choice of control parameters. This is highly crucial as the power loss in the primary

capture system is currently the dominating loss [85]. Conversions that take place in mechanical gear, converter, generator, grid and transmission have all over 90% efficiency. Previously, the direct drive was normally avoided to eliminate overrating of generators with respect to the average power [85].

5.2 Reference Frames of PMSG

In a symmetrical balanced three-phase system, the current and voltage of a generator can be described as three signals with the same frequency and amplitude but with a phase shift of one-third of a cycle. Thus, the alternating current could be written as:

$$
\begin{align}
i_a\,(t) &= I\cos(w_e t + \phi) = I\angle\phi \tag{5.1a}\\
i_b\,(t) &= I\cos(w_e t + \phi - 120) = I\angle(\phi - 120) \tag{5.1b}\\
i_c\,(t) &= I\cos(w_e t + \phi + 120) = I\angle(\phi + 120) \tag{5.1c}
\end{align}
$$

where i_a, i_b and i_c are the three-phase currents, I is the amplitude, w_e is the frequency of the electrical system and ϕ is the initial angle.
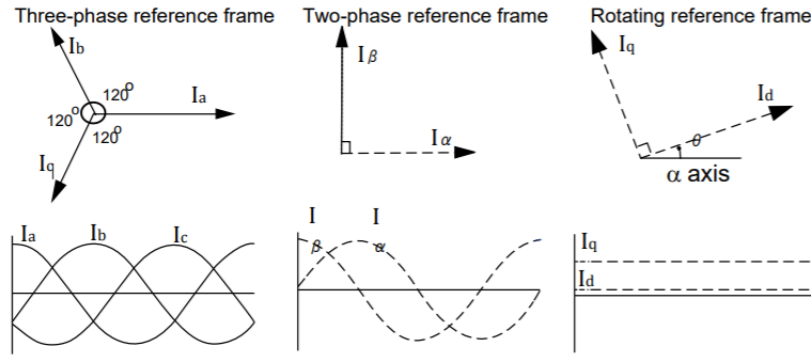
Figure 5.3: Three types of reference frames [91]

The three-phase reference frame is shown on the left side of Figure 5.3. The abc three-phase system can be transformed into "alpha-beta-gamma" ($\alpha\beta\gamma$) or dq0 frame. They are also known as Clarke and Park transformations. The main advantage of transformation is the orthogonality and reduced cross-coupling. The same three-phase signals would be represented by two signals and the values of the two signals are constant values. In the case of $\alpha\beta\gamma$, the two new signals are α and β and they are perpendicular to each other while γ is the zero-axis. In the case of dq0, the two new signals are d and q and they are perpendicular to each other. $\alpha\beta\gamma$ is an orthogonal stationary reference frame while dq0 is an orthogonal rotating reference frame.

5.2.1 Clarke Transformation

Clarke transformation ($\alpha\ \beta\ \gamma$) transforms a three-phase system into a two-phase orthogonal stationary system. The transformation matrix is:

$$T_{\alpha\beta\gamma} = \frac{2}{3} \begin{bmatrix} 1 & \frac{-1}{2} & \frac{-1}{2} \\ 0 & \frac{\sqrt{3}}{2} & \frac{-\sqrt{3}}{2} \\ \frac{1}{2} & \frac{1}{2} & \frac{1}{2} \end{bmatrix} \tag{5.2}$$

In a symmetrical balanced three-phase system the sum of currents or voltages in abc is zero. The value of signal γ is the sum of signal a, b and c multiplied by $1/3$ and therefore it has zero value. Thus, the transformation of equation (5.2) can be simplified to:

$$\begin{bmatrix} sig_\alpha \\ sig_\beta \end{bmatrix} = \frac{2}{3} \begin{bmatrix} 1 & \frac{-1}{2} & \frac{-1}{2} \\ 0 & \frac{\sqrt{3}}{2} & \frac{-\sqrt{3}}{2} \end{bmatrix} \begin{bmatrix} sig_a \\ sig_b \\ sig_c \end{bmatrix} \tag{5.3}$$

where sig stands for a signal.

It results in a signal having only two control variables and this reduces the number of controllers required and the computational power demand of micro-controllers or digital signal processors [92].
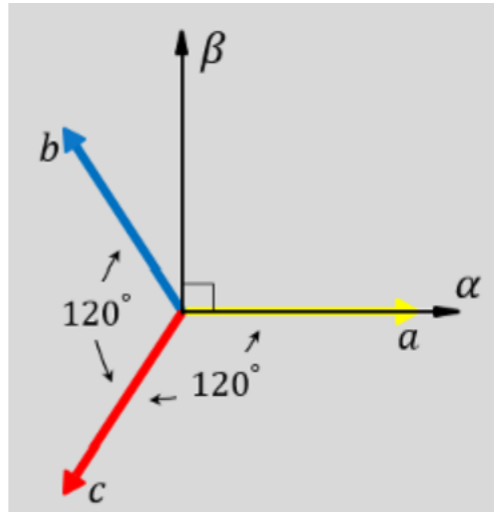
Figure 5.4: The direction of the magnetic axes of the stator windings in the abc reference frame and the stationary $\alpha\beta\gamma$ reference frame [93]

5.2.2 Park (dq0) Transformation

Park transformation transforms the stationary system to rotating orthogonal system. The dq0 transformation rotates the $\alpha\beta\gamma$ frame with an electrical angle of the motor, $\theta(t)$. The dq0 signals can be treated as stationary values as shown in Figure 5.3. The transformation matrix from $\alpha\beta\gamma$ to dq0 is:

$$T_{dq0} = \begin{bmatrix} cos\,\theta & sin\,\theta & 0 \\ -sin\,\theta & cos\,\theta & 0 \\ 0 & 0 & 1 \end{bmatrix} \tag{5.4}$$

In a symmetrical balanced three-phase system, the value of γ signal is zero and the transformation of equation (5.5) can be simplified to:

$$\begin{bmatrix} sig_d \\ sig_q \end{bmatrix} = \begin{bmatrix} cos\,\theta & sin\,\theta \\ -sin\,\theta & cos\,\theta \end{bmatrix} \begin{bmatrix} sig_\alpha \\ sig_\beta \end{bmatrix} \tag{5.5}$$

It is also possible to transform abc-reference frame directly to dq0-reference frame with Park transformation as shown in equation (5.6) [94].

$$\begin{bmatrix} sig_d \\ sig_q \\ sig_0 \end{bmatrix} = \frac{2}{3} \begin{bmatrix} cos\,\theta & cos\,(\theta - 120) & cos\,(\theta + 120) \\ -sin\,\theta & -sin\,(\theta - 120) & -sin\,(\theta + 120) \\ \frac{1}{2} & \frac{1}{2} & \frac{1}{2} \end{bmatrix} \begin{bmatrix} sig_a \\ sig_b \\ sig_c \end{bmatrix} \tag{5.6}$$

For a symmetrical balanced system, the value of the zero component is zero. The a-axis of the three-phase could be aligned either to d- or q-axis of the rotating frame of reference at the time, t=0. Figure 5.5 shows the a-axis aligned to q-axis.
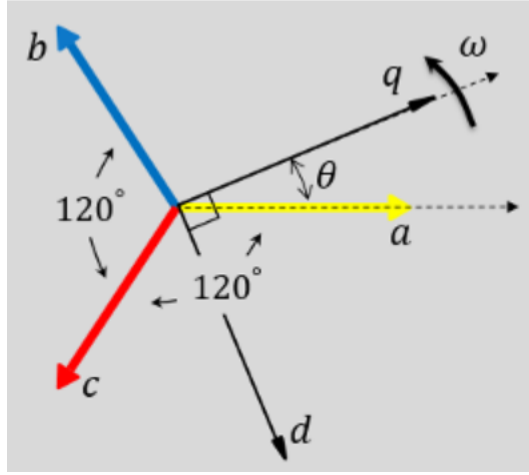
Figure 5.5: The a-axis and the q-axis are initially aligned [95]

Conventional PI controllers applied to three-phase stationary frame suffer from steady-state amplitude and phase error. Therefore they struggle to follow reference values in ac current regulations [96]. PI controllers acting on dq0 frame of reference can attain zero steady-state error since they act on dc signals. The DC values simplify the work of the controller in the system. They have only two signals and therefore only two PI controllers are required. Both the $\alpha\beta\gamma$ and the dq0 frame of references are shown in Figure 5.3.

5.3 Modelling of PMSG

In PMSG, the rotor mechanical angle can be defined as the angle between the a-phase magnetic axis and the rotor d- or q-axis. In the simulation part of this master thesis, the rotor mechanical angle is defined as the angle between the a-phase magnetic axis and q-axis. The voltages across the stator windings are defined by:

$$\begin{bmatrix} v_a \\ v_b \\ v_c \end{bmatrix} = \begin{bmatrix} R_s & 0 & 0 \\ 0 & R_s & 0 \\ 0 & 0 & R_s \end{bmatrix} \begin{bmatrix} i_a \\ i_b \\ i_c \end{bmatrix} + \begin{bmatrix} \frac{d\Psi_a}{dt} \\ \frac{d\Psi_b}{dt} \\ \frac{d\Psi_c}{dt} \end{bmatrix} \tag{5.7}$$

where:

- v_a, v_b and v_c are the individual voltages across the stator windings.

- R_s is the equivalent resistance of each stator winding.

- i_a, i_b and i_c are the currents flowing into the stator windings.

- $\frac{d\Psi_a}{dt}$, $\frac{d\Psi_b}{dt}$ and $\frac{d\Psi_c}{dt}$ are the rates of change of magnitude flux in each stator winding.

The stator voltages and currents are transformed into dq0 frame by applying Park's transformation on the stator winding voltages and currents. The resulting electromagnetic torque of the generator is expressed in dq frame of reference. The resulting equations are [97]:

$$v_d = R_s i_d + \frac{d\Psi_d}{dt} - w_e \Psi_q \tag{5.8}$$

$$v_q = R_s i_q + \frac{d\Psi_q}{dt} + w_e \Psi_d \tag{5.9}$$

$$T_e = \frac{3}{2} p (\Psi_d i_q - \Psi_q i_d) \tag{5.10}$$

where

- R_s is the equivalent resistance of each stator windings.

- i_d is d-axis current

- i_q is q-axis current

- v_d is d-axis voltage

- v_q is q-axis voltage

- w_e is the rotor electrical rotational speed

- Ψ_d is direct axis flux linkage

- Ψ_q is quadrature axis flux linkage

- p is the number of pole-pairs

- T_e is the rotor torque

The direct and quadrature axis flux linkages are functions of d and q-axis currents.

$$\Psi_d = f(i_d, i_q) \tag{5.11a}$$
$$\Psi_q = f(i_d, i_q) \tag{5.11b}$$

In surface mounted PMSG there is no need to induce rotor currents from stator to rotor as the permanent magnet serves as a source of flux and it can be taken as infinite resistance. As there is no mutual inductance between stator and rotor, the value of cross-inductance is zero. The flux is produced by the field winding in the d-axis and the torque is produced

in the q-axis [89]. The q-axis leads the d-axis electrically by 90 degrees. As there is no flux in q-axis, the variable Ψ_m will be used to denote the d-axis component of magnetic flux. The value of L_d and L_q are assumed to be constant neglecting the saturation effects. The value of the d-axis component of magnetic flux is assumed to be constant. The values of d- and q-axis flux linkage are approximated by linearization.

$$\Psi_d \approx \Psi_{md} + L_d i_d \tag{5.12a}$$
$$\Psi_q \approx L_q i_q \tag{5.12b}$$

Inserting equations (5.12a) and (5.12b) in equations (5.8), (5.9) and (5.10), the resulting equations are:

$$v_d = R_s i_d + L_d \frac{di_d}{dt} - p w_m i_q L_q \tag{5.13}$$

$$v_q = R_s i_q + L_q \frac{di_q}{dt} + p w_m i_d L_d + p w_m \Psi_m \tag{5.14}$$

$$T_e = \frac{3}{2} p (\Psi_m + (L_d - L_q) i_d) i_q \tag{5.15}$$

$$w_e = p w_m \tag{5.16}$$

where L_d is d-axis inductance, L_q is q-axis inductance, R_s is the equivalent resistance of each stator windings, w_m is the rotor mechanical rotational speed, w_e is the rotor electrical rotational speed and Ψ_m is rotor flux linkage (the amplitude of flux induced).

The electromagnetic torque of equation (5.15) consists of torque due to the interaction of stator current and magnetic flux, and reluctance torque due to the saliency of the rotor.
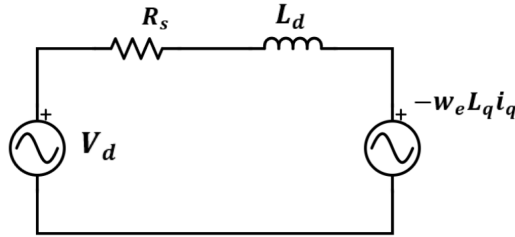

Figure 5.6: The D-axis electrical equivalent circuit for PMSG
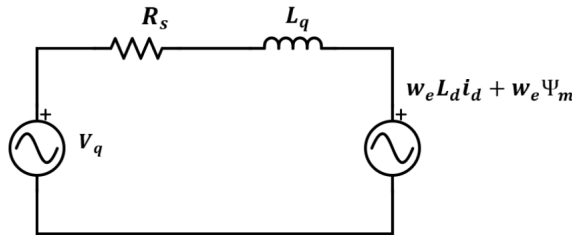
Figure 5.7: The Q-axis electrical equivalent circuit for PMSG

Figure 5.6 and 5.7 shows the electrical equivalent circuits for the generator in dq reference frame from equations (5.13) and (5.14). A block diagram of PMSG is shown in Figure 5.8 and a picture of the modelled PMSG in Simulink with sensors is shown in Figure 5.9.
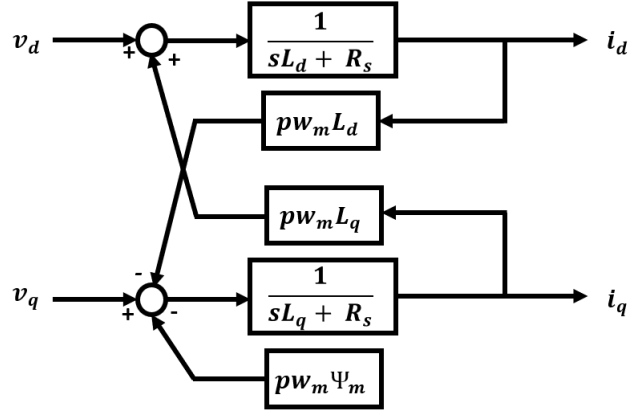
Figure 5.8: Block diagram of a Permanent Magnet Synchronous Generator (PMSG)
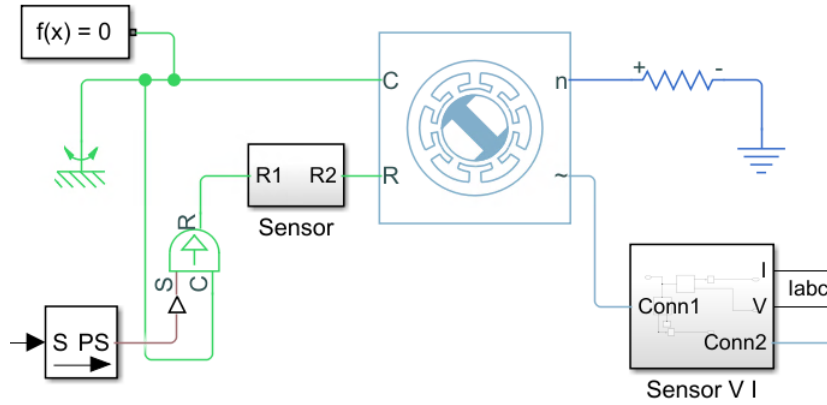
Figure 5.9: Simulink model of PMSG

The employed PMSG is a round rotor (non-saliency) and therefore, the d- and q-axis inductances are equal to each other due to uniform air-gap.

So equations (5.13), (5.14) and (5.15) could be written as:

$$v_d = R_s i_d + L\frac{di_d}{dt} - pw_m i_q L \tag{5.17}$$

$$v_q = R_s i_q + L\frac{di_q}{dt} + pw_m i_d L + pw_m \Psi_m \tag{5.18}$$

$$T_e = \frac{3}{2}p\Psi_m i_q \tag{5.19}$$

The parameter values of the modelled PMSG are presented in table 5.2 and they are based on a master thesis written by Vasile-Simion Sularea in Aalborg University [98].

Table 5.2: Rated parameters of the modelled PMSGs

Rated mechanical power	P_{rated}	250 [kW]
Rated stator phase voltage	U_s	270 [V]
Rated stator current	I_s	330 [A]
Number of pole pairs	p	8
Rated rotor flux linkage	Ψ_m	5.82 [Wb]
Stator winding resistance	R_s	8.21 [mΩ]
Stator winding inductance	L_s	14 [mH]

5.3.1 Electro-Mechanical design of the PMSG

A recirculating ball screw is coupled with the PMSG to convert linear to rotational motion as shown in Figure 5.10. The linear input motion causes the rotational motion of the nut. The ball nut is directly connected to the rotor of the PMSG which generates electrical power from the linear mechanical motion. One main advantage of ball screw system is the conversion of low-speed high force input into a high speed but low force motion [78].
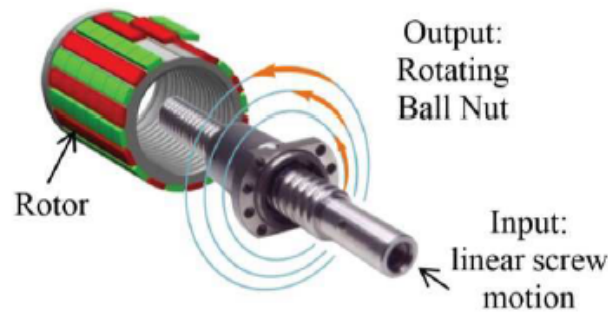

Figure 5.10: Electro-mechanical ball screw PTO [78]

The conversion of linear to rotational motion has poor friction losses hereby increasing the overall efficiency of the system. The shortened energy conversion chain reduces the number of components and this results in a lower risk of failure [78].

The distance between two adjacent screw threads is called screw pitch (p_{sc}) and it is one of the main parameters in the process. The length of the screw pitch is $0.10125\,m$. The screw pitch defines the relation between the linear input speed (v_{in}) and the nut rotational speed (w_m) [78].

$$w_m(t) = \frac{v_{in}(t)\,2\pi}{p_{sc}} \tag{5.20}$$

where p_{sc} is the screw pitch, $v_{in}(t)$ is the linear input speed and $w_m(t)$ is the nut rotational speed.

The high input force, F_{PTO}, is translated into rotational by the following equation [78]:

$$T_{ref} = \frac{F_{PTO}\,p_{sc}}{2\pi}\eta_{bs} \tag{5.21}$$

where F_{PTO} is the input force without friction loss, T_{ref} is the reference rotational torque (rotor torque) and η_{bs} is the ball screw efficiency.

The conversion of linear to rotational motion in Simulink is:
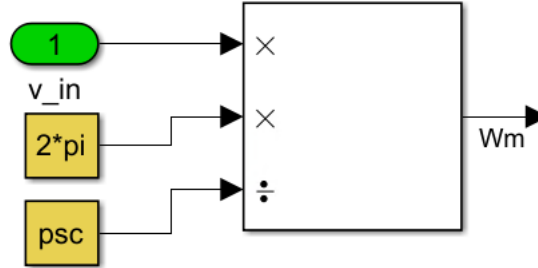
Figure 5.11: Conversion from linear to rotational motion in Simulink

The calculation of rotor torque from the input force as well as the calculation of the reference q-axis current from the rotor torque in Simulink are shown in Figure 5.12. The efficiency of the ball screw is missing in Figure 5.12. However, the mechanical friction losses are taken into consideration by translational PTO actuation force blocks inside the Wec-Sim model as described in section 4.2. Therefore the reference torque is calculated as:

$$T_{ref} = \frac{F_{PTO}\, p_{sc}}{2\pi} \tag{5.22}$$

The reference q-axis current that generates power in Figure 5.12 is calculated the same as equation (5.19).
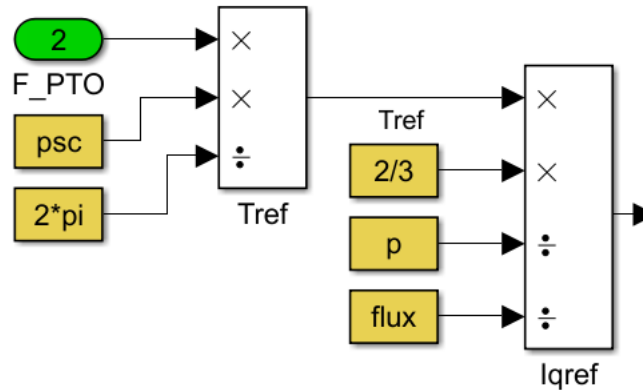
Figure 5.12: Calculation of q-axis reference current from WEC input force

5.3.2 Power Losses

The copper resistance of the stator winding generates power loss. The power losses in the copper resistance of the PMSG is [99]:

$$P_{cu} = \frac{3}{2}(R_s i_q^2 + R_s i_d^2) \tag{5.23}$$

where R_{cu} is the stator resistance, i_d is the d-axis current and i_q is the q-axis current.

Operating with i_d current zero minimizes the power losses. The PMSG has a lower stator copper loss when operating in constant torque region. Assuming i_d equal to zero:

$$P_{cu} = \frac{3}{2} R_s i_q^2 \tag{5.24}$$

By substituting the variable torque in equation (5.22) from equation (5.19) or by analyzing Figure 5.12, i_q can be expressed as:

$$i_q = \frac{p_{sc}}{3\pi p \Psi_m} F_{PTO} \tag{5.25}$$

Substituting the value of i_q:

$$P_{cu} = \frac{R_s p_{sc}^2}{6\pi^2 p^2 \Psi_m^2} F_{PTO}^2 \tag{5.26}$$

The above equation shows how the stator copper losses are affected by the input force without friction loss. Substituting the values of the parameters:

$$P_{cu} = 5.245 * 10^{-9} F_{PTO}^2 \tag{5.27}$$

The coefficient of proportionality between the stator copper losses and the PTO force is small and the stator copper losses are expected to be low.

5.4 Voltage Source Converter (VSC)

An Average-Value Voltage Source Converter block is used to convert electrical energy from AC to DC. The Voltage Source Converter (VSC) is connected in series with the generator and therefore it should have a high enough rating for the maximum current and maximum voltage to pass through. The rating of the VSC is chosen to be equal to the rating of the generator $250\,kW$. The rated voltage and rated current of the VSC are $500\,V$ and $500\,A$ respectively. The VSC is able to withstand the maximum current of the generator that is a little higher than $400\,A$, shown in the simulation part of chapter 6. The efficiency of the VSC is 95%. The input of VSC is a physical signal input port and it is a normalized modulation wave directly connected to the output of the current controller. The output of the VSC is connected to a DC link. The voltage of the DC link is $1000\,V$.

The VSC controls the power produced by the buoy movement. It converts the input of the VSC which has a variable current, variable voltage and variable frequency to a constant DC voltage. Thus, the use of VSC increases the absorption of wave power while maintaining power and voltage conditioning. The converter is bidirectional as there are instances where power flows in reverse direction. The reverse flow of power is in-case of optimum control strategy discussed in section 4.1.
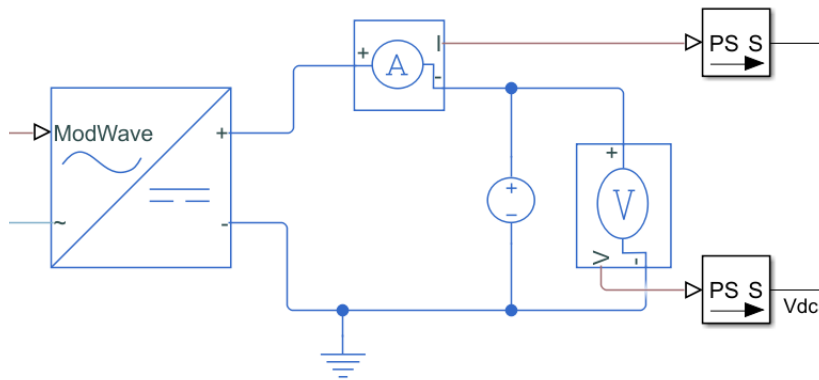
Figure 5.13: Average-Value Voltage Source Converter and DC link

5.5   Current Controller

The current controller shown in Figure 5.14 controls the stator currents to control torque which controls the force of the Power Take-Off as shown in Figure 5.12. This results in phase and amplitude control of the WEC [83]. The dynamic resistance and mechanical reactance of the WEC perceived by the coming waves are changed or controlled. Some kind of destructive interference is performed between the waves and the WEC. For the desired interference to occur the current of the generator is made to track the desired current or the reference current calculated. The current controller is applied to make sure the current of the PMSG follows the reference current.
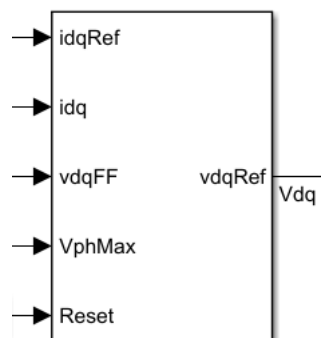
Figure 5.14: PMSG Current Controller

The techniques for following the desired current trajectory is based on vector/field-oriented control (FOC). The vector control decomposes the stator current and both components are controlled separately. To keep the current at the desired value, FOC usually applies decoupling terms, proportional-integral (PI) controllers, and pulse-width modulation (PWM). FOC is an industry standard in control of PMSGs due to modularity, flexibility, low computational burden and robustness with respect to parameter variation. The design stage of current controllers does not normally take voltage and current constraint into consideration. As a result, anti-windup, dynamic over-modulation as well as decreasing the gain of the controller are applied. Over-modulation increases losses during transient operation.

A decrease of gain of a controller results in performance deterioration [97]. PWM is not discussed as the VSC used is an Average-Value VSC as mentioned in section 5.4.

5.5.1 Decoupling of d-axis and q-axis voltages

The dq voltage values are coupled as shown in equation (5.17) and (5.18). This results in the change of one output affecting the output of the other and this, in turn, affects the output of the previous variable. The decentralized control becomes challenging. The Multiple Input Multiple Output (MIMO) is changed to Single Input Single Output (SISO) by decoupling v_d and v_q. The decoupling is employed by feed forward of v_d and v_q. The new reference voltages are defined as $v_d' = v_d + w_e i_q L$ and $v_q' = v_q - w_e i_d L - w_e \Psi_m$. Thus, equation (5.17) and equation (5.18) would be:

$$v_d' = R_s i_d + L_s \frac{di_d}{dt} \tag{5.28a}$$

$$v_q' = R_s i_q + L_s \frac{di_q}{dt} \tag{5.28b}$$

Thus v_d' and v_q' are independent and both are first order equations.
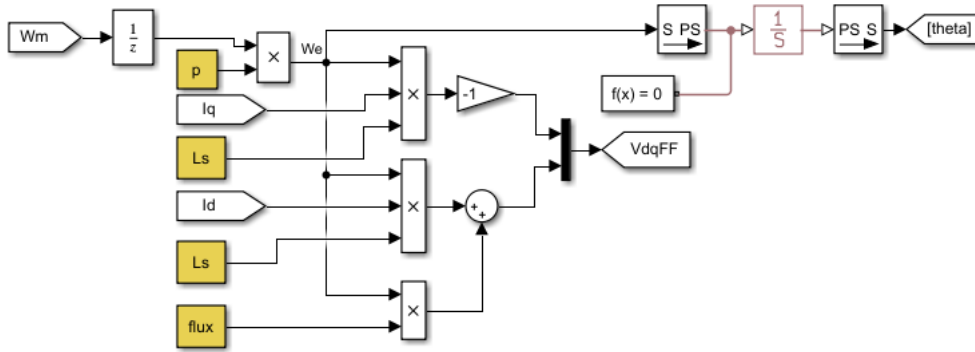
Figure 5.15: Feed forward voltages of v_d and v_q

The equations for feed forward voltages v_d and v_q used in the Simulink are shown in Figure 5.15.

5.5.2 PI Controllers

A PI-controller calculates the error value as the difference between the desired value and the measured value. An accurate and responsive correction is applied to the control function. There are two tuning values and they are the controller gain K_p and the integral time constant T_i. An analogue PI-controller is applied for the i_d and i_q currents to follow the i_{dref} and i_{qref} reference currents. The internal workings of the PI controller is shown in Figure 5.16. The origins of the inputs of the PI controller are shown clearly in Figure 5.17 where e is the error signal which is the difference between reference and PMSG generated current, du is control signal saturation which is the difference between the input and output of d-q voltage limiter, and $Reset$ is integral gain reset. There are also additional functions of PI-controller [100]. These are:

Figure 5.16: The internal structure of a PI controller

- Limitation of output: The value of the output of the controller is set to be between defined values of upper and lower limit. The VSC has a 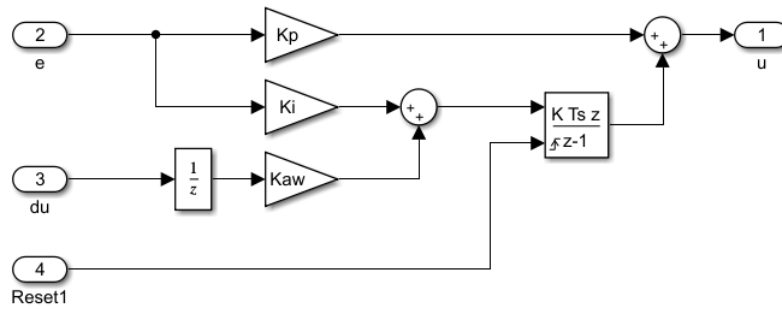limit on the voltage reference it can generate. This limiting value depends on the voltage of the DC-link. The current controller takes the maximum phase voltage as an input and it is half of the value of the DC-link, $500\,V$.

- Initial Values: An integrator's initial value can be defined by the user. The initial values of integrators are set to zero if the simulation starts from zero. Otherwise, the integrator should follow up the output i.e. the initial value of integrator should be the initial output value.

- Feed Forward: Most current controllers have a feed forward [100]. The feed forward of v_d and v_q in the current controller are already defined in section (5.5.1) and they are $v_d' = v_d + w_e i_q L$ and $v_q' = v_q - w_e i_d L - w_e \Psi_m$.

- Anti-windup: This is applied when the output reaches a saturation. As the output can not increase further, the integration must be stopped until the response falls back into an acceptable range. Negative input is sent to the PI-controller until it moves out of the saturation. Anti-windup is shown in Figure 5.17 where the difference of the input and output of the d-q voltages limiter is sent back as an input to the PI controllers. The difference between input and output of d-q voltage limiter is zero as long as the value of the d-q input voltages are not higher than the saturation value. The difference between input and output is non-zero only when any of the input values are higher than the saturation value. The value of anti-windup sent to the PI controller is always negative as it is the input voltage minus the output voltage. The output voltage is limited by the d-q voltage limiter and therefore it is never higher than the input value. In the PI controller, the value of anti-windup is multiplied by the corresponding axis anti-windup gain and then added to the integral part of the PI controller. The value of d-axis and q-axis anti-windup gain used in the simulation is 200 as shown in Table 5.3.

To choose the parameters of a controller, there are different methods that can be applied [100]:

- bode-plot: It is possible to get the transfer function of the system from the bode-plot. From the transfer function, the values of controller parameters can be fetched. The classic criterion is that the gain margin must be at least 6 dB and a phase margin must be at least 45 degrees.

- Pole location can also be used to determine the parameters of the PI controller.

- Use of Modulus optimum and Symmetric optimum [101].

As the system parameters are known, PI parameters can be calculated by using pole location, or Modulus or Symmetrical optimum.
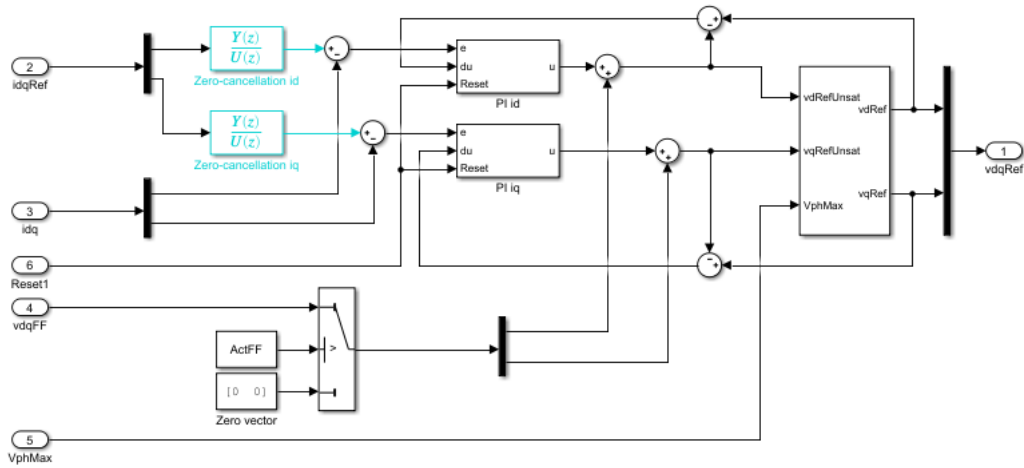
Figure 5.17: The internal structure of a current controller

In power electronics, an internal reduction of block diagrams often end up with one large dominant time constant and other minor time constants [100]. The dominating time constant in PMSG is the stator current time constant. The corresponding transfer function of equation (5.28a) and equation (5.28b) can be written as:

$$\frac{i(s)}{v(s)} = \frac{\frac{1}{R_s}}{1 + \frac{L}{R_s}s} \tag{5.29}$$

The current controllers are applied to the dq reference frame. The system is decoupled into d and q, and therefore two PI controllers are needed. Due to the speed of the WEC, the influence of PWM and converter time constants are ignored. The transfer function of the PWM and the converter are assumed to be unity. Figure 5.18 shows a closed loop consisting of PI controller, PWM, converter and PMSG. To tune the PI controllers Modulus Optimum is chosen.

Figure 5.18: A block diagram of a current controller. The PWM and the converter block are represented by unity gain [102].

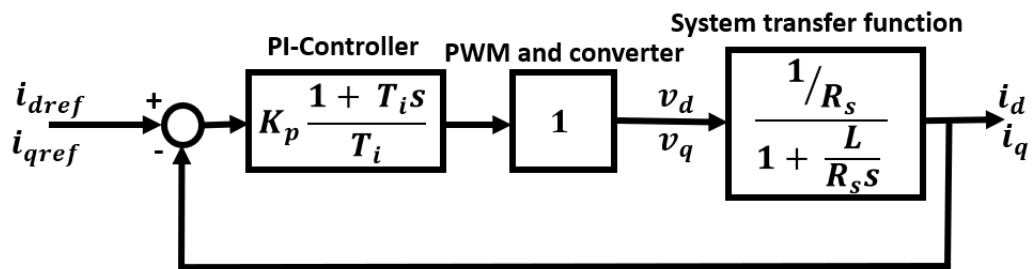One of the oldest controller design methods is Optimum Modulus. It is often used for low order controlled plants without time delay. The modulus optimum control transfer function is achieved by cancelling the largest time constant of the system transfer function and holding the closed gain to be higher than unity for all frequencies [101]. The advantage of Modulus Optimum is the simplicity and fast response it presents.

The final open loop transfer function from Figure 5.18 can be written as:

$$h_o(s) = K_p \frac{1 + T_i s}{T_i s} \frac{\frac{1}{R_s}}{1 + \frac{L}{R_s} s} \tag{5.30}$$

By Modulus Optimum the PI-controllers time constant T_i is selected to be equal to $\frac{L}{R_s}$. Thus, the resulting equation is:

$$h_o(s) = K_p \frac{\frac{1}{R_s}}{\frac{L}{R_s} s} = K_p \frac{1}{Ls} \tag{5.31}$$

The closed loop transfer function is:

$$M(s) = \frac{h_o(s)}{1 + h_o(s)} = \frac{K_p}{K_p + Ls} = \frac{K_p}{K_p + Ljw} \tag{5.32}$$

To have unity gain the value of K_p must be much higher than the value of L.

The proportional and integral gain values of the d-axis and q-axis PI controllers are given in table 5.3.

Table 5.3: Parameters of current controller

D-axis current proportional gain	Kp	16
D-axis current integral gain	Ki	150
D-axis current anti-windup gain	Kaw	200
Q-axis current proportional gain	Kp	16
Q-axis current integral gain	Ki	150
Q-axis current anti-windup gain	Kaw	200

Figure 5.19 shows the current controller in Simulink with all inputs and outputs included. The current controller has inputs of the generator's i_d and i_q currents, feed forward voltage VdqFF, maximum phase voltage Vphmax, and calculated reference currents i_d and i_q. The generator's i_d and i_q currents are obtained by Park transformation from the abc current output of the generator and the angle theta. The calculation for angle theta is shown in Figure 5.15. The sign of i_d and i_q current is reversed just before it is sent to the current controller. This is in order for the current controller to function well with the positive gain values already presented in table 5.3. The corresponding input of i_d and i_q reference currents also shift sign. They shift sign before the value of VdqFF is calculated as the feed forward voltage is also an input of the current controller and it needs to be calculated with actual input currents of the current controllers. The calculation for VdqFF is shown in Figure 5.15. Vphmax is the maximum phase angle and its value is $500\,V$. The calculation of reference currents i_d and i_q is presented in the next section 5.6. The output of the current controller, v_d and v_q are transformed to abc voltage by inverse Park transformation, normalized by Vphmax and sent to VSC.
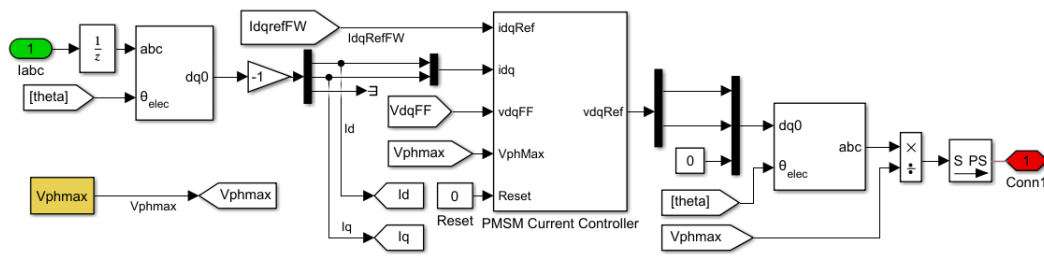
Figure 5.19: A Simulink model of a current controller with all the inputs and outputs included

5.6 Field Weakening

For an ideal brushless DC generator, speed and current are proportional to voltage and torque. This characteristic is imitated by modern AC generators. The operation region of the PMSG is divided into two areas. These are constant torque control region and the field weakening control region. In the constant torque control region, the torque is constant while the active power generated differs with the speed of the generator. In the field weakening control region, the active power is constant while the torque decreases with increase in speed.

PMSG produce a back electromotive force (EMF) that rises proportionally to the speed of the generator. The back EMF voltage is created by relative motion between the stator windings and the rotor's magnetic field. The value of back EMF is proportional to the rate of change of the magnetic field, its intensity and the number of turns. The opposite polarity of the back EMF reduces the actual voltage in the armature turns and decreases the current flowing through the generator [103]. When the speed of the generator continues to increase the voltage eventually reaches the maximum value. The speed of the generator at maximum voltage is referred to as the base speed. If the speed of PMSG overcomes the base speed, there is no current flowing between the converter and the PMSG, and the input torque does not produce current. In cases when the PMSG is running as a motor, the current does not flow from the converter to the stator coils as there is no torque generated. Further increase of speed can produce current or torque which is opposite to the direction of rotation depending on whether the PMSG is acting as a generator or motor. To run the PMSG over the base speed, the internal EMF must be reduced and it is achieved by reducing the magnetic flux between the rotor permanent magnets and stator coils. This results in reduced maximum torque and the converter avoids entering into saturation. This principle of weakening the magnetic field by applying an opposing magnetic field on the stator coils in phase with the rotor field is known as field weakening [104].

For the PMSG to operate in an extended range of speed, field weakening is adopted. The voltage limit is defined by the DC-link voltage and the current limit is defined by the PMSG and the IGBTs in the converter [104]. In DC, induction and ordinary synchronous machines field weakening is achieved by reducing the field current. In PMSG, the field weakening is accomplished by exerting an opposing magnetic field on the stator coils which is in-phase with the magnetic field from the rotor. A negative stator current in the direct axis (d-axis) creates the opposing magnetic field and reduces the internal EMF generated by the PMSG [104].

The maximum current and maximum voltage are limited by the following formulas.

$$i_d^2 + i_q^2 \leq I_{rated}^2 \tag{5.33a}$$
$$v_d^2 + v_q^2 \leq V_{limit}^2 \tag{5.33b}$$

The rated current, $330\,A$, is the maximum current the PMSG can operate with. For a limited amount of time, the machine can withstand a current much higher than the rated current. It is difficult to specify the maximum value of the current the generator can withstand. It depends on the machine's thermal capacitance and thermal conditions [97]. As a result of this, the current limit is treated as a soft constraint in the simulation part.

V_{limit} is the maximum voltage available from the converter. Its value is given by $V_{limit} = \frac{V_{dc-link}}{2}$. The value of V_{limit} can be increased by inserting a third harmonics. The third harmonics is measured and added to the output of each phase of a three-phase converter. The insertion of third harmonics increases the phase voltage by 15%. As third harmonics in three phase are cophasal, they do not appear in the line to line waveforms but they decrease the peak voltage of phase waveform [105]. The 15% increased value of $V_{dc-link}$ results in $V_{limit} = \frac{V_{dc-link}}{\sqrt{3}}$. In this thesis, an average-value VSC is employed and therefore, insertion of third harmonics was not implemented to increase the maximum allowed voltage. The maximum voltage is:

$$V_{limit} = \frac{V_{dc-link}}{2} \tag{5.34}$$

The value of dc-link voltage is $1000\,V$ and therefore the maximum input phase voltage of the converter is $500\,V$. The voltage limit at the PMSGs is set to $475\,V$. The output voltage of the PMSG has a varying amplitude and frequency due to input variations. This could cause saturation of PI controllers and to avoid that the voltage limit of PMSGs is set to $475\,V$.

The equations for v_d and v_q are given by equation (5.17) and equation (5.18). In steady state they are given as:

$$v_d = R_s i_d - w_e i_q L \tag{5.35a}$$
$$v_q = R_s i_q + w_e i_d L + w_e \Psi_m \tag{5.35b}$$

Inserting equation (5.35a) and equation (5.35b) into equation (5.33b) and calculating the voltage limits:

$$(R_s i_d - w_e i_q L)^2 + (R_s i_q + w_e i_d L + w_e \Psi_m)^2 = V_{limit}^2 \tag{5.36}$$

Equation (5.36) can be rewritten as [Appendix A.3]:

$$\left(i_d + \frac{w_e^2 L \Psi_m}{R_s^2 + w_e^2 L^2}\right)^2 + \left(i_q + \frac{w_e R_s \Psi_m}{R_s^2 + w_e^2 L^2}\right)^2 = \frac{V_{limit}^2}{R_s^2 + w_e^2 L^2} \tag{5.37}$$

The voltage drop across phase resistance R_s can be ignored as PMSG are used in comparatively high speed range. Therefore, ignoring armature resistance, equation (5.37) can be written as:

$$\left(i_d + \frac{\Psi_m}{L}\right)^2 + i_q^2 = \left(\frac{V_{limit}}{w_e L}\right)^2 \tag{5.38}$$

Equation (5.38) denotes the trajectory of stator voltage equation. It describes a set of circles with a radius of $V_{limit}/(w_e L)$ and whose centre is at $(-\Psi_m/L, 0)$ as shown in Figure 5.20. Inserting the values of the parameters of the PMSG the radius of the circle is 33928.57 multiplied by $1/w_e$ and the centre of the circle is $(-415.71, 0)$. All the circles have a fixed centre but different radius depending on the speed. As the speed increase, the voltage circle shrinks and the area of the circle is reduced. The reachable current vector is reduced when the speed increases. When the speed is further increased, the reference current is located outside the voltage circle. In this case, a negative d-axis current is required. This means the machine must operate in field weakening to move the reference current vector back inside the voltage circle.
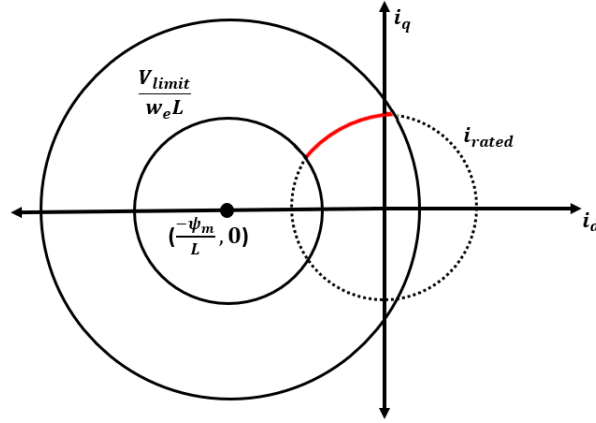

Figure 5.20: Diagram showing the voltage and current boundaries of operation. The red line denotes the optimal operation with maximum current and voltage

The following equation is achieved by expanding equation (5.36) and rearranging with descending order of i_d.

$$(R_s^2 + w_e^2 L^2)i_d^2 + (2w_e^2 L\Psi_m)i_d + w_e^2 i_q^2 L^2 + R_s^2 i_q^2 + w_e^2 \Psi_m^2 + 2R_s w_e \Psi_m i_q - V_{limit}^2 = 0 \quad (5.39)$$

Equation (5.39) is a second-order equation of the form $ax^2 + bx + c = 0$ and the solution is:

$$i_d = \frac{-b \pm \sqrt{b^2 - 4ac}}{2a} \quad (5.40)$$

where a is $R_s^2 + w_e^2 L^2$, b is $2w_e^2 L\Psi_m$ and c is $w_e^2 i_q^2 L^2 + R_s^2 i_q^2 + w_e^2 \Psi_m^2 + 2R_s w_e \Psi_m i_q - V_{limit}^2$.

Inserting the parameters of PMSG the values of a, b and c are $0.00821^2 + 0.014^2 w_e^2$, $0.163 w_e^2$ and $0.014^2 w_e^2 i_q^2 + 0.00821^2 i_q^2 + 5.82^2 w_e^2 + 0.0956 w_e i_q - 475^2$. In order to obtain a real value for i_d, $b^2 - 4ac$ must be greater than zero. Substituting the values of a, b and c in $b^2 - 4ac$:

$$(2w_e^2 L\Psi_m)^2 - 4(R_s^2 + w_e^2 L^2)(w_e^2 i_q^2 L^2 + R_s^2 i_q^2 + w_e^2 \Psi_m^2 + 2R_s w_e \Psi_m i_q - V_{limit}^2) \geq 0 \quad (5.41)$$

Ignoring the value of armature resistance and calculating for the value of i_q, the values of i_q that satisfy equation (5.41) are [Appendix A.4]:

$$-\frac{V_{limit}}{w_e L} \leq i_q \leq \frac{V_{limit}}{w_e L} \quad (5.42)$$

In field weakening, the maximum allowed i_q utilized in MATLAB simulation in Chapter 6 is 99% of the calculated limit value $V_{limit}/(w_e L)$. This practical restriction is to allow a margin for the variations of the PMSG characteristics due to temperature and stator core saturation [104]. Other reasons to lower the voltage limit are the minimum PWM pulse width and IGBT forward voltage drop.

$$-0.99\frac{V_{limit}}{w_e L} < i_q < 0.99\frac{V_{limit}}{w_e L} \tag{5.43}$$

Inserting the value of V_{limit}/L into equation (5.43).

$$-\frac{33589.28}{w_e} < i_q < \frac{33589.28}{w_e} \tag{5.44}$$

Figure 5.21 shows how the i_q current limit is implemented in Simulink. Figure 5.22 shows how the i_d and i_q reference currents are calculated. In the top left of Figure 5.22, the i_q current limitation is shown. In the lower left, the calculations for v_d and v_q are shown. The value of i_d in case of field-weakening is calculated by using equation (5.40). The switch at the top right sends the calculated negative current i_d whenever the value of $v_d^2 + v_q^2$ is higher than V_{limit}^2 i.e. in case of field weakening.
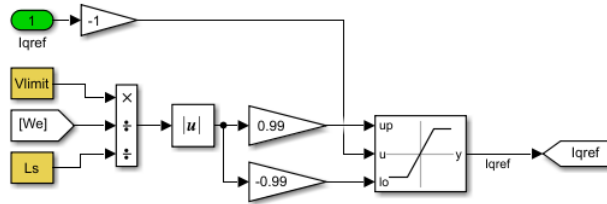

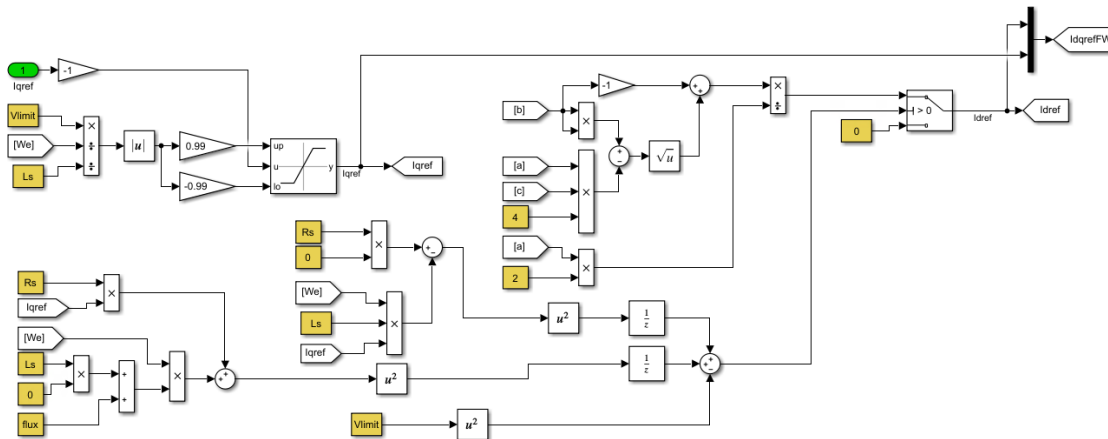**Figure 5.21:** A Simulink model of i_q reference current limit

Figure 5.22: A Simulink model of i_q current limit and field-weakening i_d current calculation

The base speed for rated i_q current could be calculated from equation (5.36). By expanding equation (5.36), it could be written in the form of a second-order polynomial. At base speed for rated i_q current, the value of i_q is equal to I_{rated} and the value of i_d is zero. Substituting i_q with I_{rated} and putting the value of i_d to zero, equation (5.36) can be expanded

and rewritten in the form of a second-order polynomial. The value of base speed at rated i_q is:

$$w_e = \frac{-2R_s I_{rated}\Psi_m \pm \sqrt{(2R_s I_{rated}\Psi_m)^2 - 4(\Psi_m^2 + L^2 I_{rated}^2)(R_s^2 I_{rated}^2 - V_{limit}^2)}}{2(\Psi_m^2 + L^2 I_{rated}^2)}$$

Two values of w_e can be calculated from equation (5.6). The negative sign before the square root is applied to calculate the base speed at rated speed when the PMSG is running as a generator while the positive sign is applied when the PMSG is running as a motor.

Figure 5.20 shows the voltage and current boundaries of operation. Above the base speed, the PMSG is in field weakening. To attain maximum available torque the PMSG is run along the red line shown in Figure 5.20. The red line is the intersection between the voltage limit at the defined speed and the current limit.

5.6.1 Limitation of active power

The value of active power produced from each PMSG can be described by:

$$P_e = T_e\, w_e \tag{5.45}$$

The expression for torque is given in equation (5.19) and substituting the expression for torque in equation (5.45):

$$P_e = \frac{3}{2}p\Psi_m i_q w_e \tag{5.46}$$

w_e is equal to p multiplied by w_m and from equation (5.42), the maximum i_q is $\frac{V_{limit}}{w_e L}$ due to field weakening. The maximum active power that can be generated by each PMSG is:

$$P_e = \frac{3}{2}\Psi_m w_e \frac{V_{limit}}{w_e L} = \frac{3}{2}\Psi_m \frac{V_{limit}}{L} \tag{5.47}$$

The values of Ψ_m and L are constants and therefore the maximum active power depends on the voltage limit. Inserting the values of V_{limit}, L and Ψ_m, the maximum active power that can be generated by each PMSG is $296.20\, kW$.

Chapter 6

Wave to Wire Modelling and Simulation

Chapter 6 covers a detailed description of simulations conducted with capping and uncapping of input mechanical power to PMSG in two different control strategies i.e. passive loading and optimum control. The optimal values of damping coefficient and the spring coefficient in each type of simulation and their corresponding maximum average electric output power are presented. The maximum average output power obtained in each type of simulation are compared to each other, and their corresponding ratio of peak to average electrical output power are discussed.

6.1   Simulation

In this part, the simulation of PA3 is performed. Two different control strategies of point absorber WEC are applied. These are passive loading and optimum control. The values of static and dynamic friction force are chosen to maximize the power generated by a wave of a significant height of $3.25\,m$ and a peak period of $12\,s$ [106]. The duration of the simulation is $600\,s$ and a time step of $0.5\,ms$ is applied. The DC-link voltage and the PMSG maximum voltage are $1\,kV$ and $475\,V$ respectively as mentioned in section 5.6. The parameter values used in the simulation are presented in table 6.1.

Table 6.1: Parameter values for simulation

Parameter	Value
Power capping value	$250\,kW$
Static friction force	$11.4684\,kN$
Dynamic friction force	$22.8093\,kN$
Time step	$0.5\,ms$
Duration of simulation	$600\,s$
DC-link voltage	$1\,kV$
PMSG voltage limit	$475\,V$

The two control strategies are applied with and without capping the input power of the generator. The power capping value of the input of the generator is the same as the rated power of the generator i.e. $250\,kW$. Thus four different types of simulations are applied. The first type of simulation is the control strategy passive loading without capping of the input power of the generator. The second is passive loading with capping. The third is optimum control without capping and the fourth is optimum control with capping.

6.1.1 Uncapped Passive Loading

Passive loading is applied without capping of the input power of the generator. As explained in section 4.1.1, the value of the spring coefficient in passive loading is zero. The value of the damping coefficient is varied to maximize the average output power of the generator. By simulating the WEC for different values of damping coefficient, different values of average power are observed. Figure 6.1 shows how the values of the average mechanical and electrical power of the PMSG vary with different values of the damping coefficient. The optimal value of the damping coefficient that produces the maximum mean power is $266.6\,kN/(m/s)$ as seen in Figure 6.1. The values of average and peak electrical output power of the generator at this optimal value of the damping coefficient are $34.58\,kW$ and $301.50\,kW$ respectively. The average and peak mechanical input power of the generator are $35.01\,kW$ and $302.50\,kW$ respectively. The corresponding values of the peak force, peak speed and peak stroke distance of the WEC are $402.83\,kN$, $1.51\,m/s$ and $1.40\,m$ respectively. The plots that show variation of peak mechanical force, peak velocity and peak stroke position with respect to varying damping coefficient are placed in appendix A.6.
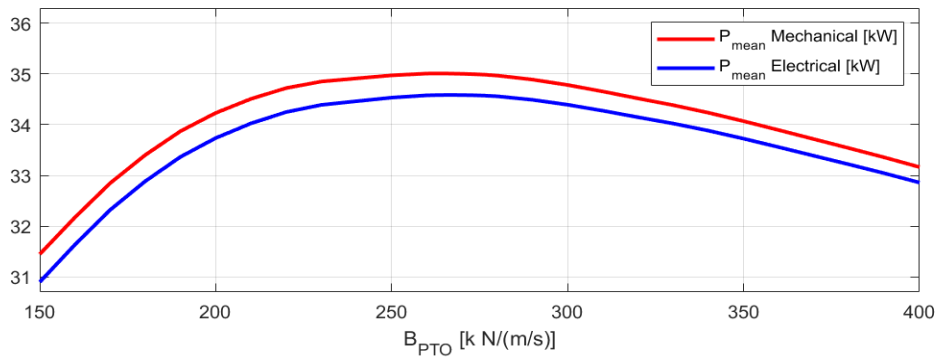

Figure 6.1: The mean mechanical and mean electrical power of PMSG in uncapped passive loading

The ratio of peak mechanical and peak electrical power, P_{peak}, to average mechanical and average electrical power, P_{mean}, is between 8.6 and 10 as shown in Figure 6.2.
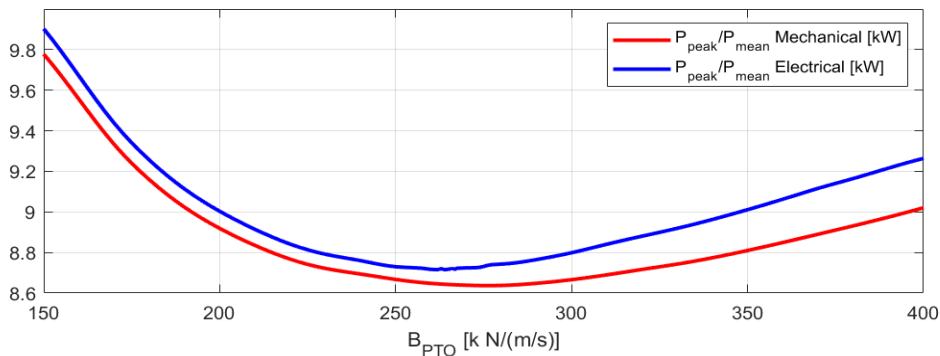

Figure 6.2: The ratio of peak mechanical and peak electrical to mean mechanical and mean electrical in uncapped passive loading

The voltage of phase a of the generator is shown in Figure 6.3. The voltage of the PMSG is limited to $475\,V$. The rms output voltage is $290.55\,V$.
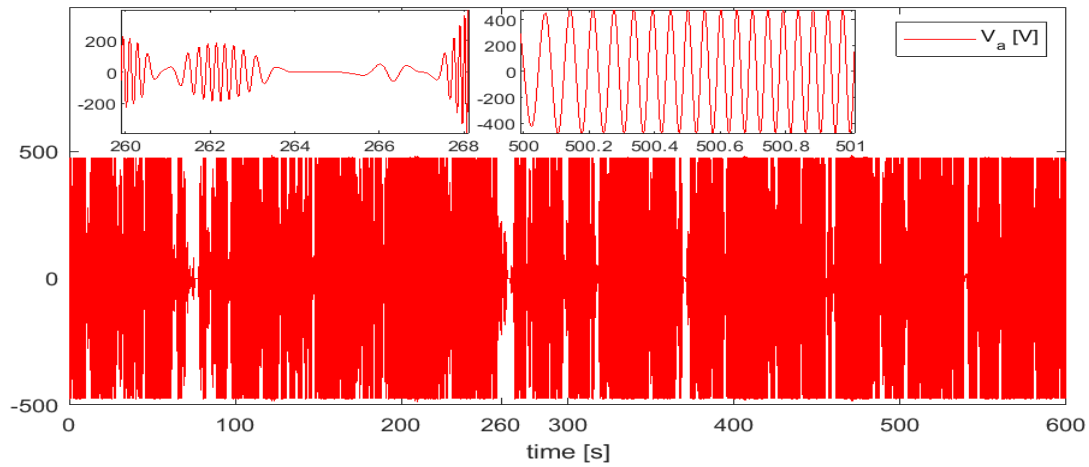

Figure 6.3: The voltage output of phase a of PMSG in uncapped passive loading

The current of the PMSG is shown in Figure 6.4 and Figure 6.5. The rms output current of the generator is $130.91\,A$ and the maximum current is $410.6\,A$. Figure 6.4 shows the d-axis current. The PMSG oscillates between constant torque and field-weakening region. As the rated current of the PMSG is $330\,A$, it is clearly seen from Figure 6.4 that there are instances where the d-axis current is greater than the rated current.
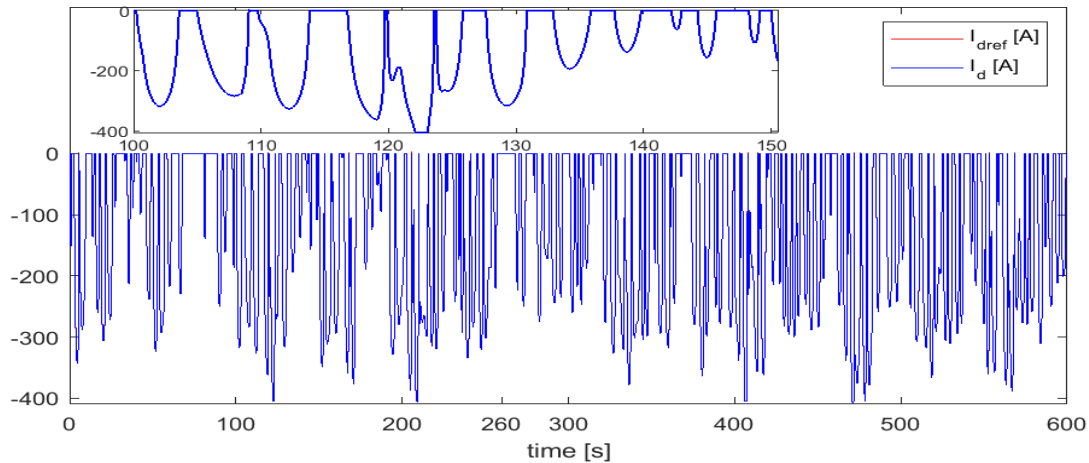

Figure 6.4: The d-axis reference and the d-axis current produced by PMSG in uncapped passive loading
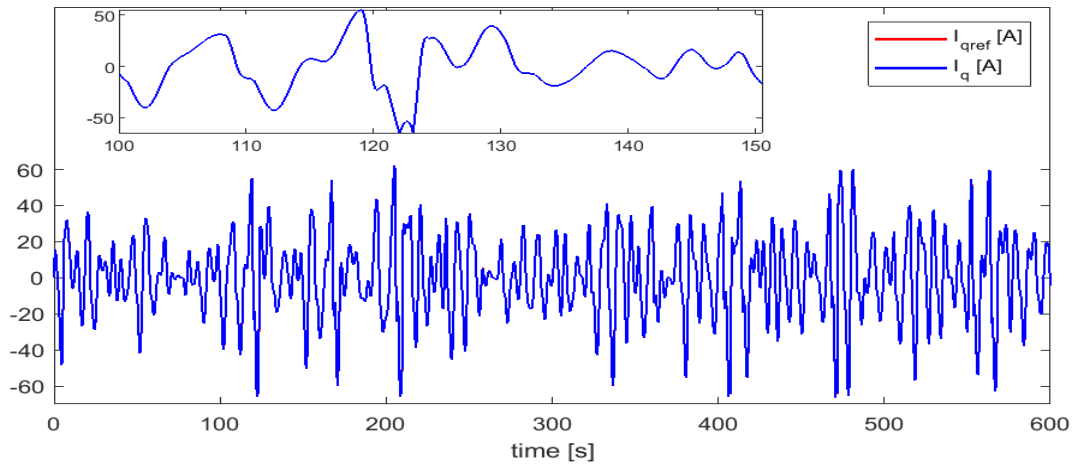
Figure 6.5: The q-axis reference and the q-axis current produced by PMSG in uncapped passive loading

The mechanical input power and the electrical output power are shown in Figure 6.6. The electrical power follows the mechanical power closely showing high efficiency.
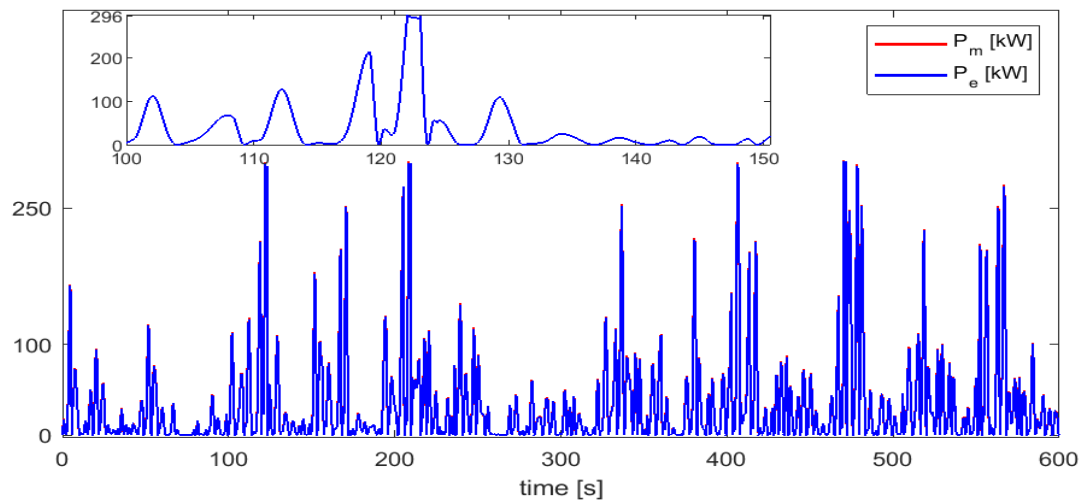

Figure 6.6: The mean mechanical and mean electrical power of PMSG in uncapped passive loading

6.1.2 Capped Passive Loading

In capped passive loading, a passive loading control strategy is applied on the WEC but the mechanical input power of the generator is capped to $250\,kW$. The WEC is simulated with varying values of the damping coefficient to find the value that produces the maximum average output power of the generator. Figure 6.7 shows the average mechanical input power and average electrical output power of the generator for different values of damping coefficient. The optimal value of damping coefficient that gives the maximum value of average output power is $267.80\,kN/(m/s)$. The average mechanical input power of the generator at this optimal value is $34.79\,kW$ and the average electrical output power of the generator is $34.37\,kW$. The corresponding value of the peak mechanical input power, peak electrical output power, peak force, peak speed and peak stroke position of the WEC are $256.51\,kW$, $254.67\,kW$, $258.75\,kN$, $1.61\,m/s$ and $1.44\,m$ respectively. The plots that show peak mechanical force, peak velocity and peak stroke position versus damping coefficient are placed in appendix A.7.
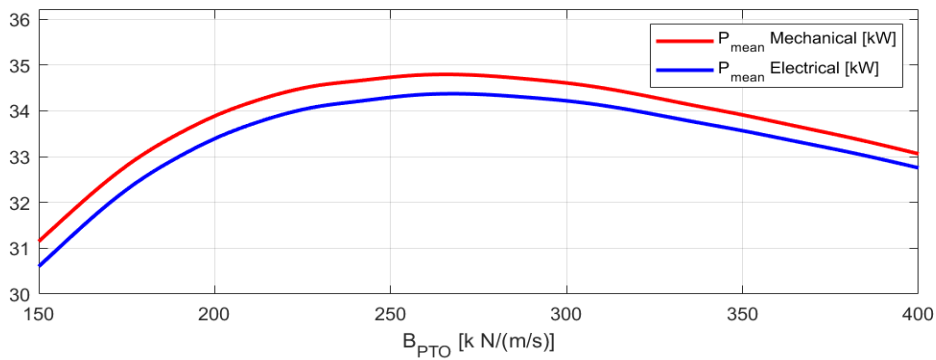

Figure 6.7: The mean mechanical input and the mean electrical output power of PMSG in capped passive loading

The ratio of peak electrical and peak mechanical to average electrical and average mechanical power in capped passive loading is shown in Figure 6.8 and it varies between 7.3 and 8.4.
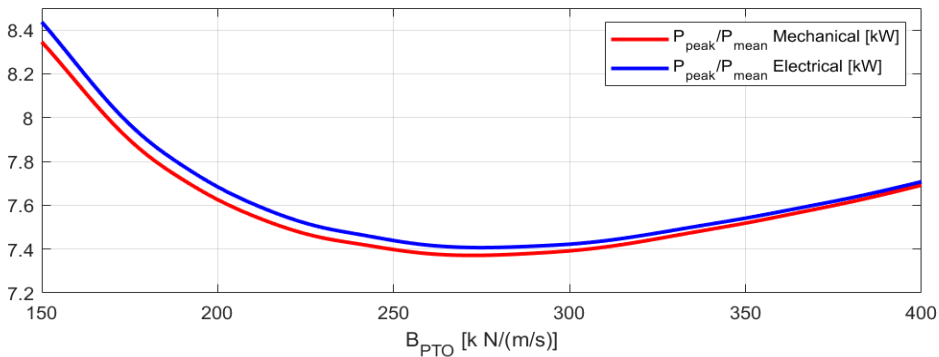

Figure 6.8: The ratio of peak electrical power to mean electrical power in capped passive loading

The voltage of phase a of the generator is shown in Figure 6.9 and it is limited to $475\,V$. The rms value of the output voltage is $290.54\,V$.
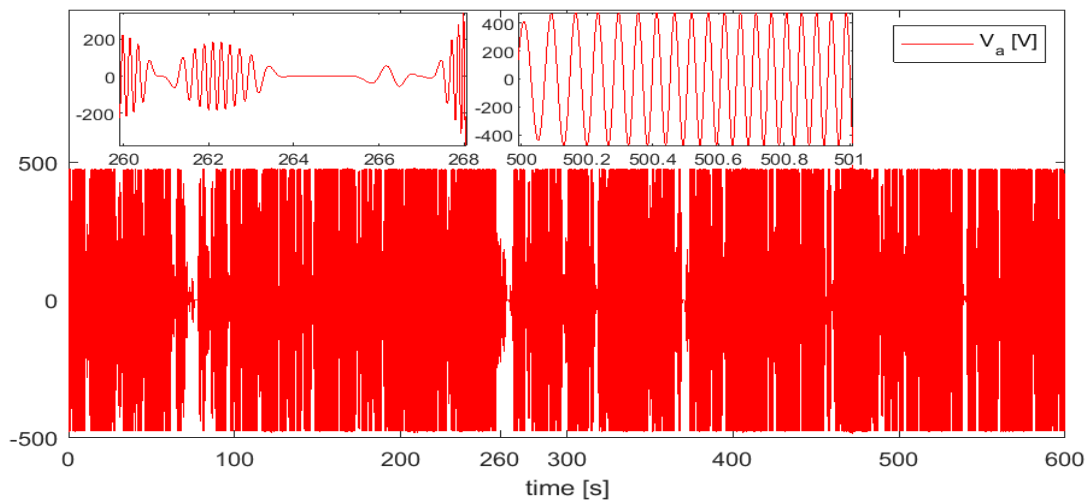
Figure 6.9: The voltage output of phase a of PMSG in capped passive loading

The output current of the generator is shown in Figure 6.10 and Figure 6.11. The rms value of the output current of the generator is $130.70\,A$ and the maximum current is $394.0\,A$. The d-axis current of the PMSG is shown in Figure 6.10. The q-axis current of the PMSG is shown in Figure 6.11.

Figure 6.10: The d-axis reference and the d-axis current produced by PMSG in capped passive loading

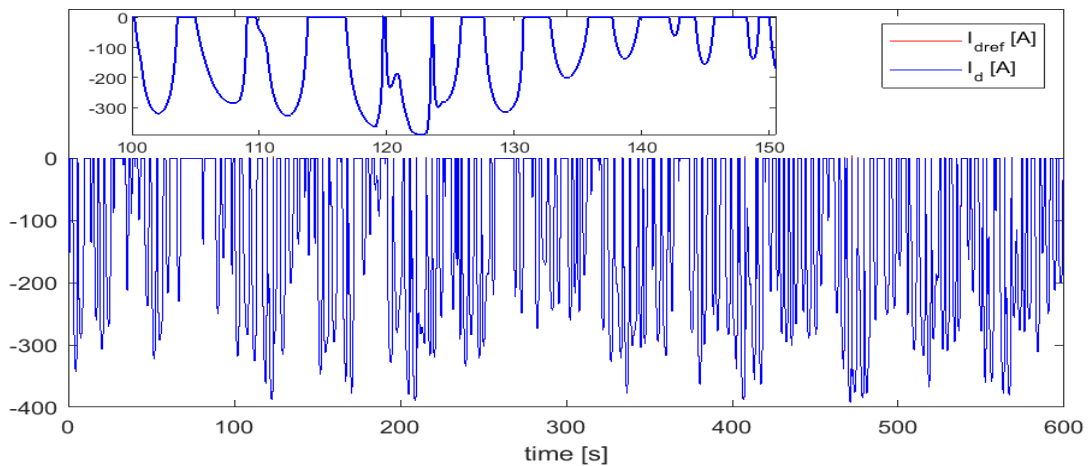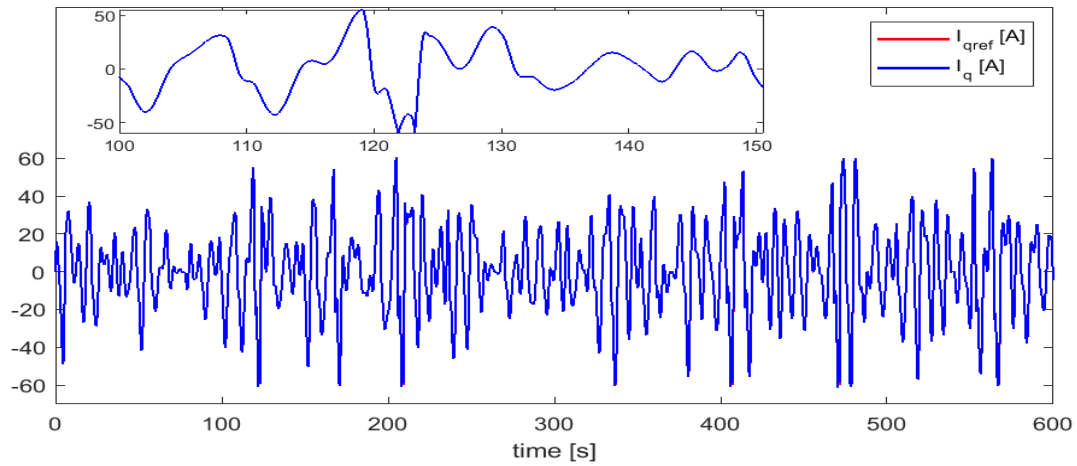**Figure 6.11:** The q-axis reference and the q-axis current produced by PMSG in capped passive loading

The mechanical input power and the electrical output power of the generator are shown in Figure 6.12.
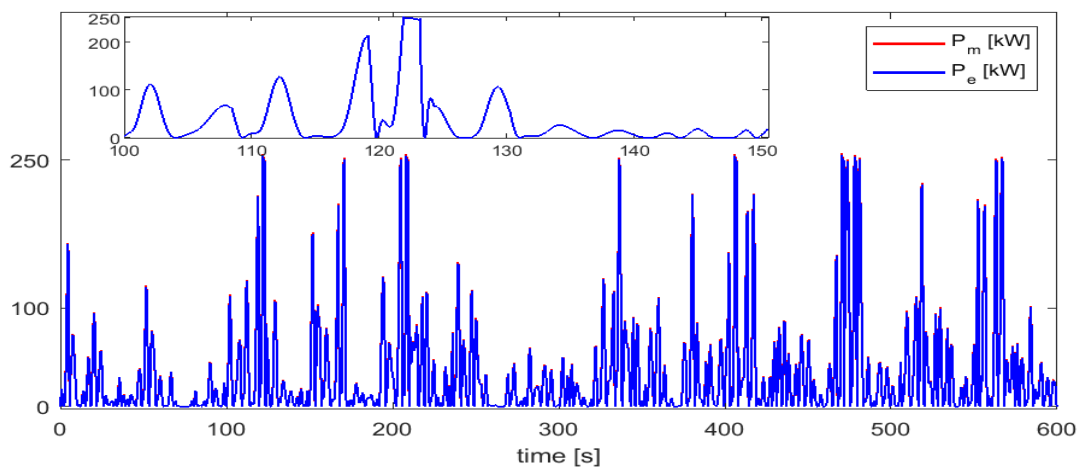

Figure 6.12: The mechanical input power and the electrical output power of PMSG in capped passive loading

6.1.3 Uncapped Optimum Control

Optimum control strategy applies both damping coefficient and spring coefficient to control the amplitude and phase of the WEC to extract the maximum power available. The maximum average electrical output power of $35.82\,kW$ is obtained. The value of the damping coefficient and spring coefficient at this optimal value are $150\,kN/(m/s)$ and $240\,kN/(m/s^2)$ respectively. Figure 6.13 shows how the values of the maximum average electrical output power of the PMSG with different values of the damping coefficient and spring coefficient. The maximum average mechanical input power of the PMSG is 36.28. The peak mechanical force, peak velocity and peak stroke distance are $490.27\,kN$, $1.42\,m/s$ and $1.47\,m$ respectively. The plots of peak mechanical force, mean mechanical power, peak mechanical power, peak electrical power, the ratio of peak to mean mechanical power, peak velocity and peak stroke distance are placed in appendix A.8.
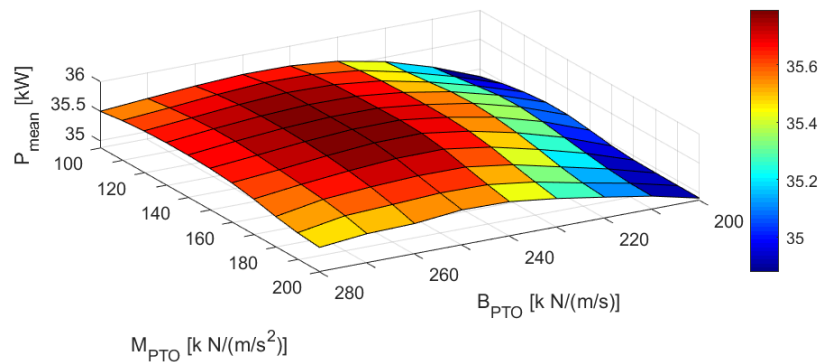
Figure 6.13: The plot of the mean electrical output power of PMSG in uncapped optimum control

The ratio of peak to mean electrical output power is shown in Figure 6.14. It varies between 8.6 and 9.
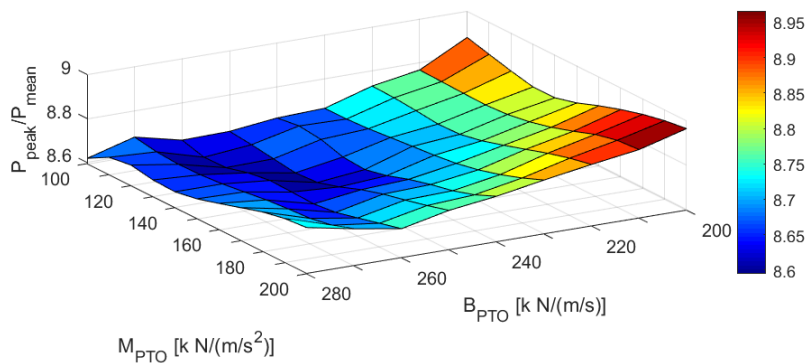
Figure 6.14: The ratio of peak electrical power to mean electrical power in uncapped optimum control

The voltage of phase a of the generator is shown in Figure 6.15. The rms value of the voltage is $291.10\,V$.

Figure 6.15: The plot of the voltage output of phase a of PMSG in uncapped optimum control

The generator produces a current of $136.93\,A$ rms and the maximum current is $415.0\,A$. Figure 6.16 shows the d-axis current. The PMSG oscillates between the constant torque and field-weakening regions and it generates i_d current higher than the rated current of the generator. The q-axis current is shown in Figure 6.17.
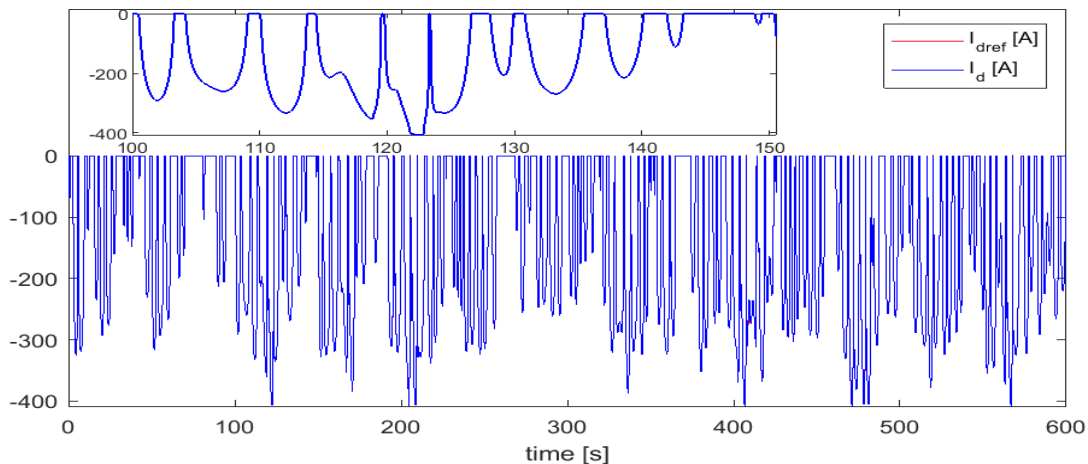
Figure 6.16: The d-axis reference and the d-axis current produced by PMSG in uncapped optimum control

Figure 6.17: The q-axis reference and the q-axis current produced by PMSG in uncapped optimum control

The mechanical input power and electrical output power of the generator with respect to time are shown in Figure 6.18.

Figure 6.18: The mechanical input power and the electrical output power of PMSG in uncapped optimum control

6.1.4 Capped Optimum Control

The mechanical input power is capped at $250\,kW$. The value of the damping coefficient and spring coefficient are varied to extract the maximum amount of power. A maximum average electrical power of $35.37\,kW$ is generated by applying a damping coefficient of $120\,kN/(m/s)$ and a spring coefficient of $260\,kN/(m/s^2)$. The average mechanical input power of the PMSG is $35.81\,kW$. The peak mechanical force, peak velocity and peak stroke distance are $327.04\,kN$, $1.50\,m/s$ and $1.49\,m$ respectively. The plots of peak mechanical force, mean mechanical power, peak mechanical power, peak electrical power, the ratio of peak to mean mechanical power, peak velocity and peak stroke distance are placed in appendix A.9.
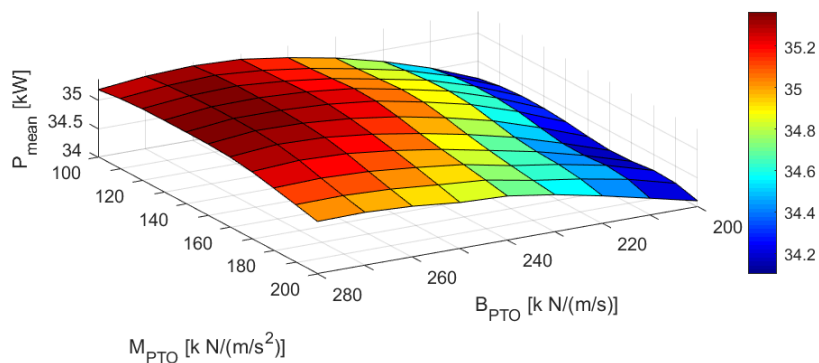
Figure 6.19: The plot of the mean electrical output power of PMSG in capped optimum control

The ratio of peak to mean electrical power is between 7 and 8.3 as shown in Figure 6.20.
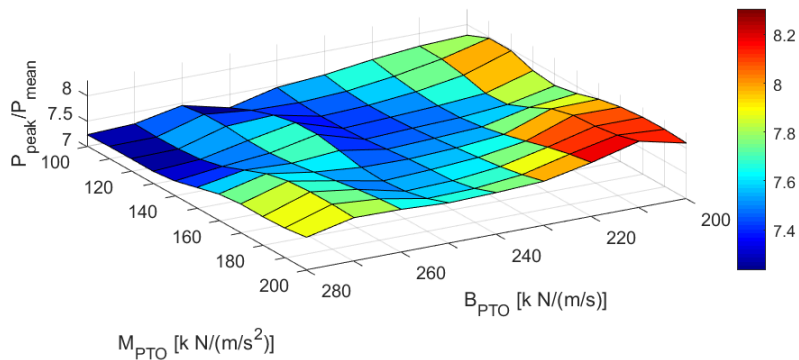
Figure 6.20: The ratio of peak electrical power to mean electrical power in capped optimum control

The voltage of phase a of the PMSG is shown in Figure 6.21. The rms voltage is $289.96\,V$.
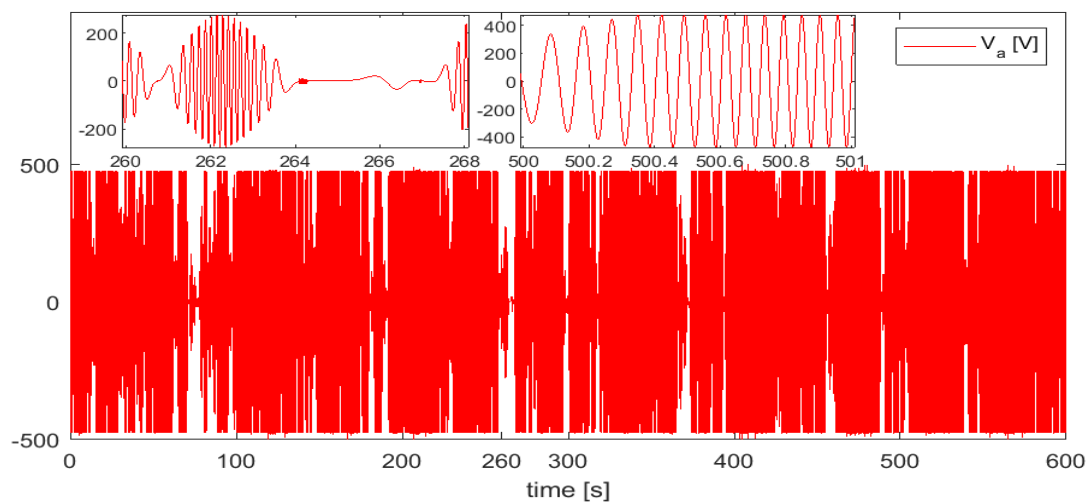
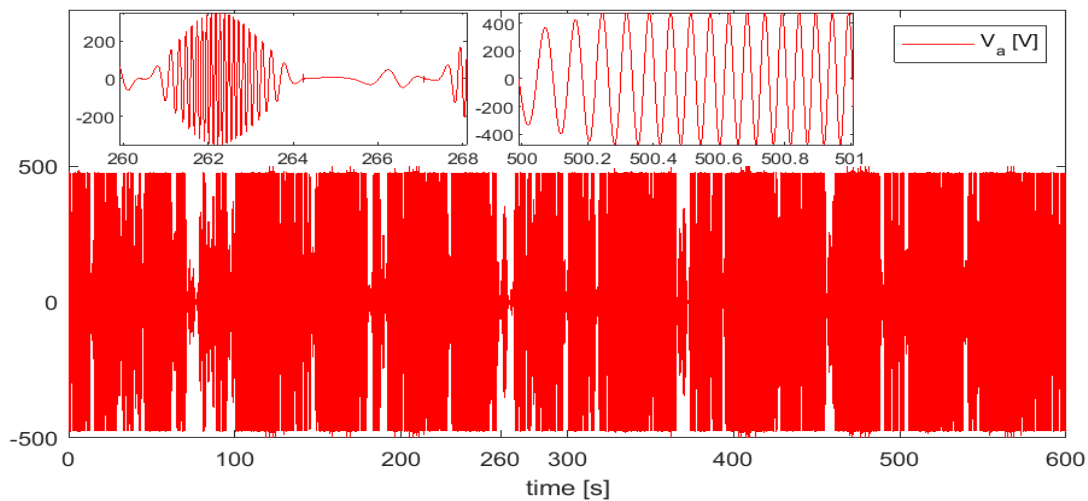**Figure 6.21:** The plot of the voltage output of phase a of PMSG in capped optimum control

The current output of the PMSG is $133.84\,A$ rms and the maximum current is $392.6\,A$. Figure 6.22 shows the d-axis current of the generator. The PMSG oscillates between the constant torque and field-weakening region. Figure 6.23 shows the q-axis current of the generator.
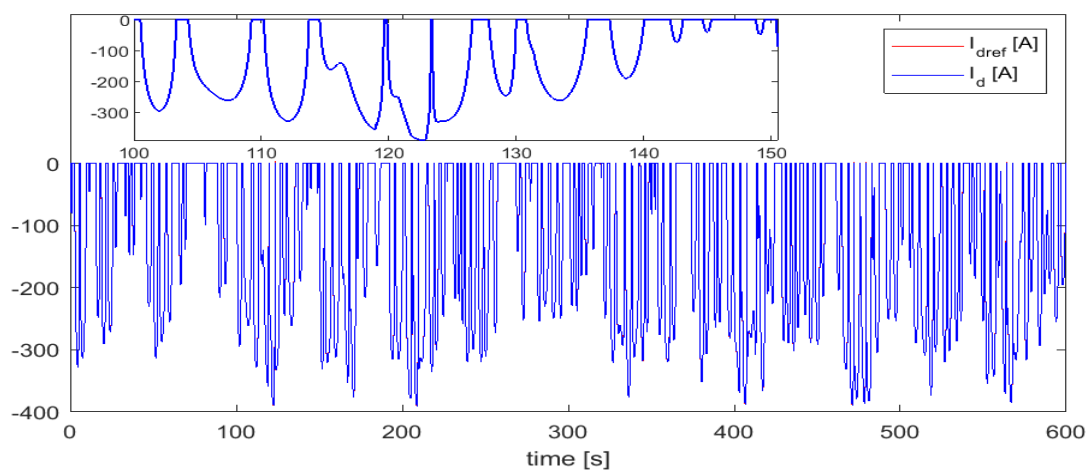
Figure 6.22: The d-axis reference and the d-axis current produced by PMSG in capped optimum control
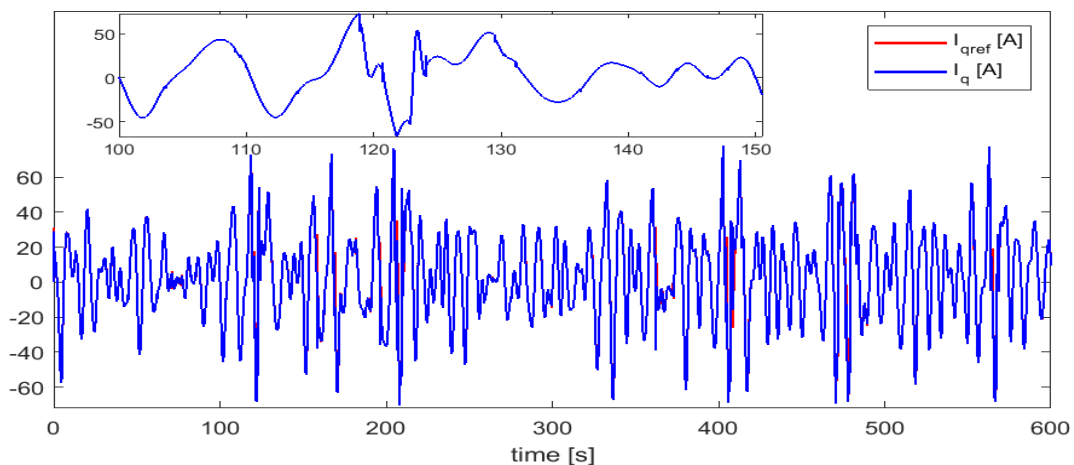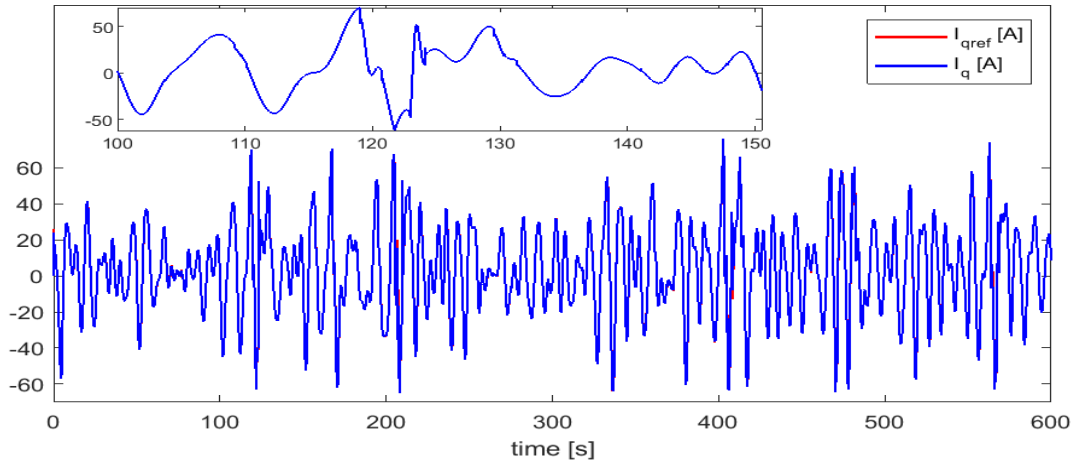
Figure 6.23: The q-axis reference and the q-axis current produced by PMSG in capped optimum control

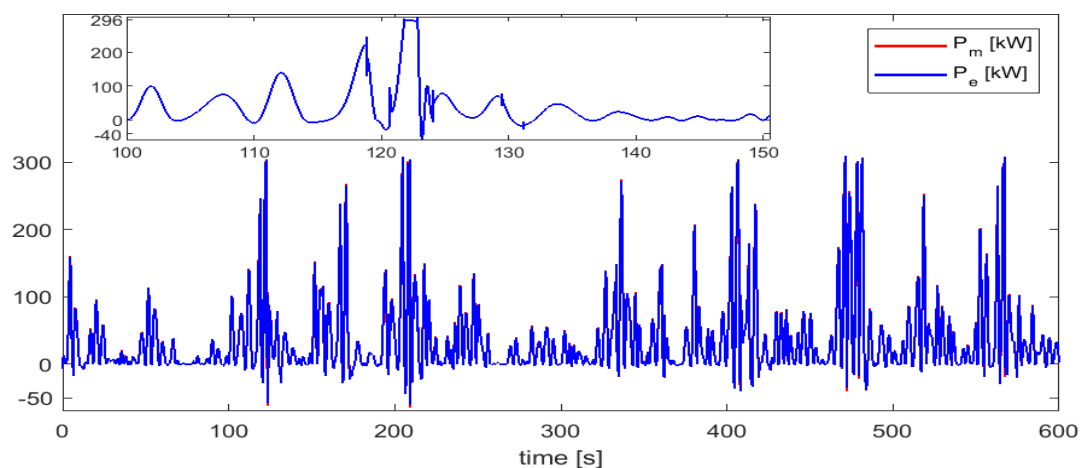The mechanical input power and electrical output power of the generator with respect to time are shown in Figure 6.24.
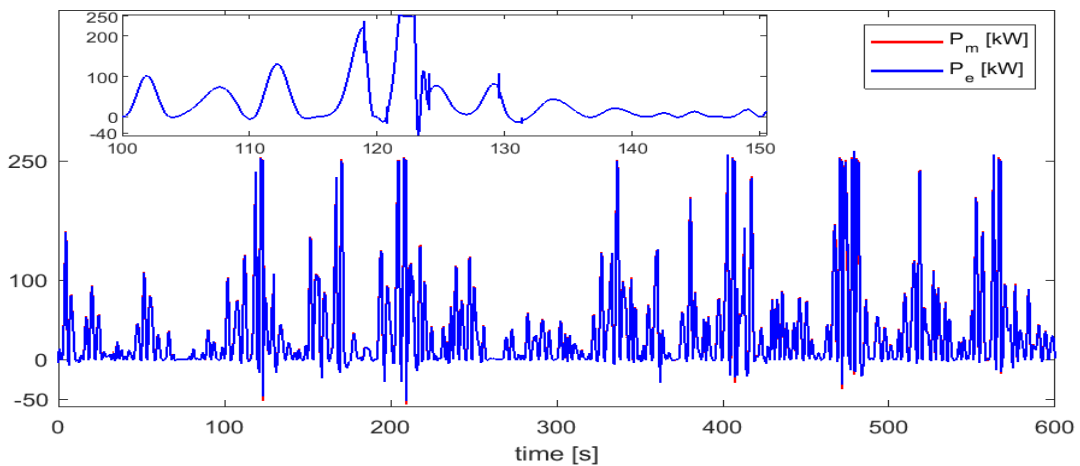
Figure 6.24: The mechanical input power and the electrical output power of PMSG in capped optimum control

This page intentionally left blank

Chapter 7

Discussion, Conclusion and Future Work

The point absorber is made to follow an optimal projectory to maximize the power extracted by a point absorber wave energy converter. The optimal trajectory is influenced by physical inertia, stiffness, damping, and PTO. The WEC physical characteristics like size, shape, and mass are constants. However, the WEC behavior can be influenced by varying the values of the stiffness and/or damping of the system. These variables are influenced through the PTO thereby increasing the power extracted from the incoming waves as shown in chapter 3. Thus, the WEC can resonate over a broad range of frequencies.

Chapter 4 shows that the rating of the generator and converter limit the maximum power the system can handle. Electric machines can operate transiently at high peak power while power electronics can not, due to their shorter thermal time constant. The constraints are set by evaluating the required rating of the generator and converter. Over-rating is costly. In chapter 6, an irregular wave of Bretschneider spectrum having a significant height of $3.25\,m$ and a peak period of $12\,s$ is simulated. The rating of the PMSG and converter employed is $250\,kW$. Two control strategies, passive loading and optimum control, are applied with and without capping the mechanical input power of the generator. The mechanical input power of the generator is capped at $250\,kW$. The maximum average power generated in uncapped passive loading is $34.58\,kW$ at a damping coefficient of $266.6\,k\frac{N}{m/s}$. The maximum average power generated in capped passive loading is $34.37\,kW$ at a damping coefficient of $267.8\,k\frac{N}{m/s}$. The maximum average power of $35.82\,kW$ is generated in uncapped optimum control when the value of the damping coefficient and spring coefficient are $240\,k\frac{N}{m/s}$ and $150\,k\frac{N}{m/s^2}$ respectively. The maximum average power generated by capped optimum control is $35.37\,kW$ when the damping coefficient and spring coefficient are $120\,k\frac{N}{m/s}$ and $260\,k\frac{N}{m/s^2}$ respectively. The uncapped optimum control generates the highest maximum average power of $35.82\,kW$. Comparing this value to uncapped passive loading, capped passive loading and capped optimum control, it is higher by 3.5%, 4% and 1.3% respectively.

The ratio of peak to average electrical output power in uncapped passive loading is between 8.6 and 10, and the ratio of peak to average mean electrical output power in uncapped optimum control is between 8.6 and 9. The peak power of each simulation as shown in Figure 6.6 and Figure 6.18 shows that the peak instantaneous power in each simulation is equal to the maximum power the generator can produce. Thus in both cases, the WEC produced peak power higher than the maximum power the generator can pro-

duce.

In [69], a simple analytical consideration of a sinusoidal wave of period 6 seconds and amplitude $0.5\,m$ is taken. The ratio of peak power to average power is examined in the case of passive loading and optimum control. The effect of increasing power capping on the ratio of peak power to average power is addressed. In the case of passive loading the average extracted power is $23.73\,kW$. Though the value of the peak power increased with increasing instantaneous power, the value of peak power is still double the value of average power. When optimum control is considered, an average power of $56.22\,kW$ is extracted. The ratio of peak power to average power is equal to 4.54. Under ideal conditions, the maximum average extracted power by optimum control is higher than passive loading at the expense of increased power electronics rating.

Irregular waves are also considered with the same ideal condition in [69], so as to compare to corresponding power performances with passive loading and optimum control discussed in the previous paragraph. The damping coefficient for maximum passive loading is close to the value for a sinusoidal incoming wave. The average extracted power is $18.38\,kW$. The result is a reduction of a quarter of the average power due to irregular waves. The ratio of peak to average extracted power is 7.7 to 17.1. In the case of optimum control, the average extracted power is $28.38\,kW$. The reduction of power is very significant compared to passive loading. The ratio of peak to average extracted power is found to be between 25.2 and 58.3. Thus, the need for a consistent overrating of electric machines and power electronics is emphasized in irregular waves. Thus, comparing the ratio of P_{peak} to P_{mean} of uncapped passive loading and uncapped optimum control to the ratio in irregular waves while taking into consideration the power limit described in section 4.3.1, the values are in the expected range.

The instantaneous extracted power from irregular waves is extremely fluctuating with sporadically very high peaks, for instance, Figure 6.6. The evaluation of the effect of capping in maximizing the average extracted power while limiting excessive overrating is important. The capping on the instantaneous power is implemented by reducing the PTO applied force. The ratio of peak to average electrical output power in capped passive loading and capped optimum control is between 7 and 8.5 as shown in Figure 6.8 and Figure 6.20. This is mainly due to the capping of the mechanical input power of $250\,kW$. The resulting reduction of average power due to capping was 0.6% and 1.3% in passive loading and optimum control respectively. However, both simulations have a peak electrical output power a little higher the power capping value. This is due to the power generated in Surge as PA3 has two degrees of freedom and also the delay of the actuator.

A test of power capping effect in irregular waves is implemented in [69]. A reduction of the capping of the maximum instantaneous power of 62% (from $P_{sat} = 147.04\,kW$ to $P_{sat} = 55.14\,kW$) results in a loss of only 3% of average power in passive loading. A corresponding reduction of capping of the maximum instantaneous power of 67% (from $P_{sat} = 1102.8\,kW$ to $P_{sat} = 367.6\,kW$) results in a loss of 19.5% of average power in optimum control. This shows that a significant decrease in the power electronics rating results in a limited drop of average extracted power.

The voltage of phase a of the generator in uncapped passive loading and capped passive

loading are shown in Figure 6.3 and Figure 6.9 respectively. The corresponding rms output voltage of the simulations are $290.55\,V$ and $290.54\,V$ respectively. The voltage of phase a of the generator in uncapped optimum control and capped optimum control are shown in Figure 6.15 and Figure 6.21 respectively. The corresponding rms output voltage of the simulations are $291.10\,V$ and $289.96\,V$ respectively. The voltage in each simulation is mostly sinusoidal and varies significantly in amplitude and frequency as the incident irregular wave has a varying amplitude and frequency. The rms voltage of optimum control is higher than passive loading as it generates higher power. The rms voltage is also lower in capped from uncapped as the maximum power generated is limited.

The d-axis current is very similar in all cases. The rms current of uncapped passive loading, capped passive loading, uncapped optimum control and capped optimum control are $130.91\,A$, $130.70\,A$, $136.93\,A$ and $133.84\,A$ respectively. The rms current is higher in optimal control than passive loading as it generates higher power. Similarly, the rms current is lower in capped than in the uncapped system. The mechanical input power varies significantly that the PMSG oscillates between constant torque and field-weakening region in all cases. The value of i_d is zero in the constant torque region while it is negative in the field-weakening region. Negative i_d increases the loss of the system decreasing the efficiency as described in section 5.3.2. There is some increase in the magnitude of negative i_d spikes in uncapped optimum control compared to other cases. The increase of absorbed power in uncapped optimum control increases the PMSG's speed generating higher negative i_d current. Higher negative i_d current increases losses and thereby reduces the average power generated. As the rated current of the PMSG is $330\,A$, there are instances where the d-axis current in all cases is greater than the rated current. However, the current of the generator is always less than the rated current of the converter, $500\,A$. The current limit of the generator is treated as a soft constraint as mentioned in section 5.6.

The q-axis current is the component of current that produces the power from the PMSG as shown in equation (5.19). The q-axis current from the generator follows the q-axis reference current, shown in Figure 6.5. The q-axis reference current is defined by the reference torque, which in itself is defined by the force from the WEC. The force in passive loading and optimum control is determined by equation (4.1) and equation (4.2) respectively. The q-axis current in uncapped optimum control as shown in Figure 6.17 has higher peak amplitudes than the other cases due to higher force from the WEC. The q-axis current in all cases does not reach a limiting value as expressed in equation (5.43). Therefore, it is not affected by it.

The electrical power in all cases follows the mechanical power closely showing high efficiency. The power curve in Figure 6.6 and Figure 6.12 shows that the flow of power in passive loading is in only one direction as the speed and force are in phase producing only positive power. The power curve in Figure 6.18 and Figure 6.24 shows that the flow of power is bidirectional as power is sent back to the WEC in some instances. The PMSG in optimum control operates as a motor when the power curve is negative. The influence of capping on output power is less significant as the output electrical is mostly below the capping value. The limitation of peak power by the maximum power of $296.20\,kW$ also reduce the power difference between uncapped and capped scenarios as the maximum power in uncapped cases is limited.

Chapter 6 shows that optimum control is suited well for small amplitude and high-frequency waves as it exploits the maximum energy of the waves. In cases of high waves, pure damping is suited so as not to exceed the peak power limit. In between these two scenarios, an intermediate reactive control could be applied to maximize the power output hereby providing a peak power lower than optimum control but higher than passive loading.

Optimum control generates higher power than passive loading. There are factors that reduce the maximum average power generated. The bidirectional flow of power in optimum control and the low efficiency of the PMSG due to low loading generates more power losses in optimum control. This reduces the average power output in optimum control than in passive loading. The limitation of the active power of the generator affects more to uncapped optimum control as optimum control produces higher peak power than passive loading. So, uncapped optimum control is the preferred control strategy to maximize the power generated in the wave-to-wire model of point absorber WEC shown in Figure 1.6 and it generates the maximum average power of $35.82\,kW$.

The future work can focus:

- Obtaining a PMSG that can produce higher peak power. Electric machines can operate transiently at high peak power. This is reached by increasing the rotor flux linkage or decreasing inductance of the PMSG. The maximum average power generated is increased and it is easier to evaluate the ratio of peak to average power generated.

- To take the wave spectrum of a defined location. To consider all the sea states present at that location and their occurrence probabilities.

- Replacing the average model VSC with a six-pulse three-phase controlled converter. IGBT can be chosen as switching devices and evaluate the changes that result.

- There are different physical constraints in WEC such as maximum stroke distance, maximum speed, and maximum torque. To take consideration of different physical constraints and their effect on the average power generated.

- The model in the master thesis is build up to the DC-link. It could be expanded to reach the grid and consider the influence and impact of it.

- Considering several WEC connected to the same DC link and study the impact on the ratio of peak to average power and power quality of the grid.

- To run the two control strategies of the WEC in the university laboratory and analyze the difference with the results of the MATLAB simulation of the wave-to-wire model.

Bibliography

[1] Rinkesh, *What is Wave Energy and How Wave Energy is Converted into Electricity? - Conserve Energy Future*. [Online]. Available: `https://www.conserve-energy-future.com/waveenergy.php` (visited on 05/15/2019).

[2] L. Wang, J. Isberg, and E. Tedeschi, "Review of control strategies for wave energy conversion systems and their validation: the wave-to-wire approach," *Renewable and Sustainable Energy Reviews*, no. August 2017, pp. 366–379, 2018.

[3] N. Khan, A. Kalair, N. Abas, and A. Haider, "Review of ocean tidal, wave and thermal energy technologies," *Renewable and Sustainable Energy Reviews*, vol. 72, no. October 2015, pp. 590–604, 2017.

[4] E. Tedeschi and M. Molinas, "Impact of control strategies on the rating of electric power take off for Wave Energy conversion," *Proceedings of the IEEE International Symposium on Industrial Electronics*, pp. 2406–2411, 2010.

[5] A. Clément, P. McCullen, A. F. d. O. Falcão, A. Fiorentino, F. Gardner, K. Hammarlund, G. Lemonis, T. Lewis, K. Nielsen, S. Petroncini, M. T. Pontes, P. Schild, B. Sjöström, H. C. Sørensen, and T. Thorpe, "Wave energy in Europe: current status and perspectives," *Renewable and Sustainable Energy Reviews*, vol. 6, no. 5, pp. 405–431, 2002.

[6] B. Drew, A. R. Plummer, and M. N. Sahinkaya, "A review of wave energy converter technology," *Proceedings of the Institution of Mechanical Engineers, Part A: Journal of Power and Energy*, vol. 223, no. 8, pp. 887–902, 2009.

[7] J. V. Taboada, H. L. Gelgele, O. Akevoll, W. E. Converter, O. Access, P. T. Off, R. Force, and H. Load, "Wave energy converter," *Master Thesis*, 2012.

[8] A. M. O'Hagan, C. Huertas, J. O'Callaghan, and D. Greaves, "Wave energy in Europe: Views on experiences and progress to date," *International Journal of Marine Energy*, vol. 14, pp. 180–197, 2016.

[9] M. D. Esteban, J.-S. López-Gutiérrez, and V. Negro, "Classification of wave energy converters," *Recent Adv Petrochem Sci*, vol. 2, pp. 2–5, 4 2017.

[10] Se Joon Lim, *Wave Energy Converters*, 2013. [Online]. Available: `http://large.stanford.edu/courses/2013/ph240/lim2/` (visited on 09/18/2018).

[11] I. López, J. Andreu, S. Ceballos, I. M. de Alegría, and I. Kortabarria, "Review of wave energy technologies and the necessary power-equipment," *Elsevier*, vol. 27, pp. 413–434, 2013.

[12] A. Babarit, "A database of capture width ratio of wave energy converters," *Renewable Energy*, vol. 80, pp. 610–628, 2015.

[13] J. Leijon and C. Boström, "Freshwater production from the motion of ocean waves – A review," *Desalination*, vol. 435, pp. 161–171, Jun. 2018.

[14] A. Viviano, S. Naty, E. Foti, T. Bruce, W. Allsop, and D. Vicinanza, "Large-scale experiments on the behaviour of a generalised Oscillating Water Column under random waves," *Renewable Energy*, vol. 99, pp. 875–887, 2016.

[15] M. Vieira, A. Sarmento, and L. Reis, "Failure analysis of the guide vanes of the Pico Wave Power Plant Wells turbine," *Engineering Failure Analysis*, vol. 56, pp. 98–108, Oct. 2015.

[16] C. B. Boake, T. J. T. Whittaker, M. Folley, and H. Ellen, "Overview and initial operational experience of the LIMPET wave energy plant," *In: Proceedings of The 12th International Offshore and Polar Engineering Conference, Japan, May 26-31*, vol. 3, pp. 586–594, 2002.

[17] M. V. Damme, "Distributions for wave overtopping parameters for stress strength analyses on flood embankments," *Coastal Engineering*, vol. 116, pp. 195–206, 2016.

[18] C. Altomare, T. Suzuki, X. Chen, T. Verwaest, and A. Kortenhaus, "Wave overtopping of sea dikes with very shallow foreshores," *Coastal Engineering*, vol. 116, pp. 236–257, 2016.

[19] J. P. Kofoed, P. Frigaard, E. Friis-Madsen, and H. C. Sørensen, "Prototype testing of the wave energy converter wave dragon," *Renewable Energy*, vol. 31, pp. 181–189, 2006.

[20] Johannes Falnes, "Research and Development in Ocean-Wave in Norway," *International Symposium on Ocean Energy Development, Muroran, Hokkando, Japan 1993*, 1993.

[21] C. Boström, "Electrical Systems for Wave Energy Conversion," PhD thesis, University of Uppsala, 2018, p. 105.

[22] A. Falca, "Wave energy utilization : A review of the technologies," *Renewable and Sustainable Energy Reviews*, vol. 14, pp. 899–918, 2010.

[23] E. Lejerskog, C. Boström, L. Hai, R. Waters, and M. Leijon, "Experimental results on power absorption from a wave energy converter at the Lysekil wave energy research site," *Renewable Energy*, vol. 77, pp. 9–14, 2015.

[24] J. Xie and L. Zuo, "Dynamics and control of ocean wave energy converters," *International Journal of Dynamics and Control*, vol. 1, no. 3, pp. 262–276, 2013.

[25] A Weinstein, Goran Fredrikson, L Claeson, Jan Forsberg, M.J.Parks, Kim Nielsen, M.S. Jenses, Khatereh Zandiyeh, Peter Frigaard, M Kramer, Thomas Andersen, "AquaBuOY - The offshore wave energy converter numerical modeling and optimization," *Energy*, vol. 4, 2003.

[26] J. Weber, R. Costello, F. Mouwen, J. Fingwood, and G. Thomas, "Techno-economic WEC system optimisation - Methodology applied to Wavebob system definition," *3rd International Conference on Ocean Energy*, Nov 2014, 2010.

[27] Ocean Power Technologies Inc, "Making Waves in Power - Annual Report of Ocean Power Technology," Apr 30, 2009.

[28] C. Josset, A. Babarit, and A. H. Clément, "A wave-to-wire model of the SEAREV wave energy converter," *Proceedings of the Institution of Mechanical Engineers Part M: Journal of Engineering for the Maritime Environment*, vol. 221, no. 2, pp. 81–93, 2015.

[29] M. G. de Sousa Prado, F. Gardner, M. Damen, and H. Polinder, "Modelling and test results of the Archimedes wave swing," *Proceedings of the Institution of Mechanical Engineers, Part A: Journal of Power and Energy*, vol. 220, no. 8, pp. 855–868, 2006.

[30] C. D. Engin and A. Yeşildirek, "Designing and modeling of a point absorber wave energy converter with hydraulic power take-off unit," *2015 4th International Conference on Electric Power and Energy Conversion Systems, EPECS 2015*, 2015.

[31] OpenLearn - Open University, *Models and modelling*, 2018. [Online]. Available: `https://www.open.edu/openlearn/science-maths-technology/computing-and-ict/models-and-modelling/content-section-2.1` (visited on 06/13/2019).

[32] J. Sjolte, G. Tjensvoll, and M. Molinas, "Power Collection from Wave Energy Farms," *Applied Sciences*, vol. 3, no. 2, pp. 420–436, 2013.

[33] H. Titah-benbouzid and Benbouzid, "An Up-to-Date Technologies Review and Evaluation of Wave Energy Converters," *International Review of Electrical Engineering - IREE*, p. 5, 2015.

[34] J. Zhang, H. Yu, Q. Chen, M. Hu, L. Huang, and Q. Liu, "Design and Experimental Analysis of AC Linear Generator With Halbach PM Arrays for Direct-Drive Wave Energy Conversion," *IEEE Transactions on Applied Superconductivity*, vol. 24, no. 3, pp. 1–4, 2014.

[35] N. Hodgins, O. Keysan, A. S. Mcdonald, and M. A. Mueller, "Design and Testing of a Linear Generator for Wave-Energy Applications," *IEEE Transactions on Industrial Electronics*, vol. 59, no. 5, pp. 2094–2103, 2012.

[36] R. Vermaak, M. J. Kamper, and S. Member, "Design Aspects of a Novel Topology Air-Cored Permanent Magnet Linear Generator for Direct Drive Wave Energy Converters," *IEEE Transactions on Industrial Electronics*, vol. 59, no. 5, pp. 2104–2115, 2012.

[37] T. K. Brekken, "On Model Predictive Control for a point absorber Wave Energy Converter," *Proceedings of the IEEE Trondheim PowerTech*, pp. 1–8, 2011.

[38] C. Boström, B. Ekergård, R. Waters, S. Member, and M. Eriksson, "Linear Generator Connected to a Resonance-Rectifier Circuit," vol. 38, no. 2, pp. 255–262, 2013.

[39] L. Cappelli, S. Member, F. Marignetti, S. Member, G. Mattiazzo, E. Giorcelli, G. Bracco, S. Carbone, C. Attaianese, and S. Member, "Linear Tubular Permanent-Magnet Generators for the Inertial Sea Wave Energy Converter," *IEEE Transactions on Industry Applications*, vol. 50, no. 3, pp. 1817–1828, 2014.

[40] S. Olaya, J.-M. Bourgeot, and M. Benbouzid, "Modelling and Preliminary Studies for a Self-Reacting Point Absorber WEC," *First International Conference on Green Energy ICGE*, pp. 14–19, 2014.

[41]   N. Muller, S. Kouro, J. Glaria, and M. Malinowski, "Medium-voltage power converter interface for Wave Dragon wave energy conversion system," *Energy Conversion Congress and Exposition*, pp. 352–358, 2013.

[42]   M. S. Lagoun, A. Benalia, and M. E. H. Benbouzid, "A Predictive power control of Doubly Fed Induction Generator for Wave Energy Converter in Irregular Waves," *2014 First International Conference on Green Energy ICGE 2014*, pp. 26–31, 2014.

[43]   M. S. Lagoun, S. Nadjem, A. Benalia, and M. E. H. Benbouzid, "Predictive Power Control of Doubly-Fed Induction Generator for Wave Energy Conveters," *2nd International Symposium On Environment Friendly Energies And Applications*, pp. 312–317, 2012.

[44]   M. Alberdi, M. Amundarain, A. Garrido, and I. Garrido, "Neural control for voltage dips ride-through of oscillating water column-based wave energy converter equipped with doubly-fed induction generator," *Renewable Energy*, vol. 48, pp. 16–26, 2012.

[45]   M. Alberdi, M. Amundarain, A. J. Garrido, I. Garrido, and F. J. Maseda, "Fault-Ride-Through Capability of Wave-Power-Generation Plants Equipped With Doubly Fed Induction Generator and Airflow Control," *IEEE Transactions on Industrial Electronics*, vol. 58, no. 5, pp. 1501–1517, 2011.

[46]   B. Li, D. Macpherson, and J. Shek, "Direct drive wave energy converter control in irregular waves," *IET Conference on Renewable Power Generation*, pp. 64–64, 2012.

[47]   M. Yemane, "Modeling and Control of Wave Energy Converters," *Semester Project, Electrical Power Engineering , NTNU*, p. 50, 2018.

[48]   I. V.Lavrenov, *Wind-Waves in Oceans: Dynamics and Numerical Simulations.* R. Guzzi, L. J. Lanzerotti, D. Imboden, and U. Platt, Eds. 1993, p. 367.

[49]   M. A. Maâtoug and M. Ayadi, "Numerical simulation of the second-order Stokes theory using finite difference method," *Alexandria Engineering Journal*, vol. 55, no. 3, pp. 3005–3013, 2016.

[50]   National Renewable Energy Laboratory and Sandia Corporation, *Theory — WEC-Sim documentation*, 2015. [Online]. Available: `http://wec-sim.github.io/WEC-Sim/theory.html` (visited on 09/18/2018).

[51]   J. Hals, B. Aurelien, A. Kurniawan, M. Muliawan, T. Moan, and J. Krokstad, "The NumWEC project: Numerical estimation of energy delivery from a selection of wave energy converters," no. December, 2011.

[52]   M. Folley, *Numerical Modelling of Wave Energy Converters*, R. Zanol, Ed. Joe Hayton, 2016, p. 305.

[53]   J. Davidson and J. V. Ringwood, "Mathematical modelling of mooring systems for wave energy converters - A review," *Energies*, vol. 10, no. 5, 2017.

[54]   J. Hals, "Jørgen Hals Modelling an phase control of wave-energy converters Jørgen Hals Modelling and phase control of wave-energy converters," PhD thesis, NTNU, Trondheim, 2010, p. 258.

[55] J. D. Nolte and R. C. Ertekin, "Wave power calculations for a wave energy conversion device connected to a drogue," *Journal of Renewable and Sustainable energy 6, 013117*, 2014.

[56] F. D. O. Falca, "Phase control through load control of oscillating-body wave energy converters with hydraulic PTO system," vol. 35, pp. 358–366, 2008.

[57] W. Cummins, "The Impulse Response Function and Ship Motions," vol. 1661, 1962.

[58] J. Falnes, "On non-causal impulse response functions related to propagating water waves," *Applied Ocean Research*, vol. 17, no. 6, pp. 379–389, 1995.

[59] E. Al Shami, R. Zhang, and X. Wang, "Point absorber wave energy harvesters: A review of recent developments," *Energies*, vol. 12, no. 1, p. 6, 2019.

[60] A. Pecher and J. P. Kofoed, *Ocean Engineering & Oceanography 7 Handbook of Ocean Wave Energy*. Springer Nature, 2017, p. 283.

[61] University of Strathclyde, *Power Take Off - Analysis of Cost Reduction Opportunities in the Wave Energy Industry*. [Online]. Available: `http://www.esru. strath.ac.uk/EandE/Web_sites/14-15/Wave_Energy/power- take-off.html` (visited on 11/23/2018).

[62] J. Falnes, *Ocean Waves and Oscillating Systems: Linear Interaction Including Wave Energy Extraction, Cambridge, UK*. Cambridge University Press, 2002, p. 220.

[63] O. Abdelkhalik, R. Robinett, S. Zou, G. Bacelli, R. Coe, D. Bull, D. Wilson, and U. Korde, "On the control design of wave energy converters with wave prediction," *Journal of Ocean Engineering and Marine Energy*, vol. 2, no. 4, pp. 473–483, 2016.

[64] J. Falnes and A. Kurniawan, "Fundamental formulae for wave-energy conversion," *Royal Society Open Science*, vol. 2, no. 3, 2015.

[65] T. Zhou, "Damping Profile Research for Corpower Ocean's Wave Energy Converter," *Master Thesis*, 2016.

[66] D. Rowell and D. Wormley, *System Dynamics: An Introduction*. Prentice Hall, 1997.

[67] L. Alberti, E. Tedeschi, N. Bianchi, M. Santos, and A. Fasolo, "Effect of the generator sizing on a wave energy converter considering different control strategies," *COMPEL - The international journal for computation and mathematics in electrical and electronic engineering*, vol. 32, no. 1, pp. 233–247, 2012.

[68] E. Tedeschi and M. Molinas, "Tunable control strategy for wave energy converters with limited power takeoff rating," *IEEE Transactions on Industrial Electronics*, vol. 59, no. 10, pp. 3838–3846, 2012.

[69] E. Tedeschi, M. Carraro, M. Molinas, and P. Mattavelli, "Effect of control strategies and power take-off efficiency on the power capture from sea waves," *IEEE Transactions on Energy Conversion*, vol. 26, no. 4, pp. 1088–1098, 2011.

[70] G. Bacelli, "Optimal control of wave energy converters," Maynooth University, Tech. Rep., 2014, p. 206.

[71] The Australian Office for Learning and Teaching, School of Physics, UNSW 2052, and A. Sydney, *Wave, power and radiation - Physclips waves and sound.* [Online]. Available: `http://www.animations.physics.unsw.edu. au/jw/waves%7B%5C_%7Dpower.htm` (visited on 11/24/2018).

[72] J. Hals, J. Falnes, and T. Moan, "A Comparison of Selected Strategies for Adaptive Control of Wave Energy Converters," *J. Offshore Mech. Eng 133(3), 031101 (Mar 29, 2011)*, p. 12, 2011.

[73] V. Kurupath, R. Ekstrom, and M. Leijon, "Optimal Constant DC Link Voltage Operation of a Wave Energy Converter," *energies*, vol. 6, pp. 1993–2006, 2013.

[74] National Renewable Energy Laboratory and US department of Energy, *WEC-Sim — NWTC Information Portal*, 2017. [Online]. Available: `https://nwtc. nrel.gov/WEC-Sim` (visited on 05/18/2019).

[75] "IMAGINE – Task 2.1 WEC-Sim model progress," *Cruz atcheson Consulting Engineering*, pp. 4–5, 2018.

[76] UMBRAGROUP SPA, *Imagine — Innovative Method for Affordable Generation IN ocean Energy*, 2018. [Online]. Available: `https://h2020-imagine. eu/` (visited on 06/14/2019).

[77] Innovation and Networks Executive Agency, *IMAGINE - Innovative Method for Affordable Generation IN ocean Energy*. [Online]. Available: `https://ec. europa.eu/inea/en/horizon-2020/projects/h2020-energy/ tidal-wave-hydropower/imagine` (visited on 06/14/2019).

[78] L. Castellini, M. D'Andrea, M. Martini, G. Alessandri, D. Coiro, F. De Luca, G. Calise, G. Troise, and A. Vogler, "Experimental tests on a wave-to-wire pivoted system for wave energy exploitation," *2017 6th International Conference on Clean Electrical Power: Renewable Energy Resources Impact, ICCEP 2017*, pp. 479–487, 2017.

[79] A. H. Techet, "Ocean Waves Spring 2005," *Lecture Notes: MIT Ocean Engineering*, p. 6, 2015.

[80] D. Alcorn, Raymond O'Sullivan, "Implication of control schemes for electrical system design in wave energy converters," in *Electrical Design for Ocean Wave and Tidal Energy Systems*, Institution of Engineering and Technology, 2014, ch. 8, pp. 286–296.

[81] D. OSullivan, D. Murray, J. Hayes, M. G., and A. W., "The Benefits of Device Level Short Term Energy Storage in Ocean Wave Energy Converters," *Energy Storage in the Emerging Era of Smart Grids*, p. 448, 2012.

[82] M. Stålberg, R. Waters, O. Danielsson, and M. Leijon, "Influence of Generator Damping on Peak Power and Variance of Power for a Direct Drive Wave Energy Converter," *Journal of Offshore Mechanics and Arctic Engineering*, vol. 130, no. 3, p. 031 003, 2008, ISSN: 08927219.

[83] M. Molinas, O. Skjervheim, P. Andreasen, T. Undeland, J. Hals, T. Moan, and B. Sørby, "Power electronics as grid interface for actively controlled wave energy converters," *2007 International Conference on Clean Electrical Power, ICCEP '07*, pp. 188–195, 2007.

[84] E. Tedeschi and M. Molinas, "Control Strategy of Wave Energy Converters Optimized Under Power Electronics Rating Constraints," *Proceedings of the 3rd International Conference on Ocean Energy (ICOE 2010)*, pp. 1–6, 2010.

[85] H. Lendenmann, K.-C. Strømsem, M. D. Pre, W. Arshad, A. Leirbukt, G. Tjensvoll, and T. Gulli, "Direct generation wave energy converters for optimized electrical power production," *Proceedings of the 7th European Wave and Tidal Energy Conference (EWTEC07)*, 2007.

[86] S Bharadwaj Reddy, *Advantages & Disadvantages Induction Motor, Electrical Machines, Tools*. [Online]. Available: `https://instrumentationtools.com/advantages-disadvantages-induction-motor/` (visited on 03/31/2019).

[87] B. Bits, "Permanent Magnet Synchronous Motor Control High-performance and power-efficient motor control," pp. 1–2, 2012. [Online]. Available: `https://cache.freescale.com/files/industrial/doc/brochure/BBPRMMAGSYNART.pdf`.

[88] MathWorks, *Permanent magnet synchronous motor with sinusoidal flux distribution (PMSM)*. [Online]. Available: `https://se.mathworks.com/help/physmod/sps/ref/permanentmagnetsynchronousmotor.html` (visited on 03/08/2019).

[89] Christopher Jaszczolt, *Understanding permanent magnet motors - Control Engineering*, 2017. [Online]. Available: `https://www.controleng.com/articles/understanding-permanent-magnet-motors/` (visited on 06/02/2019).

[90] *Advantages and Disadvantages of the PMSG Generator*, 2018. [Online]. Available: `http://energyprofessionalsymposium.com/?p=30652` (visited on 03/20/2019).

[91] Microsemi Corporation, "Par, Inverse Park and Clarke, Inverse Clarke Transformations MSS Software Implementation - User Guide," p. 20, 2013.

[92] A. Vasile, "Grid Monitoring and Advanced Control of Distributed Power Generation Systems," Insitut for Energiteknik, Aalborg Universitet, Tech. Rep., 2007, p. 213.

[93] MathWorks, *Clarke Transform - MATLAB - MathWorks Nordic*. [Online]. Available: `https://se.mathworks.com/help/physmod/sps/ref/clarketransform.html` (visited on 03/20/2019).

[94] Y. Gyihui, C. Cai, and L. Wang, "A Three-phase Active Power Filter Based on PARK Transformation," *2009 4th International Conference on Computer Science & Education*, pp. 1221–1224, 2009.

[95] MathWorks, *Park Transform - MATLAB - MathWorks Nordic*. [Online]. Available: `https://se.mathworks.com/help/physmod/sps/ref/parktransform.html` (visited on 03/20/2019).

[96] D. N. Zmood and D. G. Holmes, "Stationary frame current regulation of PWM inverters with zero steady-state error," *IEEE Transactions on Power Electronics*, vol. 18, no. 3, pp. 814–822, 2003.

[97] T. Jerčić, Š. Ileš, D. Žarko, and J. Matuško, "Constrained field-oriented control of permanent magnet synchronous machine with field-weakening utilizing a reference governor," *Automatika*, vol. 58, no. 4, pp. 439–449, 2018.

[98] V.-S. Sularea, "Design and Control of high efficiency wind turbine based hydrogen production system," PhD thesis, 2016, p. 116.

[99] P. C. Krause, O. Wasynczuk, and S. D. Sudhoff, *Analysis of Electric Machinery and Drive Systems*, Second. John Wiley & Sons, Inc., 2002, p. 632.

[100] R. Nilsen, *Electric Drives*. Trondheim, 2018, p. 255.

[101] C. Bajracharya, M. Molinas, J. A. Suul, and T. M. Undeland, "Understanding of tuning techniques of converter controllers for VSC-HVDC," *Proceedings of the Nordic Workshop on Power and Industrial Electronics (NORPIE/2008)*, pp. 1–8, 2008.

[102] J. Sjolte, C. M. L. Sandvik, E. Tedeschi, and M. Molinas, "Exploring the potential for increased production from the wave energy converter lifesaver by reactive control," *Energies*, vol. 6, no. 8, pp. 3706–3733, 2013.

[103] Jeffrey Jenkins, *Charged EVs — A closer look at back electromotive force*, 2013. [Online]. Available: `https://chargedevs.com/features/a-closer-look-at-back-electromotive-force/` (visited on 06/03/2019).

[104] T. Martin and R. Burke, "Practical field weakening current vector control calculations for PMSM in vehicle applications," *2013 World Electric Vehicle Symposium and Exhibition, EVS 2014*, pp. 1–7, 2014.

[105] J. A. Houldsworth and D. A. Grant, "The Use of Harmonic Distortion to Increase the Output Voltage of a Three-Phase PWM Inverter," *IEEE Transactions on Industry Applications*, vol. IA-20, no. 5, pp. 1224–1228, 1984.

[106] E. Alves, D. Andrade, and E. Tedeschi, "D5.1 - EMG control strategy analysis report," pp. 120–121, 2019.

Detailed steps of equations

A.1 Space-State analysis of a mass-spring-damper system

Space-State analysis of a mass-spring-damper system equivalent representing the point absorber for section 3.2:

$$\begin{bmatrix} \dot{z}_1 \\ \dot{z}_2 \end{bmatrix} = \begin{bmatrix} 0 & 1 \\ -S/m & -R/m \end{bmatrix} \begin{bmatrix} z_1 \\ z_2 \end{bmatrix} + \begin{bmatrix} 0 \\ 1/m \end{bmatrix} u_1$$

Representing the above equation in state-variable form:

$$\dot{z} = Ez + Fu \tag{A.1a}$$

$$y = Gz + Lu \tag{A.1b}$$

By using Laplace transform the above equations can be written as:

$$sZ(s) = EZ(s) + FU(s) \tag{A.2a}$$

$$Y(s) = GZ(s) + LU(s) \tag{A.2b}$$

By moving Z(s) to the left from equation (A.2a):

$$Z(s) = (sI - E)^{-1} F \tag{A.3}$$

By solving the vectorial differential equation (A.2a), the solution for $z(t)$ is:

$$z(t) = e^{E(t-t_o)} z(t_o) + \int_{t_0}^{t} e^{E(t-\tau)} Fu(\tau) \, d\tau \tag{A.4}$$

where the matrix exponential is defined as the series

$$e^{At} = I + At + \frac{1}{2!} A^2 t^2 + \frac{1}{3!} A^3 t^3 + \dots$$

Inserting equation (A.4) into (A.2b), the output vector is:

$$y(t) = Ge^{E(t-t_o)} z(t_o) + \int_{t_0}^{t} Ge^{E(t-\tau)} Fu(\tau) \, d\tau + Lu(t)$$

A.2 The Expression for average power

The detailed steps to derive equation (4.5), the expression for average power in electric analogue in section 4.3.3:

$$P_{mean} = I^2 R_{PTO}$$

$$P_{mean} = \frac{E^2 R_{PTO}}{(R_{wec} + R_{PTO})^2 + (X_{wec} \pm X_{PTO})^2}$$

and

$$X_{PTO} = \sqrt{Z_{PTO}^2 - R_{PTO}^2}$$

$$X_{PTO} = Z_{PTO}\sqrt{1 - \frac{R_{PTO}^2}{Z_{PTO}^2}}$$

$$X_{PTO} = \frac{Z_{PTO}\frac{R_{PTO}}{Z_{PTO}}\sqrt{1 - \frac{R_{PTO}^2}{Z_{PTO}^2}}}{\frac{R_{PTO}}{Z_{PTO}}}$$

But:

$$cos\varphi_{PTO} = \frac{R_{PTO}}{Z_{PTO}}$$

$$X_{PTO} = \frac{R_{PTO}\sqrt{1 - cos\varphi_{PTO}^2}}{cos\varphi_{PTO}}$$

Thus:

$$P_{mean} = \frac{E^2 R_{PTO}}{(R_{wec} + R_{PTO})^2 + (X_{wec} \pm \frac{R_{PTO}\sqrt{1 - cos\varphi_{PTO}^2}}{cos\varphi_{PTO}})^2}$$

A.3   Stator voltage trajectory of PMSG

Calculating the trajectory of stator voltage equation from v_d and v_q voltages of a PMSG, section 5.6:

The limit of stator voltage in PMSG:

$$v_d^2 + v_q^2 = V_{limit}^2$$

This could be written as:

$$(R_s i_d - w_e i_q L)^2 + (R_s i_q + w_e i_d L + w_e \Psi_m)^2 = V_{limit}^2$$

Multiplying out the parenthesis:

$$R_s^2 i_d^2 - 2R_s i_d w_e i_q L + w_e^2 i_q^2 L^2 + R_s^2 i_q^2 + 2R_s i_q w_e (i_d L + \Psi_m) + w_e^2 (i_d L + \Psi_m)^2 = V_{limit}^2$$

Expanding the parenthesis in the above equation, eliminating equal expressions and rearranging the resulting equation :

$$R_s^2 i_d^2 + w_e^2 i_q^2 L^2 + R_s^2 i_q^2 + 2R_s i_q w_e \Psi_m + w_e^2 i_d^2 L^2 + 2w_e^2 i_d L \Psi_m + w_e^2 \Psi_m^2 = V_{limit}^2$$

$$(R_s^2 + w_e^2 L^2) i_d^2 + 2w_e^2 L \Psi_m i_d + (R_s^2 + w_e^2 L^2) i_q^2 + 2w_e R_s \Psi_m i_q + w_e^2 \Psi_m^2 = V_{limit}^2$$

Multiplying the whole equation by $R_s^2 + w_e^2 L^2$:

$$(R_s^2 + w_e^2 L^2)^2 i_d^2 + 2(R_s^2 + w_e^2 L^2) w_e^2 L \Psi_m i_d + (R_s^2 + w_e^2 L^2)^2 i_q^2 + 2(R_s^2 + w_e^2 L^2) w_e R_s \Psi_m i_q$$
$$+ (R_s^2 + w_e^2 L^2) w_e^2 \Psi_m^2 = (R_s^2 + w_e^2 L^2)\, V_{limit}^2$$

Expanding parenthesis and rearranging:

$$(R_s^2 + w_e^2 L^2)^2 i_d^2 + 2(R_s^2 + w_e^2 L^2) w_e^2 L \Psi_m i_d + w_e^4 L^2 \Psi_m^2 + (R_s^2 + w_e^2 L^2)^2 i_q^2$$
$$+ 2(R_s^2 + w_e^2 L^2) w_e R_s \Psi_m i_q + w_e^2 R_s^2 \Psi_m^2 = (R_s^2 + w_e^2 L^2)\, V_{limit}^2$$

$$\left((R_s^2 + w_e^2 L^2) i_d + w_e^2 L \Psi_m\right)^2 + \left((R_s^2 + w_e^2 L^2) i_q + w_e R_s \Psi_m\right)^2 = (R_s^2 + w_e^2 L^2)\, V_{limit}^2$$

Dividing the above equation by $(R_s^2 + w_e^2 L^2)^2$:

$$\left(i_d + \frac{w_e^2 L \Psi_m}{R_s^2 + w_e^2 L^2}\right)^2 + \left(i_q + \frac{w_e R_s \Psi_m}{R_s^2 + w_e^2 L^2}\right)^2 = \frac{V_{limit}^2}{R_s^2 + w_e^2 L^2}$$

A.4 The boundary value of q-axis current

The boundary values for i_q in field-weakening, section 5.6:

$$(2w_e^2 L\Psi_m)^2 - 4(R_s^2 + w_e^2 L^2)(i_d + w_e^2 i_q^2 L^2 + R_s^2 i_q^2 + w_e^2 \Psi_m^2 + 2R_s w_e \Psi_m i_q - V_{limit}^2) \geq 0$$

Ignoring the value of armature resistance:

$$(2w_e^2 L\Psi_m)^2 - 4w_e^2 L^2(w_e^2 i_q^2 L^2 + w_e^2 \Psi_m^2 - V_{limit}^2) \geq 0$$

$$4w_e^4 L^4 i_q^2 + 4w_e^4 L^2 \Psi_m^2 - 4w_e^2 L^2 V_{limit}^2 - 4w_e^4 L^2 \Psi_m^2 \leq 0$$

$$4w_e^2 L^2(w_e^2 L^2 i_q^2 - V_{limit}^2) \leq 0$$

Since $4w_e^2 L^2$ is always greater than zero:

$$w_e^2 L^2 i_q^2 - V_{limit}^2 \leq 0$$

$$w_e^2 L^2 i_q^2 \leq V_{limit}^2$$

$$\mid i_q \mid \leq \mid \frac{V_{limit}}{w_e L} \mid$$

Thus the boundaries of i_q are:

$$-\frac{V_{limit}}{w_e L} \leq i_q \leq \frac{V_{limit}}{w_e L}$$

A.5 Calculating damping and spring coefficient

The calculation for finding the values of damping coefficient $\boldsymbol{B_{PTO}}$ and spring coefficient $\boldsymbol{M_{PTO}}$ for optimal control in section is 4.1.2:

With impedance matching:

$$F_{PTO} = -Z_{PTO}\, v\,(w)$$

$$Z_{PTO} = Z_{wec}^*\,(w)$$

The PTO force is equal to:

$$F_{PTO}\,(t) = -B_{PTO}\dot{z}\,(t) - M_{PTO}\ddot{z}\,(t)$$

$$F_{PTO}\,(w) = -B_{PTO}v\,(w) - M_{PTO}\dot{v}\,(w)$$

$$F_{PTO}\,(w) = -(B_{PTO} + jwM_{PTO})\,v\,(w)$$

$$Z_{PTO} = Z_{wec}^*\,(w)$$

$$B_{PTO} + jwM_{PTO} = R_{wec}\,(w) - jX_{wec}\,(w)$$

The values of B_{PTO} and M_{PTO} would be:

$$B_{PTO} = R_{wec}\,(w) \quad and \quad M_{PTO} = -X_{wec}\,(w)\,/w$$

A.6 Plots of uncapped passive loading

Plots of peak mechanical force, peak velocity and peak position of WEC in uncapped passive loading are shown below.
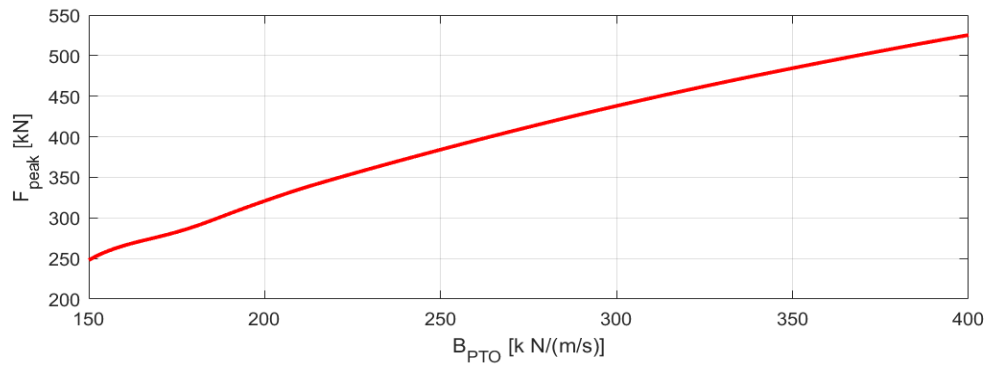
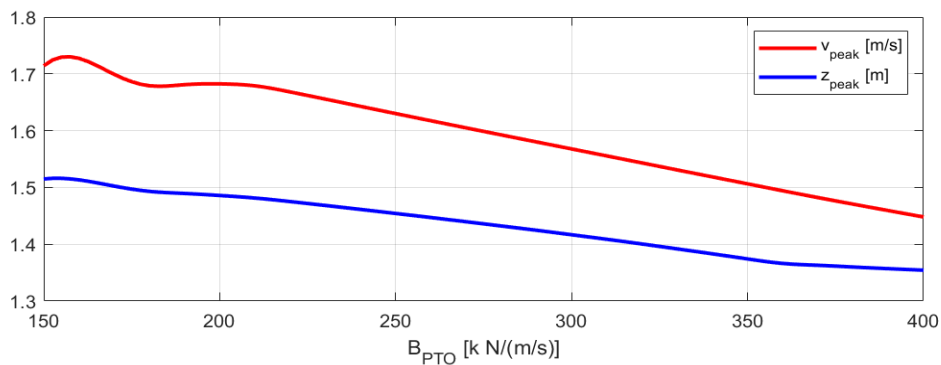**Figure A.1:** The plot of peak mechanical force versus damping coefficient in uncapped passive loading
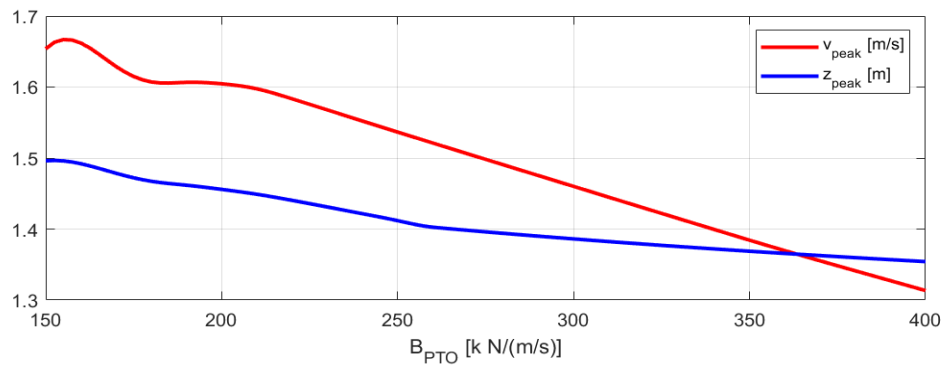
Figure A.2: The plot of peak velocity and peak stroke position versus damping coefficient in uncapped passive loading

A.7   Plots of capped passive loading

Plots of peak mechanical force, peak mechanical power, peak electrical power, peak velocity and peak stroke position of WEC in capped passive loading.
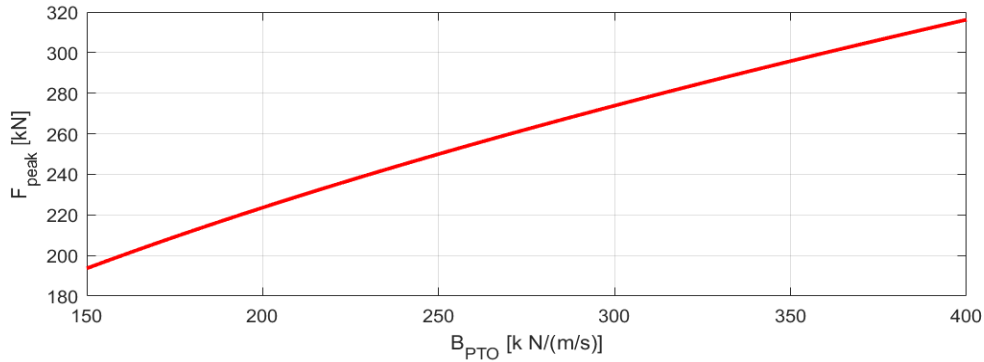
Figure A.3: The plot of peak mechanical force versus damping coefficient in capped passive loading
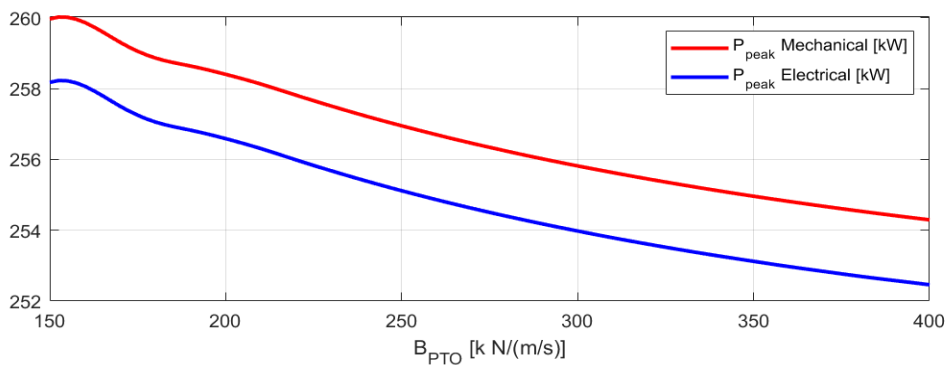
Figure A.4: The plot of peak mechanical and peak electrical power of PMSG versus damping coefficient in capped passive loading

Figure A.5: The plot of peak velocity and peak stroke position versus damping coefficient in capped passive loading

A.8   Plots of uncapped optimum control

Plots of peak mechanical force, average mechanical power, peak electrical power, peak mechanical power, the ratio of peak to mean mechanical power, peak velocity and peak stroke position in uncapped optimum control are shown below.
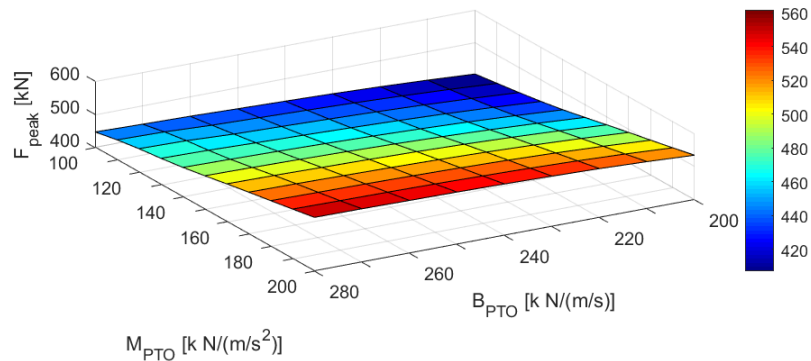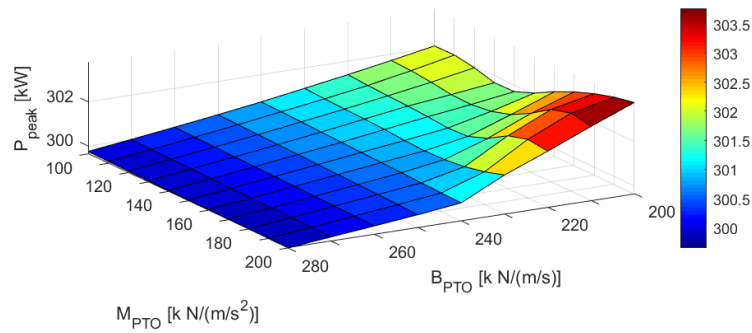

Figure A.6: The plot of peak mechanical force for different values of damping coefficient, B_{PTO} and spring coefficient, M_{PTO} in uncapped optimum control
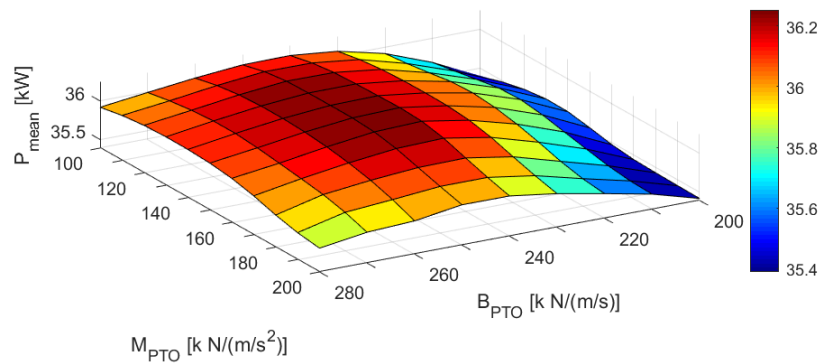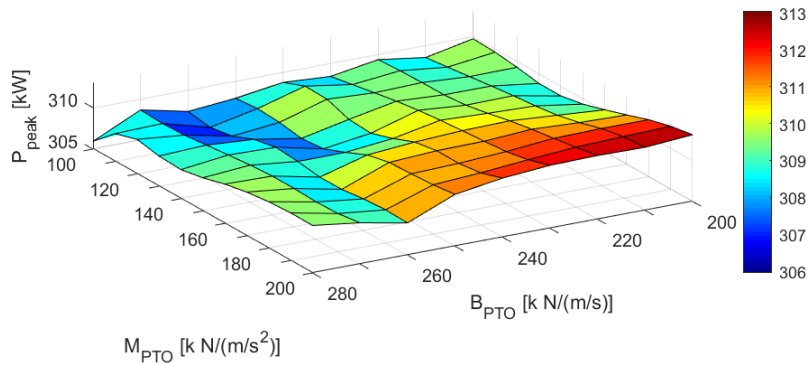

Figure A.7: The plot of mean mechanical input power for different values of damping coefficient, B_{PTO} and spring coefficient, M_{PTO} in uncapped optimum control

Figure A.8: The plot of peak mechanical input power for different values of damping coefficient, B_{PTO} and spring coefficient, M_{PTO} in uncapped optimum control

Figure A.9: The plot of peak electrical output power for different values of damping coefficient, B_{PTO} and spring coefficient, M_{PTO} in uncapped optimum control
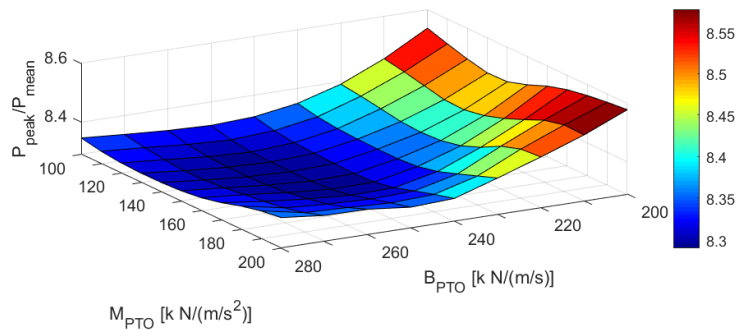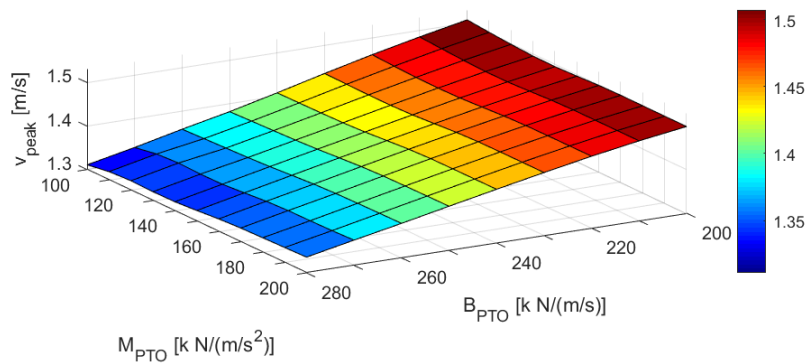

Figure A.10: The plot of the ratio of peak to mean mechanical power for different values of damping coefficient, B_{PTO} and spring coefficient, M_{PTO} in uncapped optimum control

Figure A.11: The plot of peak velocity for different values of damping coefficient, B_{PTO} and spring coefficient, M_{PTO} in uncapped optimum control
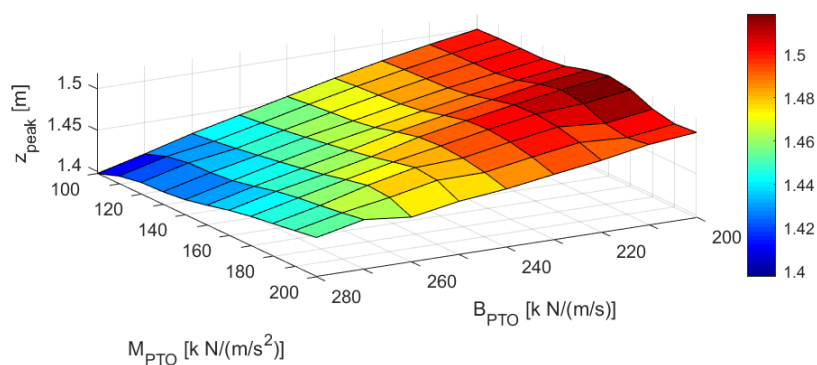

Figure A.12: The plot of peak stroke distance for different values of damping coefficient, B_{PTO} and spring coefficient, M_{PTO} in uncapped optimum control

A.9   Plots of Capped Optimum Control

Plots of peak mechanical force, average mechanical power, peak electrical power, peak mechanical power, the ratio of peak to mean mechanical power, peak velocity and peak stroke position in capped optimum control are shown below.
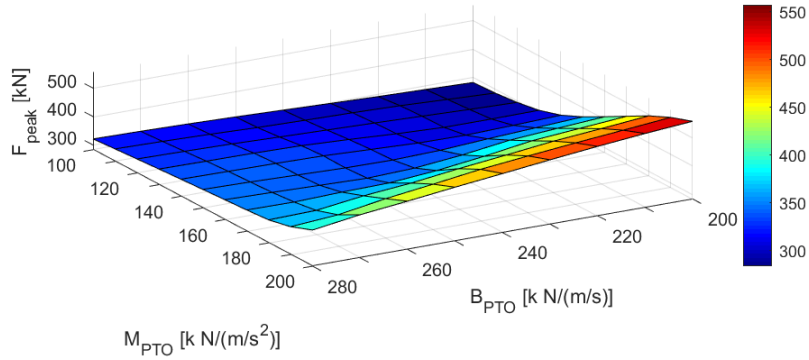

Figure A.13: Plot of peak mechanical force for different values of damping coefficient, B_{PTO} and spring coefficient, M_{PTO} in capped optimum control
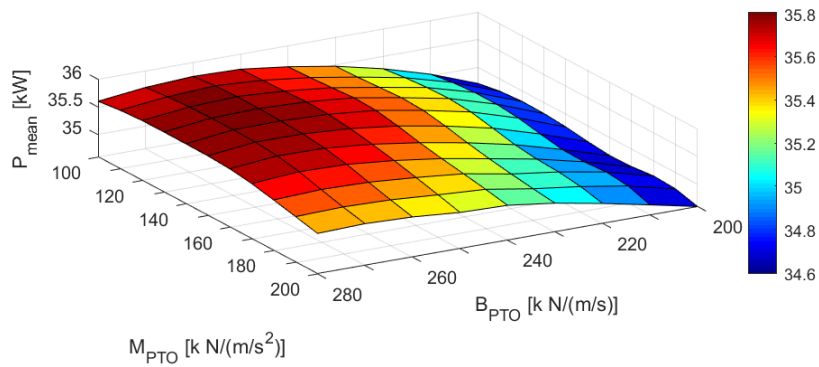

Figure A.14: The plot of mean mechanical input power for different values of damping coefficient, B_{PTO} and spring coefficient, M_{PTO} in capped optimum control
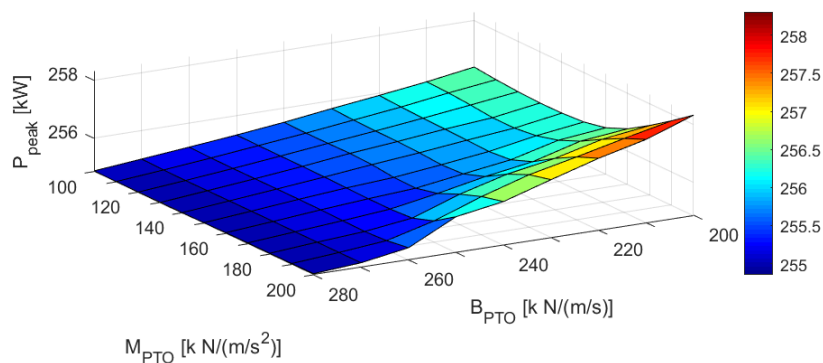
Figure A.15: The plot of peak mechanical input power for different values of damping coefficient, B_{PTO} and spring coefficient, M_{PTO} in capped optimum control
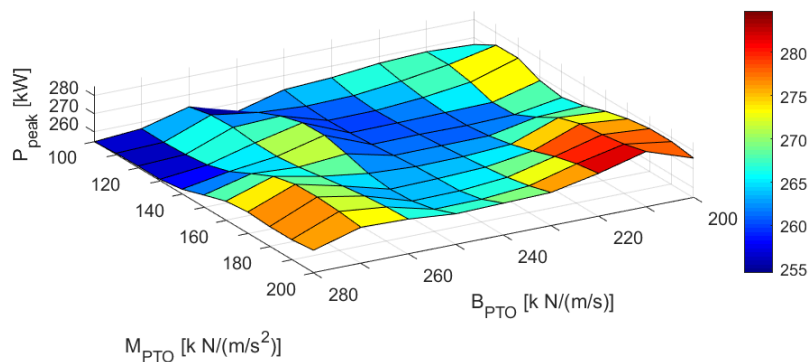

Figure A.16: The plot of peak electrical output power for different values of damping coefficient, B_{PTO} and spring coefficient, M_{PTO} in capped optimum control
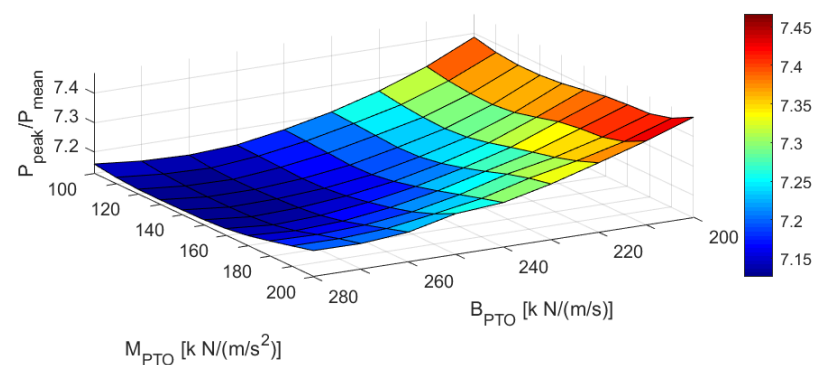

Figure A.17: The plot of the ratio of peak to mean mechanical input power for different values of damping coefficient, B_{PTO} and spring coefficient, M_{PTO} in capped optimum control
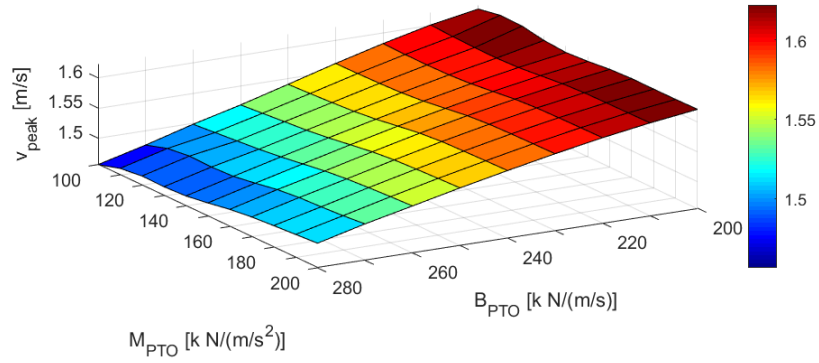
Figure A.18: The plot of maximum velocity for different values of damping coefficient, B_{PTO} and spring coefficient, M_{PTO} in capped optimum control
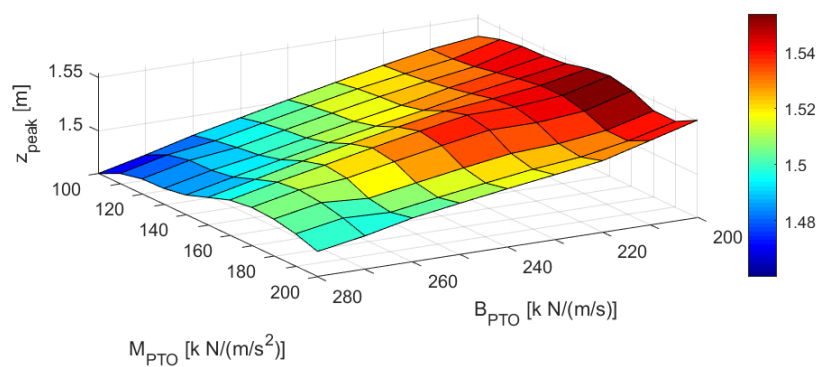

Figure A.19: The plot of maximum stroke distance for different values of damping coefficient, B_{PTO} and spring coefficient, M_{PTO} in capped optimum control

B | Appendix

MATLAB Script

B.1 MATLAB script for Bretschneider spectrum

Listing B.1: A MATLAB script for Bretschneider spectrum of a significant height of 3.25m and a peak period of 12 seconds.

```
% Bretschnieder Spectrum
clear;
Hs = 3.25 ;        % significant wave height
Tp = 12 ;          % peak period
wp = 2*pi/Tp ;     % 1/peak period

% Frequencies of spectrum
wspec = (.001:.005:2);

% Bretschnieder Spectrum
for j = 1:length(wspec)
w = wspec(j);
S(j) = 5/16 * wp^4/w^5 * Hs^2 * exp(-5*wp^4 /(4*w^4));
end

% plot and labels
grid;
plot(wspec,S,'r','LineWidth',2);
legend({['T 10sec' newline 'H 3.25m']})
xlabel('frequency \omega, rad/s');
ylabel('S(\omega)');
grid;
```

B.2   MATLAB script for Wec-Sim input file

Listing B.2: A MATLAB script for Wec-Sim input file

```
%% Simulation Data
simu = simulationClass();% Create the Simulation Variable

simu.simMechanicsFile='CETOlike_relDrag_EMG_Pcapped_v2p2.slx';

Fref_from_Gen = 1;% If the Fref send back is from Gen or not
                % (1 if Fref is from Gen and 0 for WEC)
par.test.S = 0        ;% EMG spring coefficient [N/m]
par.test.K = 266.6e3;% EMG damping coefficient [N/(m/s)]


% POWER CONTROL LOGIC
P_rated = 250e3; % rated power for PTO
P_multi = 2     ; % inst. power multiplier constant

simu.mode = 'normal';% Specify Simulation Mode
                % ('normal','accelerator','rapid-accelerator')
simu.explorer='off'; % Turn SimMechanics Explorer (on/off)
simu.solver = 'ode4';% simu.solver = 'ode4' for fixed step
                % & simu.solver = 'ode45' for variable step
simu.dt =0.0005;      % Simulation time-step [s]
simu.rampTime = 20;  % Wave Ramp Time Length [s]
simu.startTime = 20; % Simulation Start Time [s]
simu.endTime=simu.rampTime+600;% Simulation End bdcloseTime[s]
simu.b2b  = 0;        % Body-to-body interactions
simu.rho = 1025;      % Water density - default = 1000!
simu.nlHydro = 0;     % Non-linear FK force
simu.dtNL = 0.02;
simu.ssCalc = 1;% Control option to use state space model
simu.CITime=20;
% simu.dtFeNonlin=1*simu.dt;% Non-linear FK force time-step
simu.paraview=0;% Output files for visualisation in Paraview
                % (0-No ; 1-Yes)
simu.reloadH5Data = 1;
simu.pressureDis = 1;% Option to save pressure distribution:
                % Off->'0', On->'1', (default = 0)

simu.domainSize=30;
    % Side-length of the square domain for viewing

simu.dtOut = 0.001;

%% Irregular Waves using PM Spectrum with Convolution
% Integral Calculation
```

```
waves = waveClass('irregular');
      % Create the Wave Variable and Specify Type
waves.H = 3.25                    ;% Significant Wave Height [m]
waves.T = 12                      ;% Peak Period [s]

waves.spectrumType = 'BS';

waves.freqDisc = 'EqualEnergy';
      % Uses 'EqualEnergy' bins (default)
waves.phaseSeed = 2;% Phase is seeded so eta is the same
waves.waveDir=0;%[deg] Incident wave direction (Default = 0)

%% User-Defined Time-Series
if simu.paraview==1
    waves.viz.numPointsX=50;
    waves.viz.numPointsY=5;
end
%% Body Data
%% Float
%body(1) = bodyClass('.\hydrodata\CETO-like.h5');
body(1) = bodyClass('.\hydrodata\CETO-likev2.h5');
body(1).mass = 76.9e3;% 'equilibrium';
body(1).momOfInertia = [6.4e5 6.4e5 7.8e5;];
                   % Moment of Inertia [kg*m^2]
body(1).geometryFile = '.\geometry\CETO-likev2a.stl';
                   % Location of Geometry File

body1_diameter = 9.1;
body1_height = 6.5;

body(1).viscDrag.cd = 1.*[0.7 0.7 1.28 0.22 0.22 0];
body(1).viscDrag.characteristicArea = [body1_diameter ...
    *body1_height body1_diameter*body1_height pi ...
    *(body1_diameter/2).^2 body1_diameter ...
    *body1_diameter.^4 body1_diameter*body1_diameter.^4 0];

%% PTO and Constraint Parameters
%% Gimbal Tether - Float Connection
constraint(1) = constraintClass('Constraint1');
    % Create Constraint Variable and Set Constraint Name
constraint(1).loc=[0 0 -8.5];%Gimbal Constraint Location[m]
top_const_k=1e1;    % Gimbal stiffness [N.m/(rad)]
top_const_c=5e5;    % Gimbal damping [N.m/(rad/s)]

%% Universal Tether - Seabed Connection
constraint(2) = constraintClass('Constraint1');
    % Create Constraint Variable and Set Constraint Name
constraint(2).loc = [0 0 -26];% Constraint Location [m]
```

```matlab
%% Translational PTO

pto(1) = ptoClass('PTO1');
    % Create PTO Variable and Set PTO Name

pto(1).k=0;% PTO Stiffness [N/m]
pto(1).c=0;% PTO Damping [N/(m/s)]


pto(1).loc = [0 0 -26];% PTO Location [m]
if simu.nlHydro > 0
    pto_pull=-2.5464625e+06;% PTO pre-tension [N]
else
    pto_pull=-2.5603467e+06;% PTO pre-tension [N]
end
% PTO visualisation
body(2) = bodyClass('');
body(2).nhBody=1;
body(2).mass = 1;%'equilibrium';
body(2).dispVol=0;
body(2).momOfInertia = [1 1 1];% Moment of Inertia [kg*m^2]
body(2).geometryFile = '.\geometry\ptoLocation5m.stl';
    % Location of Geometry File
body(2).cg=[0,0,-13];

pto_k=0; % EMG spring coefficient [N/m]
pto_c=0; % EMG damping coefficient [N/(m/s)]

%%%%%%%%%%%%%%%%%%%%%%%%%%%%%%%%%%%%%%%%%%%%%%%%%%%%%%%%%%%%%%%
% Linear PTO actuation point
%% Base
body(3) = bodyClass('');
body(3).mass = 2;%'equilibrium';
body(3).nhBody = 1;
body(3).dispVol = 0.001951;
body(3).cg = [0;0;-14.5];
body(3).cb = [0;0;-14.5];
body(3).name = 'Linear PTO';
body(3).momOfInertia = [1 1 1];% Moment of Inertia [kg*m^2]
body(3).geometryFile = '.\geometry\linear_pto_v2.stl';
    % Location of Geometry File

body(4) = bodyClass('');
body(4).mass = 1;% 'equilibrium';
body(4).nhBody = 1;
body(4).dispVol = 9.7561e-04;
```

```matlab
body(4).cg = [0.0;0;-11.566];
body(4).cb = [0.0;0;-11.566];
body(4).name = 'Linear PTO rod';
body(4).momOfInertia = [1 1 1];% Moment of Inertia [kg*m^2]
body(4).geometryFile = '.\geometry\linear_pto_rod_v2.stl';
    % Location of Geometry File
pto_stroke_range = 5;
%%%%%%%%%%%%%%%%%%%%%%%%%%%%%%%%%%%%%%%%%%%%%%%%%%%%%%%%%%%%%%%%%%%%%%%%%
%% EMG SETUP

pto(2) = ptoClass('PTO2');
    % Create PTO Variable and Set PTO Name

pto(2).loc = [0 0 -14.5];

    % [DEFINE EMG PARAMETERS]
par.EMG.inertia = 0.0e3;
    % EMG total inertia on translating axis [kg]


%Site1
par.EMG.F_s0  = 11468.4;% EMG static friction force [N]
par.EMG.mu_d0 = 22809.3;
    % EMG dynamic friction coefficient [N/(m/s)]


%% Generator parameters
% Thesis: Aalborg University. Vasile Simion Sularea.
% Design and control of high efficiency wind turbine
% based hydrogen production system
p=8;              % poles pairs
flux = 5.82;      % permanent flux
Rs= 0.00821;      % stator resistance
Ls= 0.014;        % Stator inductance
Ld= 0.014;        % d-axis inductance
Lq= 0.014;        % q-axis inductance
psc= 0.10125;     % pitch screw
Vdc=1000;         % DC-link voltage
Vphmax=500;       % Voltage limit due to DC-link voltage
Vlimit= 475;      % Voltage limit of the generator
```

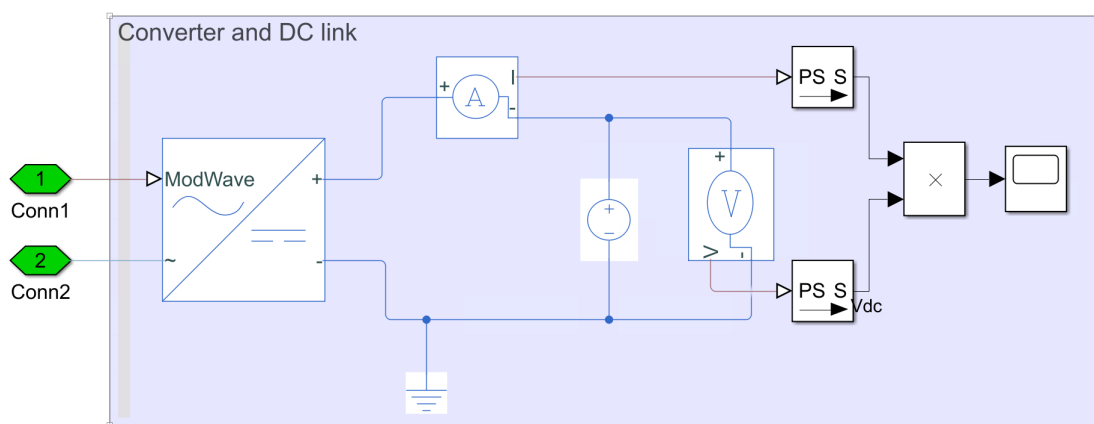# Appendix C

Figures of Simulink Model

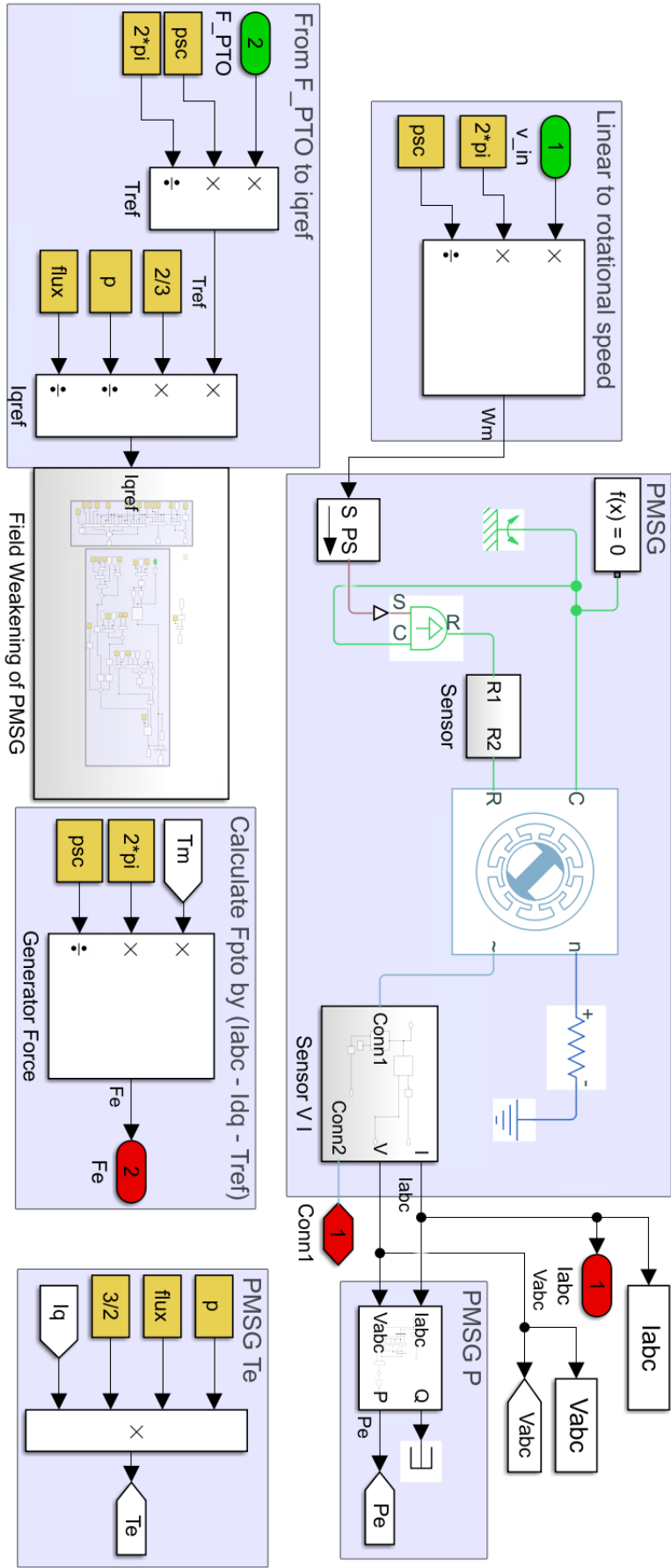**Figure C.1:** Simulink model of Converter and DC-link

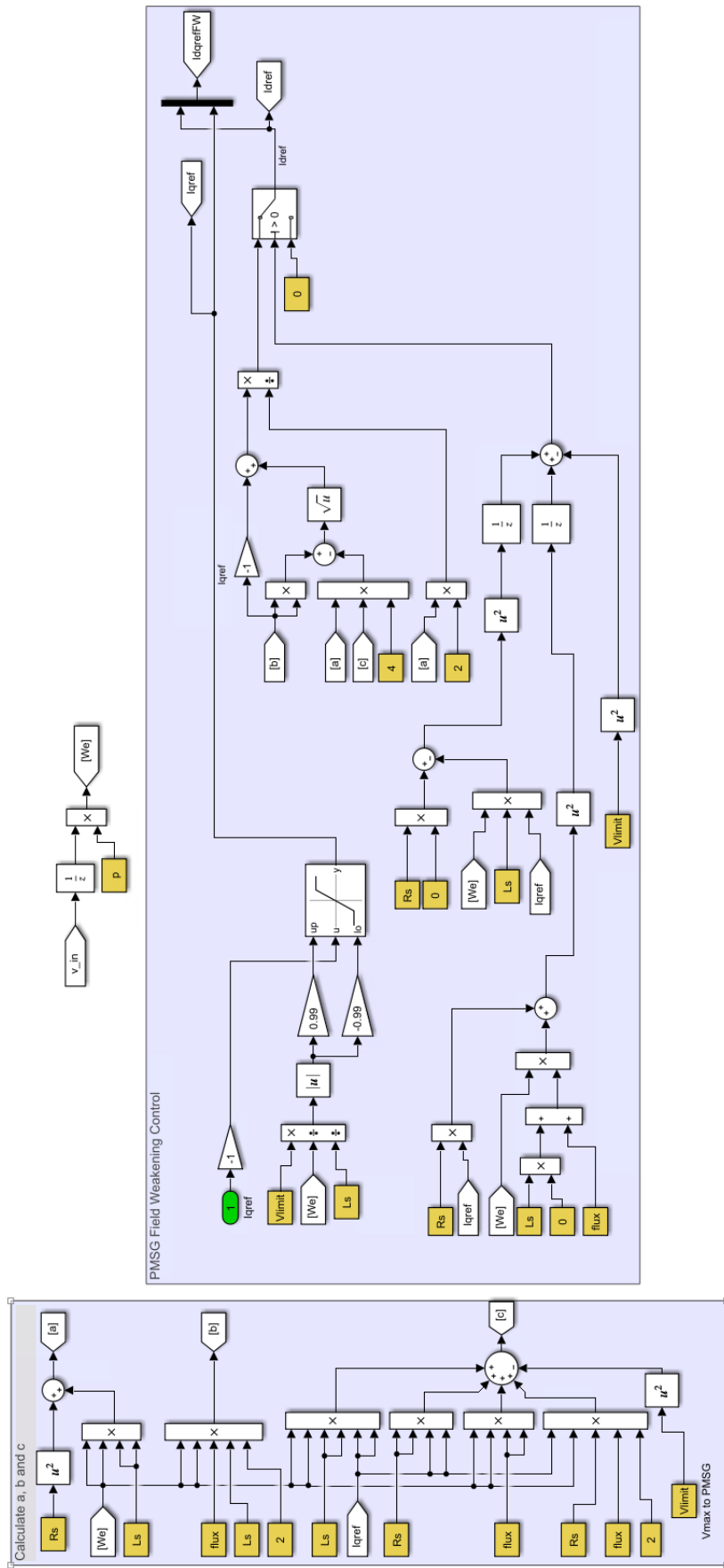**Figure C.2:** Simulink model of Surface Mounted PMSG
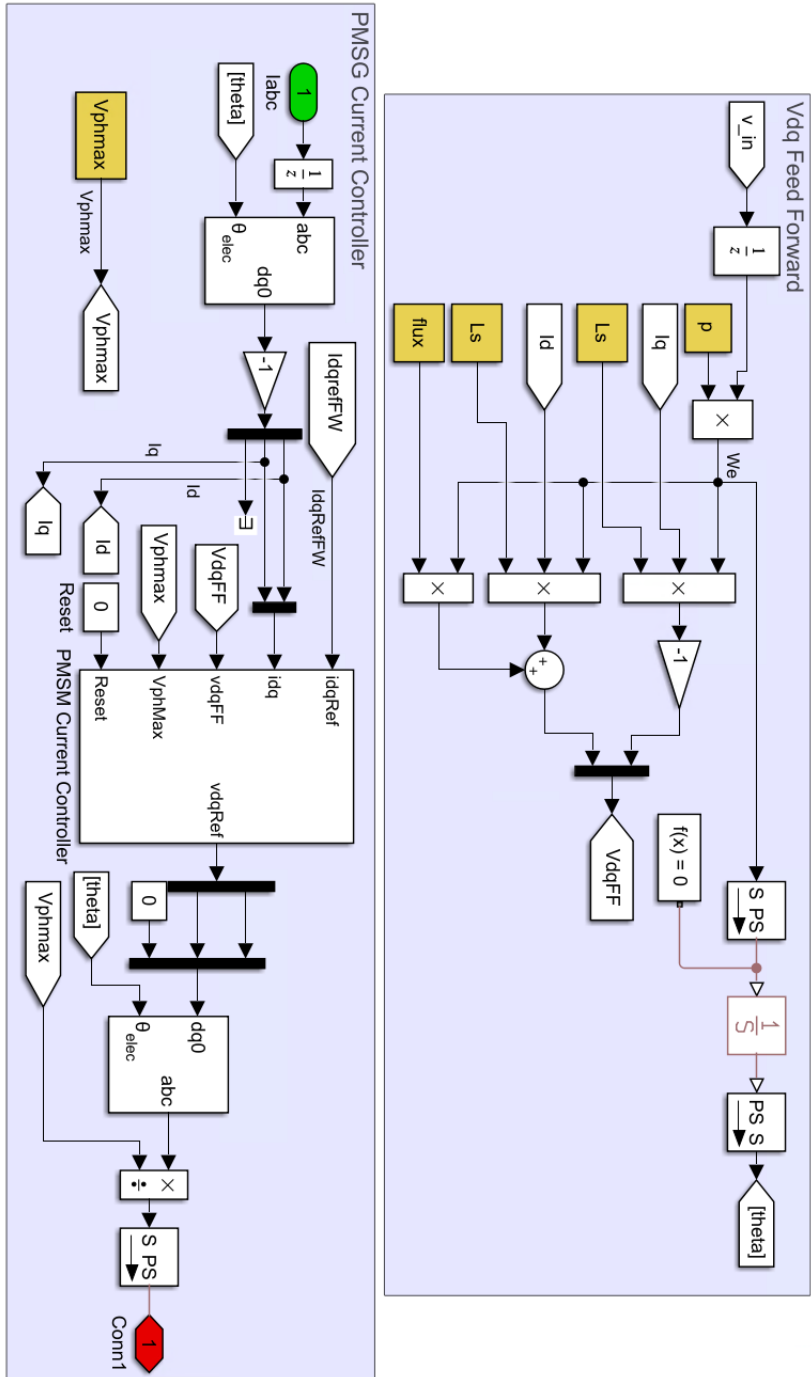
Figure C.3: Simulink model of Field Weakening of PMSG

Figure C.4: Simulink model of Current Controller

Meron Yemane

Modelling and Control of Wave-to-Wire Model of Point Absorber Wave Energy Converters (WECs)

NTNU
Norwegian University of
Science and Technology